Master of Science Thesis

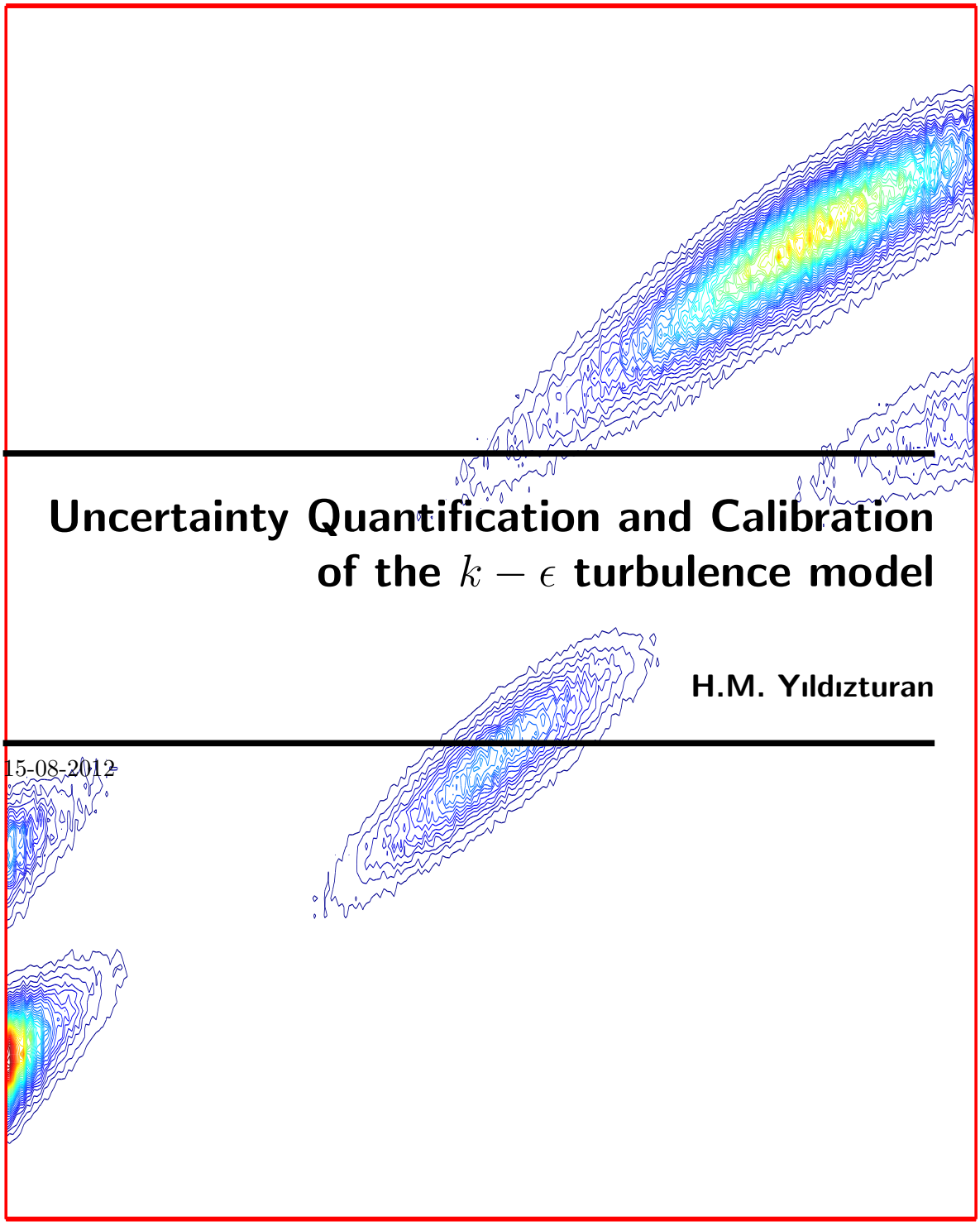

Uncertainty Quantification and Calibration of the $k - \epsilon$ turbulence model

H.M. Yıldızturan

15-08-2012

Faculty of Aerospace Engineering · Delft University of Technology

Uncertainty Quantification and Calibration of the $k - \epsilon$ turbulence model

Master of Science Thesis

For obtaining the degree of Master of Science in Aerospace Engineering at Delft University of Technology

H.M. Yıldızturan

15-08-2012

Faculty of Aerospace Engineering · Delft University of Technology

Delft University Of Technology
Department Of
Aerodynamics

The undersigned hereby certify that they have read and recommend to the Faculty of Aerospace Engineering for acceptance the thesis entitled **"Uncertainty Quantification and Calibration of the $k-\epsilon$ turbulence model"** by **H.M. Yıldızturan** in fulfillment of the requirements for the degree of **Master of Science**.

Dated: 15-08-2012

Exam committee:

Prof.dr.ir.drs. H. Bijl

Dr. R.P. Dwight

Dr. S.J. Hulshoff

Ir. J.H.S. de Baar

Summary

Nowadays, the numerical errors are decreased to an acceptable level in the sense that the variability of the model parameters is becoming more important for obtaining results with higher reliability. Therefore, the focus of this thesis is on the quantification of the uncertainties of the turbulent closure model $k-\epsilon$. The $k-\epsilon$ model is tuned to free shear flows and used for wall-bounded flows in combination with wall functions. To increase the reliability of the $k-\epsilon$ model for predictions of turbulent flows the uncertainty quantification (UQ) methodology is applied in this thesis. As a test case the external flow over the airfoil DU96-W-180 is considered.

Hence, the first aim of the thesis is the application of the UQ methodology to the considered phenomenon. This incorporates the quantification of the uncertainties to the analysis of the effects of the uncertainties on the desired outputs. In this thesis only the parametric uncertainty is quantified and the desired outputs are the lift and drag coefficients C_l and C_d. The uncertainties are efficiently propagated through the $k-\epsilon$ model for one- and five-dimensional analysis with the Probabilistic Collocation (PC) method. The multi-dimensional analysis is limited to five parameters because of the curse of dimensionality.

From 1-D UQ analysis followed that the discretization error is about 8.3 % and 1.74 % of the range of the most influential parameters respectively for the lift and drag coefficient. This illustrates the importance of UQ analysis. Furthermore, the uncertainty in the force coefficients increases for increasing multi-dimensional analysis and for increasing angles of attack α.

The second aim of the report is to calibrate the standard $k-\epsilon$ model with the experimental data of the force coefficients by employing Bayesian framework with the Markov Chain Monte Carlo method for the five most influential parameters. For the evaluation of the standard $k-\epsilon$ model the surrogate models obtained from 5-D UQ analysis are used. The calibrations are performed for the domain of α where the lift curve is linear and by using varying amount of experimental data.

The calibrations did not yield the expected accurate fit of the numerical simulations to the experimental data for the desired domain. The main reasons therefore are the presence

of model inadequacy and the observed discrepancy between the surrogate model and the numerical simulations especially for high α. However, for α up to five degrees much better fit is obtained of the numerical simulations to the experimental data.

Acknowledgements

I would like to thank just everyone that has a contribution in this achievement.

Special thanks go to Richard Dwight who made major contribution to this report by sharing his ideas and knowledge with me.

Contents

List of Figures

List of Tables

Nomenclature

General list of symbols

Symbol	Descpription	Unit
ρ	density	$[\frac{kg}{m^3}]$
ν	kinematic viscosity	$[\frac{m^2}{s}]$
p	pressure	$[\frac{N}{m^2}]$
u	velocity	[m/s]
V_∞	freestream velocity	$[\frac{m}{s}]$
k	turbulence kinetic energy	$[kg\frac{m}{s^2}]$
ϵ	dissipation rate of k	$[kg\frac{m}{s^3}]$
ν_t	eddy viscosity	$[\frac{m^2}{s}]$
y^+	scale for distance from wall	[-]
τ_w	wall shear stress	$[\frac{N}{m^2}]$
α	angle of attack	$[deg]$
M	Mach number	[-]
R	Reynolds number	[-]
C_l	2-D lift coefficient	[-]
C_d	2-D drag coefficient	[-]
C_p	pressure coefficient	[-]
c	chord length	$[m]$
CV	coefficient of variation	[-]
μ	statistical mean	

σ	standard deviation
σ^2	statistical variance
θ	uncertain model parameter

$k-\epsilon$ model parameters:

C_μ, $C_{\epsilon 1}$, $C_{\epsilon 2}$, σ_ϵ, σ_k

wall function parameters:

κ and E

Abbreviations

PC	Probabilistic Collocation
MCMC	Markov Chain Monte Carlo
AoA	angle of attack
pdf	probability density function

Chapter 1

Introduction

Though this be madness, yet there is method in it. William Shakespeare

In the last decades the abundant computational resources are extensively used to decrease the numerical errors. In that objective a level is achieved where the importance of uncertainty of the model parameters can be more significant than the numerical errors. In usual engineering the uncertainties that are inherently present in the process are dealt by design safety factors or knockdown factors. To improve the overall efficiency and reliability of the design the effect of the uncertainty, like in the model parameters, can be quantified. Besides, the quantification of the uncertainty can be used to calibrate the mathematical model in a Bayesian framework. In this thesis the uncertainty quantification (UQ) analysis and calibration of the model parameters of the standard $k-\epsilon$ turbulence model are performed. Introductory information is given about UQ analysis in Section 1.1. The considered physical phenomenon to perform these analyses is stated in Section 1.2. The objectives and outline of this thesis are stated in Section 1.3.

1.1 Uncertainty Quantification

Usually, after representing a physical phenomenon by a mathematical model the model is solved deterministically. This means that the input parameters are provided as fixed values to the model. However, almost in every physical problem there are variations, uncertainties which make it difficult to supply the model only with fixed values. For instance, in real flight the freestream velocity, angle of attack are uncertain due to varying atmospheric conditions. Production tolerances cause uncertainty in the geometry, in the physical properties of the material like the stiffness. Besides that, the degeneration of materials due to wear and tear changes their physical properties. Hence, the presence of uncertainty is ubiquitous.

Because of the complexity of the mathematical models often engineering problems are numerically solved like in computational fluid dynamics (CFD). This results in the numerical errors like the discretization and iteration error. The increasing computational resources of the latest twenty years are mainly utilized to decrease the numerical errors. At this stage, the level of uncertainty in the parameters can cause higher unreliability in the quantities of interest than the numerical errors. The reliability of the output can be improved by knowing the effects of the uncertainties in the output. Therefore, the uncertainties present in the system have to be quantified. After the uncertainties are represented by probability density functions (pdf) they need to be propagated through the mathematical model to analyze the effects on the quantities of interest. Basically, uncertainty quantification (UQ) incorporates the whole process of uncertainty analysis from defining and propagating the uncertainty to the stochastic output analysis.

There are different methods available to propagate the uncertainty through the mathematical model. A chronology of the popular methods in this field are the Monte Carlo method (S. Metropolis & Ulam, 1949), the Galerkin Polynomial Chaos (GPC) method (Ghanem & Spanos, 1991) and the Probabilistic Collocation (PC) method (Babuska, Nobile, & Tempone, 2007; G. J. A. Loeven, Witteveen, & Bijl, 2007). The Monte Carlo method is impractical to CFD problems due to its low convergence rate. The GPC results in coupled equations. Unlike the GPC the PC method results in decoupled equations for all kinds of input distributions. The decoupled equations increase the feasibility of UQ analysis. More information and examples of the PC and the other methods can be found in the references (G. J. A. Loeven, 2010; Witteveen, 2009; A. Loeven, Witteveen, & Bijl, 2006; G. J. A. Loeven & Bijl, 2008).

1.2 The considered physical phenomenon

The considered physical phenomenon in this thesis is the external turbulent flow over the airfoil DU96-W-180 (Timmer & Rooij, 2003). Experimental data of the lift coefficient C_l and the drag coefficient C_d are available for the considered physical phenomenon for 24 different angles of attack α in the range of $[-4.71°, 14.64°]$ at Reynolds number $R = 2 \cdot 10^6$ and Mach number $M = 0.15$. This phenomenon is numerically solved with the software OpenFOAM (OpenFOAM Team, n.d.) by employing the Reynolds Averaged Navier Stokes (RANS) equations and the standard $k - \epsilon$ turbulence model as the turbulence closure model. For detailed information about the physics of turbulence and about turbulence modelling the following sources are suggested (Davidson, 2004; Pope, 1998), (Bradshwa, Cebeci, & Whitelaw, 1981), (Wilcox, 1994) and (Gatski, Hussaini, & Lumley, 1996).

1.3 Objectives and outline of the thesis

The $k-\epsilon$ turbulence model parameters were calibrated to simple free shear flows by using experimental as well as numerical simulations. The presence of wall is incorporated in this model by making use of wall functions. Despite this methodology the original values

of the model parameters are kept the same as for free shear flows. In this thesis the model parameters of the $k-\epsilon$ model and the wall function are assumed to be uncertain. Note that for wall-bounded flows the terminology *standard* $k-\epsilon$ model or just $k-\epsilon$ model incorporates the standard wall function.

In light of the considered physical phenomenon the aim of this thesis is twofold:

1. Perform uncertainty quantification of the model parameters of the standard $k-\epsilon$ model.
2. Based on the results of the UQ analysis calibrate the standard $k-\epsilon$ model parameters.

Based on literature research the uncertainties in the parameters are determined by using analytical relations, experimental data and expert opinion. The standard $k-\epsilon$ model and the determination of the uncertainties in the parameters are reported in Chapter 2.

The $k-\epsilon$ model parameters are also assumed uncertain in the thesis of (Platteeuw, 2008) for UQ analysis. However, there are significant differences between the applied methodology and the results of Platteeuw and this thesis. A non-conservative approach is applied in this thesis in the sense that an attempt is made to find the largest possible dispersive distribution of the parameters. In Platteeuw's work some of the parameters are kept constant or assumed dependent on other uncertain parameters which result in neglecting uncertainty. Because the employed analytical relations are only valid to some specific flow and they contain also different uncertain parameters they are not used to define dependency relations between the uncertain parameters in this thesis. Furthermore, Platteeuw uses a different wall function.

To have a known and low discretization error mesh convergence study is performed in Chapter 3. For the objectives of the thesis it is important that the discretization error is not dominant with respect to the effects of the uncertainties.

Subsequently, the defined distributions of the uncertain parameters are used to investigate the effect of them on the quantities of interest C_l and C_d in Chapter 4. This has been pursued by propagating the uncertainties separately (1-D) and simultaneously (3-D and 5-D) with the PC method. Two of the seven uncertain parameters are discarded for 5-D UQ analysis based on the results of 1-D UQ analysis.

To have a better fit of the force coefficients from the simulations to the experimental data the model parameters of the standard $k-\epsilon$ are calibrated. For this purpose Bayesian Inference (Kennedy & O'Hagan, 2001; Wikle & Berliner, 2006) is applied in combination with the Markov Chain Monte Carlo method (MCMC) in Chapter 5. For the evaluation of the standard $k-\epsilon$ model the surrogate models are used that are obtained from 5-D UQ analysis for α 1.45°, 4.54° and 7.61°. The calibration is performed by employing varying amount of experimental data from two to six. The calibration may result in a set of calibrated parameters that eventually results in better match to the experimental

data of the considered physical phenomenon when numerically simulated. If the results are satisfying the calibrated parameters might be used to simulate external turbulent flow over other airfoils for similar conditions of the freestream.

Calibration with the Bayesian framework is applied by (Cheung, Oliver, Prudencio, Prudhomme, & Moser, 2011) to the Spalart-Allmaras turbulence closure model. Cheung et. al. did not perform a detailed research to quantify the uncertainties nor did he investigate the effect of the uncertainties on the quantities of interest. Furthermore, Cheung et. al. use different model classes to take into account the model inadequacy. That approach is out of the scope of this thesis.

Finally, the conclusion and the recommendations of this work are stated in Chapter 6.

Chapter 2

Quantification of the parametric uncertainties of the standard $k-\epsilon$ model

The main objective of this chapter is to quantify the uncertainties in the model parameters of the $k-\epsilon$ model. Therefore, the rational behind the $k-\epsilon$ model is discussed starting from the RANS equations in Section 2.1. Subsequently, the principles of the $k-\epsilon$ are stated in Section 2.2. The distributions of the uncertain parameters are determined in Section 2.3. The uncertain parameters consist of the core $k-\epsilon$ model parameters and the wall-function parameters. The determined distributions are illustrated at the last page of this chapter in Figure 2.4.

2.1 Reynolds Averaged Navier-Stokes

Despite the chaotic flow properties of turbulence its statistics indicate a clear mean part and a fluctuating part around the mean when observed over time. This very important statistical property of turbulence brought the idea of averaging of the Navier-Stokes (NS) equations, which govern the motion of the fluid flow (Davidson, 2004). Averaging of the NS equations yields the Reynolds Averaged Navier-Stokes equations (RANS). The desired aim of RANS is to obtain the mean properties of turbulent flow. The immediate effect of obtaining only the mean properties of a flow is the loss of the fine details, however, averaging simplifies the turbulent flow modelling enormously, at least for engineering purposes. The idea of averaging is to decompose the state variables in a mean and a fluctuating part e.g. the velocity vector decomposition yields $\mathbf{u} = \overline{\mathbf{u}} + \mathbf{u}'$, with $\mathbf{u}$ the real velocity field, $\overline{\mathbf{u}}$ is the mean part of the velocity field and $\mathbf{u}'$ is the fluctuation around the mean. This idea is first introduced by Osborne Reynolds, he came to this idea after visualizing a turbulent water flow through a pipe (Osborne, 1883a, 1883b; Eckhardt,

2009). Eventually, the RANS equations, the overbars indicate the mean properties, are

$$\rho(\overline{\mathbf{u}}\cdot\nabla)\overline{u}_i = -\frac{\partial\overline{p}}{\partial x_i} + \frac{\partial}{\partial x_j}\left[\overline{\tau}_{ij} + \tau_{ij}^R\right], \tag{2.1}$$

where ρ is the density of the flow $\left[\frac{kg}{m^3}\right]$, p is the pressure $\left[\frac{N}{m^2}\right]$, u represents the velocity $\left[\frac{m}{s}\right]$, $\overline{\tau}_{ij}$ represents the shear stress $\left[\frac{N}{m^2}\right]$ for Newtonian fluids its definition is $\overline{\tau}_{ij} = \rho\nu\left[\frac{\partial\overline{u}_i}{\partial x_j} + \frac{\partial\overline{u}_j}{\partial x_i}\right]$ where ν represents the kinematic viscosity $\left[\frac{m^2}{s}\right]$ and $\tau_{ij}^R = -\rho\overline{u_i'u_j'}$ represent the Reynolds stresses $\left[\frac{N}{m^2}\right]$.

The Reynolds averaging process leads to a new term namely the Reynolds stresses, in fact the Reynolds stresses represent the mean momentum fluxes induced by the turbulence. The Reynolds stresses are unknown, so this averaging process accumulates the unknowns. There are only four equations available, three momentum equations in x, y, z directions and the continuity equation. The unknown variables in the RANS equation are velocity vector, pressure and six Reynolds-stresses. The fact that there are more unknowns than the available equations is called in the turbulence terminology the *closure problem of turbulence*. It looks like there is a dilemma, the Navier-Stokes equations are deterministic, they can give chaotic representation of the velocity field, however, they are too complex for engineering applications and on the other hand the obtained equations by averaging of Navier-Stokes leads to the closure problem of turbulence.

The last resource for this dilemma is to model the Reynolds stresses to reduce the number of unknowns. Therefore *turbulence closure models* are invented. The eddy viscosity hypothesis is still the backbone of many engineering turbulence closure models. The first eddy-viscosity model dates back to 1870s and it is the work of Boussinesq. The main idea of this work is that Reynolds stresses can be linked to the mean rate of deformation, this will be further explored in the next section.

2.2 The $k-\epsilon$ turbulence model

The Reynolds stresses in the RANS equations can be approximated by the eddy viscosity hypothesis. This hypothesis is based on the work of Boussinesq and Prandtl. Boussinesq proposed in 1870 for averaged flows the following expression

$$\overline{\tau}_{xy} + \tau_{xy}^R = \rho(\nu + \nu_t)\frac{\partial\overline{u}_x}{\partial y}. \tag{2.2}$$

The idea of Boussinesq's work is that the turbulent mixing of momentum is analogous to the laminar stress $\overline{\tau}_{xy}$, however, the effective viscosity is raised from ν to $\nu + \nu_t$, ν_t is called the eddy viscosity $\left[\frac{m^2}{s}\right]$. The Boussinesq expression is of one-dimensional nature, in three-dimensional form it can be generalized as

$$\tau_{ij}^R/\rho = 2\nu_t\overline{S}_{ij} - (2/3)k\delta_{ij} \tag{2.3}$$

where $\overline{S}$ is the strain rate tensor, $\overline{S} = \frac{1}{2}\left[\frac{\partial \overline{u}_i}{\partial x_j} + \frac{\partial \overline{u}_j}{\partial x_i}\right]$. The only undefined term is the eddy viscosity ν_t in Boussinesq equation (2.3). A relation for the eddy viscosity is given by Prandtl

$$\nu_t = lV_T \tag{2.4}$$

where l is the integral length scale and V_T is a suitable measure of the fluctuations in the velocity. V_T is assumed to be equal to $\sqrt{k}$, k is the kinetic energy of the turbulence for unit mass its dimension is $\left[\frac{m^2}{s^2}\right]$. With this assumption the eddy viscosity becomes

$$\nu_t \sim \sqrt{k}l. \tag{2.5}$$

The idea is that at higher kinetic energy of the turbulence the momentum exchange will increase and this will lead to larger eddy viscosity. In this phase the relation between the dissipation rate of the kinetic energy ϵ $\left[\frac{m^2}{s^3}\right]$, the velocity and the integral scale can be utilized

$$\epsilon \sim \frac{u^3}{l}. \tag{2.6}$$

Integral scale in the last equation is substituted in the eddy viscosity relation (2.5), which yields the new form of the eddy viscosity

$$\nu_t \sim \frac{k^2}{\epsilon}. \tag{2.7}$$

The $k-\epsilon$ model uses the latter eddy viscosity relation in this form

$$\nu_t = C_\mu \frac{k^2}{\epsilon} \tag{2.8}$$

where C_μ is a constant parameter. The kinetic energy of the turbulence k and the dissipation rate of the turbulence kinetic energy ϵ are determined from the transport equations respectively for k and ϵ. The semi-empirical transport equations for k and ϵ are:

$$\underbrace{\frac{Dk}{Dt}}_{CD} = \underbrace{\frac{\tau_{ij}^R}{\rho}\overline{S}_{ij}}_{P} - \underbrace{\epsilon}_{Ds} + \underbrace{\frac{\partial}{\partial x_j}\left[\left(\nu + \frac{\nu_t}{\sigma_k}\right)\frac{\partial k}{\partial x_j}\right]}_{Df} \tag{2.9}$$

$$\underbrace{\frac{D\epsilon}{Dt}}_{CD} = \underbrace{C_{\epsilon 1}\frac{\tau_{ij}^R}{\rho}\overline{S}_{ij}\frac{\epsilon}{k}}_{P} - \underbrace{C_{\epsilon 2}\frac{\epsilon^2}{k}}_{Ds} + \underbrace{\frac{\partial}{\partial x_j}\left[\left(\nu + \frac{\nu_t}{\sigma_\epsilon}\right)\frac{\partial \epsilon}{\partial x_j}\right]}_{Df}. \tag{2.10}$$

The terms in the equation (2.9) represents:

C_μ	σ_k	$C_{\epsilon 1}$	$C_{\epsilon 2}$	σ_ϵ
0.09	1.0	1.44	1.92	1.3

Table 2.1: Standard closure coefficients of $k-\epsilon$ model (Launder & Spalding, 1974) .

- CD is the convective derivative of k.
- P is the production of the kinetic energy.
- Ds is the rate of dissipation of the kinetic energy.
- Df is the diffusion term. In the reference (Chen & Jaw, 1998) it is mentioned that the diffusion term is the only modelled term in the k equation.

The terms in the equation (2.10) represents:

- CD is the convective derivative of ϵ.
- P is the production of ϵ.
- Ds is the dissipation term.
- Df is the diffusion term. This term can be divided into molecular diffusion of ϵ and diffusion of ϵ. Respectively, the part with ν forms the molecular diffusion and the part with the ν_t forms the diffusion of ϵ.

The equations (2.8), (2.9) and (2.10) represent the $k-\epsilon$ model and are employed to calculate the eddy viscosity ν_t by equation (2.8). A transport model in the form of $k-\epsilon$ model was first proposed by (Harlow & Nakayama, 1968). The presented $k-\epsilon$ model in this section is developed by (Launder & Spalding, 1974). The constants of the $k-\epsilon$ turbulence model are called the closure coefficients, their standard values are given in Table 2.1. These constants have been tuned by using experimental data as well as numerical simulations. In the paper of (Launder & Spalding, 1974) it is mentioned that the simulations and recommendations for free shear flows on the paper (Launder, Morse, Rodi, & Spalding, 1972) are used to come up with the latest values of the closure coefficients. Moreover, in the paper of (Launder & Spalding, 1974) it is noted that the values of the constants are appropriate to plane jets and mixing layers, so basically for free shear flows. Shear flow is a flow which is predominantly one-dimensional in nature. Shear flow remote from a wall is called free shear flow. However, almost in all engineering applications there is a wall present. The standard $k-\epsilon$ model can not deal with a flow in a presence of a wall. To incorporate the presence of a wall in a flow situation wall functions are employed together with the $k-\epsilon$ model. In the next section this approach is explored.

Nowadays, there are more variants of $k-\epsilon$ model. Therefore, sometimes the presented model in this section is called the standard $k-\epsilon$ model. In this thesis, only the presented $k-\epsilon$ model is employed and analysed.

2.2.1 Wall-bounded flows

The $k-\epsilon$ model is only valid for fully developed high Reynolds number turbulent free shear flows. However, this model is often used to solve engineering applications where almost always a wall is present. Close to the wall the mean velocity decreases and at the wall it is zero, i.e. no-slip condition holds. The viscosity becomes the dominant factor close to the wall. This effect is not incorporated in the standard $k-\epsilon$ model. For wall-bounded flows the effect of the viscosity can not be ignored. In (Salim & Cheah, 2009) the performance of turbulence models are examined for wall-bounded flows by using different *near wall treatment* methods. There it is illustrated that the standard $k-\epsilon$ model needs a wall function. A wall function replaces the model equations close to the wall. To be more precise about the distance from a wall to a point in a boundary layer the non-dimensional scale y^+ is introduced. The measure in terms of y^+ of a distance y from a wall is defined as

$$y^+ = \frac{V_* y}{\nu} \tag{2.11}$$

where V_* is the friction velocity defined as $V_*^2 = \tau_w/\rho$ and τ_w is the wall shear stress.

For turbulent flows the flow close to the wall is divided in three regions (layers). This division is due to the different dominant stress factors in different layers. Very close to the wall the viscous effects are dominant and the velocity goes to zero. This layer is called the *viscous sublayer*. This layer is also responsible for the high dissipation of the turbulent kinetic energy. Outside this layer the effect of the viscosity decreases and the Reynolds stresses increase. When the viscosity effects are negligible Reynolds stresses are the dominant factor and the flow is fully turbulent. This region is called the *fully turbulent region* or the *log-law region*, the latter name comes from its velocity profile. The region between the viscous sublayer and the log-law region is called the buffer layer, which is a transition layer from viscous sublayer to the log-law region. The range of each layer is determined in terms of y^+ value, approximate values for each layer are given in Table 2.2 together with their velocity profiles.

Subdivision	Range layer	Velocity profile
Viscous sublayer	$y^+ < 5$	$\overline{u}_x = V_*^2 y/\nu$
Buffer layer	$5 < y^+ < 40$	$\overline{u}_x/V_* = f(V_* y/\nu)$
Log-law region	$y^+ > 40$	$\overline{u}_x/V_* = (1/\kappa)\ln(V_* y/\nu) + A$

Table 2.2: Subdivision of near-wall region (Davidson, 2004).

The *standard wall function* applied on the $k-\epsilon$ model is based on the velocity profile of the log-law region. Technically, that means that the first cell centre from the wall, measured in terms of y^+, should be in the log-law region. The field between the first cell centre and the wall is bridged with the standard wall function. So this area is not solved in the regular way. In this manner the mesh is made coarse near the wall and this

saves a substantial amount of computational time. At the first cell centre from the wall named Z the flux of the momentum is supposed to obey the following relation (Launder & Spalding, 1974; Hanjalic, 2004):

$$U^* = \frac{1}{\kappa} \ln E y^* \tag{2.12}$$

where

$$U^* = \frac{U_Z C_\mu^{0.25} k_Z^{0.5}}{\tau_w/\rho}$$
$$y^* = \frac{C_\mu^{0.25} k_Z^{0.5} y_Z}{\nu},$$

where κ is the von Karman constant, standard used value of it is 0.41, E is an empirical constant. U_Z, k_Z, y_Z are evaluated at the first cell centre Z. They represent respectively the mean velocity of the fluid, turbulent kinetic energy and distance from the wall to the cell centre Z.

The kinetic energy equation is solved for all the grid points. However, adjacent to the wall the diffusion term is assumed to be zero in the kinetic energy equation (2.9) and the production and the dissipation of k are computed with a different equation. The production term in the kinetic energy equation (2.9) is determined with the following expression

$$P = \tau_w \frac{\partial U}{\partial y} = \tau_w \frac{\tau_w}{\kappa \rho C_\mu^{0.25} k_Z^{0.5} y_Z}. \tag{2.13}$$

The dissipation in the k equation is evaluated with

$$\epsilon_Z = \frac{C_\mu^{0.75} k_Z^{1.5}}{\kappa y_Z}. \tag{2.14}$$

The standard way is not to solve the rate of the dissipation of the kinetic energy equation (2.10) at the first cell centre Z, instead the previous expression (2.14) is used to calculate the ϵ.

Boundary conditions imposed to the kinetic energy on the wall is $\frac{\partial k}{\partial n} = 0$, n is the local coordinate normal to the wall. This is due to the numerical concerns, it avoids underestimation of the kinetic energy and singularity of k.

Note that the presented wall function is developed for not separated flows, separation will definitely decrease the accuracy of the prediction. And it is assumed that universality holds for the viscous and logarithmic layer for wall-bounded flows. Meaning that the scaled velocity is approximately the same for different wall-bounded flows, see Table 2.2. For wall-bounded flows the standard $k-\epsilon$ model consist of the presented $k-\epsilon$ model and the presented wall function.

2.3 Distribution of the Uncertain Coefficients

The closure coefficients of the standard $k-\epsilon$ model were determined by (Launder & Spalding, 1974) for the plane jets and mixing layers. However, in almost every engineering problem the flow is bounded by a wall. The presence of a wall is incorporated in the standard $k-\epsilon$ model with the wall-function approach. Nevertheless, the values of the standard constants are kept the same as for free shear flows. Definitely, this procedure brings uncertainty in the simulations of engineering applications.

The constant parameters of the $k-\epsilon$ model and the employed wall function are assumed to be uncertain, see for the list Table 2.3. Each parameter from the list is analyzed with the aim to obtain a distribution for it, the results are presented in the subsections for each uncertain parameter.

Determining the distributions of the uncertain parameters is part of the uncertainty quantification methodology. The uncertainties are quantified in this section by find an expression for the parameter if possible, by using data from literature or/and by using expert opinion. Analytical relations are derived by applying the $k-\epsilon$ equations to a known simple flow. However, it is not possible to derive a relation for each parameter, therefore, often information from literature is used to determine the distributions. The uncertain variables in the obtained relations are propagated with the Monte Carlo method. For this purpose one million random numbers are generated according to the distribution of the uncertain variable.

Uncertain parameters		Present in equation
C_μ	Closure coefficient	eddy viscosity relation and wall function
$C_{\epsilon 1}$	Closure coefficient	production term ϵ
$C_{\epsilon 2}$	Closure coefficient	dissipation term ϵ
σ_ϵ	Closure coefficient	diffusion term ϵ
σ_k	Closure coefficient	diffusion term k
E	Smoothness of the wall	wall function
κ	Von Karman constant	wall function

Table 2.3: Parameters of the $k-\epsilon$ model and wall function that are considered as uncertain in this thesis.

2.3.1 Closure coefficient C_μ

A relation can be derived for the $k-\epsilon$ model parameter C_μ by considering the boundary layer region. In the logarithmic (log-law) layer it is assumed that the ϵ is equal to the production of k relatively at high Reynolds number, see reference (Durbin & Pettersson Reif, 2011),

$$\epsilon \approx P. \tag{2.15}$$

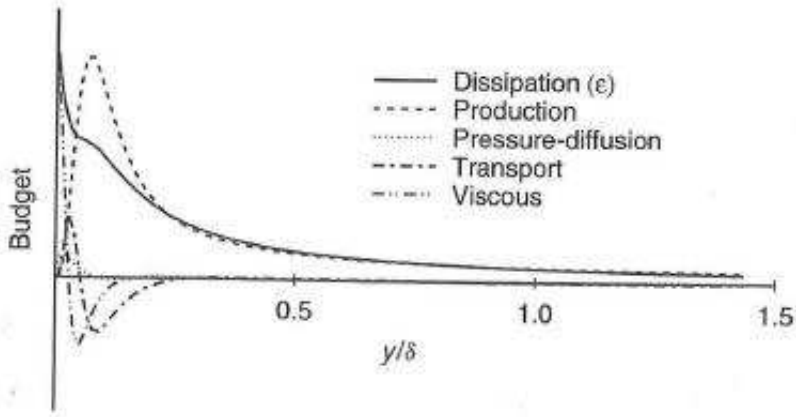

Figure 2.1: Turbulent kinetic energy budget in a boundary layer. This figure is a copy from (Durbin & Pettersson Reif, 2011).

The production term is defined as $P := -\overline{uv}\frac{\partial U}{\partial y}$ and a definition for the Reynolds stress is $-\overline{uv} := \nu_t \frac{\partial U}{\partial y}$. Multiplying the equality (2.15) with the eddy viscosity ν_t and substituting the definition of P together with the definition of the Reynolds stress yields

$$\nu_t \epsilon \approx \nu_t P = \nu_t(-\overline{uv}\frac{\partial U}{\partial y}) = (\overline{uv})^2. \tag{2.16}$$

In this phase the turbulence stress to intensity ratio $\overline{uv}/k$ can be used. In normal cases its value is assumed to be 0.3. Substituting this ratio in the equation (2.16) yields the known expression for the eddy viscosity

$$\nu_t = \frac{(0.3k)^2}{\epsilon} = C_\mu \frac{k^2}{\epsilon}. \tag{2.17}$$

However, the production of k is not exactly equal to the dissipation rate of k in the log layer. In reference (Durbin & Pettersson Reif, 2011) a turbulent kinetic energy budget is shown by using DNS data where the behaviour of production and dissipation terms are illustrated, see for the copy Figure 2.1. The Reynolds number of the boundary layer R_δ of the DNS data is 5300 which is much smaller than the considered airfoil simulation in this thesis. This could introduce an uncertainty up to five percent (from an expert opinion [1]) with the considered Reynolds number.

To account for the observed difference between the production and dissipation of k equation (2.15) is adapted to

$$P = A \cdot \epsilon, \tag{2.18}$$

where A is defined as $N(1, 0.06^2)$ to account for the inequality between the production and dissipation of k.

[1] Dr. S.J. Hulshoff, TU DELFT

The consequence of the last equation for the eddy viscosity relation (2.17) is

$$\nu_t = \frac{(0.3k)^2 \cdot N(1, 0.06^2)}{\epsilon} = 0.3^2 \cdot N(1, 0.06^2)\frac{k^2}{\epsilon}. \tag{2.19}$$

A constant value of 0.3 for the ratio of stress and intensity is used to come up with the relation (2.17). However, the ratio of turbulence stress and intensity is not constant. In (Townsend, 2003) the variability of the stress-intensity ratio $\overline{uv}/k$ is given for a group of flows, see Table 2.4. In this table distinction is made between large and small pressure gradients, however, a scale is not given for what small or large gradient is. In the airfoil simulation a large gradient occurs at the stagnation point. At other places on the airfoil the gradient is not so large as at the stagnation point. Considering the data in Table 2.4 it can be concluded that the mean value of the ratio $\overline{uv}/k$ should be smaller than 0.3 which is used in the standard case. In (Davidson, 2004) it is stated that the ratio $\frac{\overline{uv}}{k}$ is about 0.28.

Group of flows	$\overline{uv}/k$	S.D.
All	0.26	0.06
Wall layers with small pressure gradients	0.3	0.08
Wall layers with large pressure gradients	0.16	0.04

Table 2.4: Stress-Intensity ratio for different flow groups from (Townsend, 2003). S.D. denotes the standard deviation.

In the book written by (Pope, 1998) a graph is given of C_μ as a function of y^+, which is copied in Figure 2.2. That graph is obtained by direct numerical simulation for channel flows. For $y^+ > 100$ C_μ oscillates around 0.085 with an amplitude of 0.01. Between $y^+ > 40$ and $y^+ < 100$ C_μ increases from 0.04 to 0.085. For smaller y^+ values C_μ decreases linearly towards 0.005. Because the wall function is employed approximately at $y^+ \approx 40$ the C_μ value for $y^+ < 40$ is not considered in the determination of C_μ. From the figure follows that C_μ equal to 0.09 is appropriate for flows not to close to a wall, for flows adjacent to a wall its value should be decreased.

Considering these facts, the input distribution of the stress-intensity ratio is defined as $\frac{\overline{uv}}{k} = N(0.27, 0.05^2)$. The constant C_μ is then obtained with $C_\mu = N(0.27, 0.05^2)^2 \cdot N(1, 0.06^2)$. The values of C_μ in the distribution below 0.04 is truncated because of the wall function. And to prevent possible errors by applying the PC method the distribution of C_μ is truncated on the right tail for $C_\mu \geq 0.15$ where $P(C_\mu \geq 0.15) = 0.012$. The truncated distribution of C_μ is depicted in Figure 2.4a.

2.3.2 Closure Coefficient $C_{\epsilon 2}$

A relation for the closure coefficient $C_{\epsilon 2}$ can be found by assuming a decaying homogeneous, isotropic turbulence. The homogeneous turbulence flow means a flow in which the

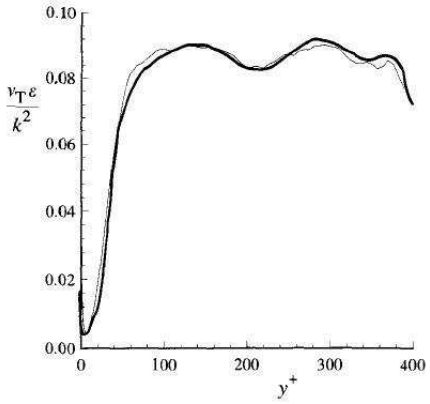

Figure 2.2: The profile of C_μ from DNS of channel flow from (Pope, 1998).

statistics are not dependent of position. Isotropic turbulence is a turbulent flow where the statistical properties of the fluctuations have no directional preference. For the decaying turbulence the $k-\epsilon$ model simplifies to

$$\frac{dk}{dt} = -\epsilon \tag{2.20}$$

$$\frac{d\epsilon}{dt} = -C_{\epsilon 2}\frac{\epsilon^2}{k}. \tag{2.21}$$

A power law solution is sought for the simplified equations

$$k = \frac{k_0}{(t/t_0+1)^n}. \tag{2.22}$$

Putting the last equation in the simplified equations of the model and after some algebra an expression for the coefficient $C_{\epsilon 2}$ is obtained as a function of the decay exponent n

$$C_{\epsilon 2} = \frac{n+1}{n} \tag{2.23}$$

By fitting the curve $k = k_0(x/x_0+1)^{-n}$ through measurements of grid generated turbulence in a wind tunnel, the decay exponent n can be found. For the standard value of $C_{\epsilon 2}$ equation (2.23) gives a decay exponent of 1.087. However, in the references (Durbin & Pettersson Reif, 2011; Pope, 1998) it is stated that the decay exponent has a variability with a range of 1.3 ± 0.2. In another source (Wilcox, 1994) the decay exponent is given in a narrower range, $n = 1.25 \pm 0.06$. Which shows the clustering of the decay component around a mean. (Mohamed & LaRue, 1990) suggest that the decay exponent is clustered around 1.3. In reference (Comte-Bellot & Corrsin, 1966), the values of the decaying exponent for small changes in the set-up like the mean velocity and the grid layout are tabulated, see for the copy of the values Table 2.5.

Mean Velocity [m/s]	10	20	8.5	10	10	20	20
n	1.33	1.27	1.27	1.26	1.25	1.27	1.24
Mean velocity [m/s]	27	10	20	10	20	10	20
n	1.22	1.19	1.18	1.3	1.27	1.33	1.39

Table 2.5: Decay exponent of grid turbulence from (Comte-Bellot & Corrsin, 1966).

From the data in Table 2.5 a normal distribution is defined for n. The obtained distribution in this way for the decay exponent n is $N(1.27, 0.055^2)$ which is in agreement with the data from other mentioned sources. Subsequently, the distribution of $C_{\epsilon 2}$ is obtained by using the relation (2.23). The left and right tails are truncated due to the application of PC method respectively for $C_{\epsilon 2} \leq 1.7$ and $C_{\epsilon 2} \geq 1.9$ where the probabilities are $P(C_{\epsilon 2} \leq 1.7) = 0.002$ and $P(C_{\epsilon 2} \geq 1.9) = 0.002$. The truncated distribution of $C_{\epsilon 2}$ is depicted in Figure 2.4b.

2.3.3 Closure Coefficient σ_ϵ

The σ_ϵ constant is present in the diffusion term of the ϵ equation. In the subsection for $C_{\epsilon 1}$ the relation (2.29) is derived for the logarithmic layer where the constant σ_ϵ is present. However, using that equation with the defined distributions yields convergence problems. Therefore, expert opinion is used to get a distribution for this constant. In the book of (Chen & Jaw, 1998) it is mentioned that the value of σ_ϵ is in the range of [1,1.3]. Because there was no other data about this coefficient that range is used to define the uniform distribution $U(1, 1.3)$ for σ_ϵ, see Figure 2.4e.

2.3.4 Von Karman constant κ

The Von Karman constant κ is present in the expression that defines the logarithmic velocity profile near a boundary. Because the presence of κ in the wall function its value in the log layer is required. Although its name suggest a constant the Von Karman constant is not constant of nature, in the source (Durbin & Pettersson Reif, 2011) κ is given in the range 0.41 ± 0.2. In the reference (Osterlund, Johansson, Nagib, & Hites, 2000) κ is investigated along y^+, for the desired logarithmic layer its value varies between 0.37 and 0.44. To contain the specified range in the literature for κ a uniform distribution of $U(0.37, 0.44)$ is defined, see Figure 2.4f.

2.3.5 Closure Coefficient $C_{\epsilon 1}$

The standard value of the closure coefficient $C_{\epsilon 1}$ is fixed by examining the model behaviour for the spreading rate in a plane mixing layer, see reference (Launder, 1972). The difference between the constants $C_{\epsilon 2}$ and $C_{\epsilon 1}$ is a measure of the spreading rate of free shear flows, see (Durbin & Pettersson Reif, 2011). This parameter can be calibrated

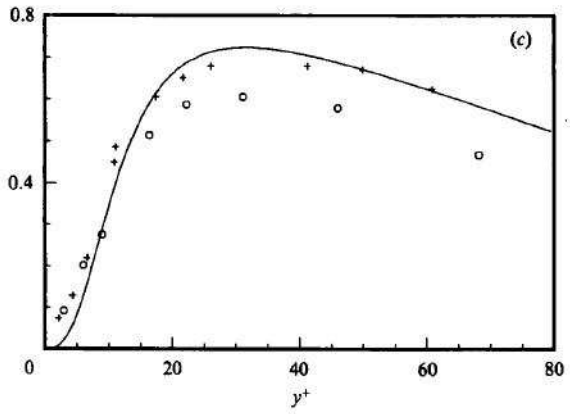

Figure 2.3: The Reynolds shear stress $-\overline{uv}$ normalized by the wall shear velocity from (Kim et al., 1987).

by using growth rates of homogenous sheared turbulence in relation with the following expression

$$\frac{P}{\epsilon} - 1 = \frac{C_{\epsilon 2} - C_{\epsilon 1}}{C_{\epsilon 1} - 1}. \tag{2.24}$$

This relation expresses the growth rate to the excess of the production P to the dissipation ϵ. However, employing this relation yields convergence problems. Therefore, a different method is applied to find an appropriate distribution of $C_{\epsilon 1}$. An expression is derived for the logarithmic layer that provides a distribution of $C_{\epsilon 1}$.

In the logarithmic layer it is assumed that the production is approximately equal to the dissipation. This approximation was also used for the determination of the distribution C_μ. There it is shown that, actually, $P = A \cdot \epsilon$, where A is defined as $N(1, 0.06^2)$. Furthermore, in the log layer it is assumed that the stress is constant $-\overline{uv} = V_*^2$ and that the log law can be stated as $\frac{\partial U}{\partial y} = \frac{V_*}{\kappa y}$. However, in Figure 2.3 it is shown by using the DNS results and experimental results that the assumption $-\overline{uv} = V_*^2$ is not true. Actually it is dependent on y^+. The deviation in the constant-stress layer assumption is corrected with the normal distributed correction term of $N\left(0.68, 0.02^2\right)$ so $-\overline{uv} = V_*^2 \cdot N\left(0.68, 0.02^2\right)$.

Substituting the assumption for the Reynolds stress term in the definition of the production term together with the relation for $\frac{\partial U}{\partial y}$ yields

$$P = -\overline{uv}\frac{\partial U}{\partial y} = N\left(0.68, 0.02^2\right) \cdot \frac{V_*^3}{\kappa y}. \tag{2.25}$$

Hence, the relation between the production P and the dissipation ϵ is

$$P \cdot N(1, 0.06^2) = N\left(0.68, 0.02^2\right) \cdot N(1, 0.06^2)\frac{V_*^3}{\kappa y} = \epsilon. \tag{2.26}$$

The eddy viscosity can be written in a different form by using the assumption for the constant-stress layer and the relation for the $\frac{\partial U}{\partial y}$. The eddy viscosity gets the form

$$\nu_t \equiv \frac{\overline{uv}}{\frac{\partial U}{\partial y}} = N\left(0.68, 0.02^2\right) \cdot \kappa y V_*. \tag{2.27}$$

The $k-\epsilon$ model uses a different form to calculate the eddy viscosity namely $\nu_t = C_\mu \frac{k^2}{\epsilon}$. This implies together with the equation (2.26) that

$$N\left(0.68, 0.02^2\right) \cdot \kappa y V_* = \frac{C_\mu k^2 y}{N\left(0.68, 0.02^2\right) \cdot N(1, 0.06^2) V_*^3}. \tag{2.28}$$

Solving the latter equation for k gives $k = \frac{N\left(0.68,0.02^2\right)\cdot\sqrt{N(1,0.06^2)}V_*^2}{\sqrt{C_\mu}}$. Substituting the derived equations for k, ν_t and ϵ in the transport equation for ϵ (2.10) yields the following relation

$$C_{\epsilon 2} - C_{\epsilon 1} = \frac{N\left(0.68, 0.02^2\right)\kappa^2}{\sqrt{N(1, 0.06^2)}\sigma_\epsilon \sqrt{C_\mu}}. \tag{2.29}$$

By using the already defined distributions of κ, σ_ϵ, $C_{\epsilon 2}$ and C_μ in the latter equation the distribution of $C_{\epsilon 1}$ is determined see Figure 2.4c. The distribution of $C_{\epsilon 1}$ is truncated before applying the PC method at the left and the right tail for $C_{\epsilon 1} \leq 1.18$ and $C_{\epsilon 1} \geq 1.61$ with the probability $P(C_{\epsilon 1} \leq 1.18) = 0.0054$ and $P(C_{\epsilon 1} \geq 1.61) = 0.0078$.

2.3.6 Closure Coefficient σ_k

The diffusion in the k equation is modelled with

$$\mathbf{T} = -\alpha_t \nabla k \tag{2.30}$$

where α_t is some unknown diffusivity. In the k equation this diffusivity is taken as $\alpha_t = \nu + \frac{\nu_t}{\sigma_k}$. The constant σ_k is defined to make the diffusivity flexible, however, in the most cases σ_k is assumed to be one. Even in some literature this constant is not mentioned at all and it is not programmed in the standard version of the OpenFOAM. In the reference (Chen & Jaw, 1998) the range of this constant is stated between 0.8 - 1. By using this range a uniform distribution $\sigma_k = U\,(0.8, 1)$ is defined, see Figure 2.4g.

2.3.7 Smoothness parameter E

To take into account the smoothness of the wall, the smoothness parameter E is present in the standard wall function. This parameter is also inserted in the wall function to have more control on the wall function and to adapt its value to empirical observations. To see the effect of variations in this parameter it is assumed to be variable. In the original paper

where $k-\epsilon$ model is explained (Launder & Spalding, 1974) a value of $E = 9.0$ is stated for smooth walls, in OpenFOAM and (Fluent, n.d.) the standard programmed value of E is 9.8. However, what value E should have for rough walls is not stated. The object in the simulations in this thesis is an airfoil which can be considered as a smooth object. Because E is also inserted in the wall function to have more control on the wall function a normal distribution is considered with a standard deviation of one, $E = N(9.8, 1)$. The distribution of E is shown in Figure 2.4d. On both sides the tails are truncated before applying the PC method for $E \leq 7$ and $E \geq 12.6$ with the probabilities $P(E \leq 7) = 0.003$ and $P(E \geq 12.6) = 0.003$.

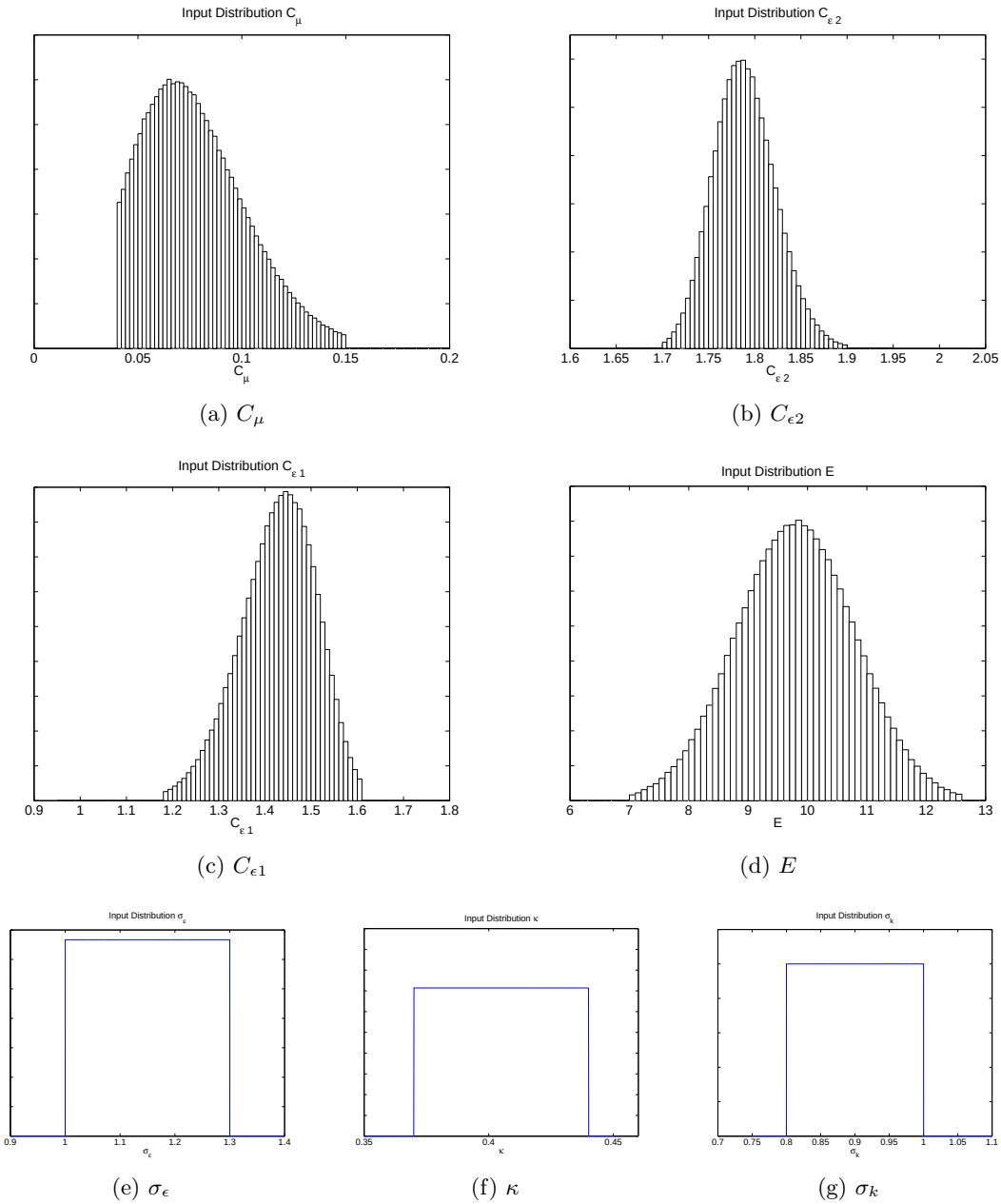

(a) C_μ (b) $C_{\epsilon 2}$

(c) $C_{\epsilon 1}$ (d) E

(e) σ_ϵ (f) κ (g) σ_k

Figure 2.4: The determined distributions of the standard $k - \epsilon$ model parameters.

Chapter 3

Numerical Setup, Deterministic Simulations and Experimental Data

This chapter forms the numerical/technical bridge to the uncertainty quantification analysis. To get the desired outputs from the turbulent flow around the airfoil DU96-W-180 numerical simulation techniques are employed. This chapter gives information about the numerical setup of the simulations and it illustrates the solved state variables around the airfoil DU96-W-180. The setup of the simulations is explained in Section 3.1. A mesh convergence study is performed in Section 3.2 to obtain a mesh which results in less discretization error and affordable computational time. The results of the solved state variables are presented in Section 3.3 together with the pressure coefficient C_p and the skin friction coefficient c_f. The deterministic numerical results of the lift and drag coefficients for different angles of attack are compared with the experimental data in Section 3.4. As last in this chapter the uncertainties in the experimental data are estimated in Section 3.5.

3.1 Performing the simulations

The meshes are generated with the software Pointwise and have a circular framework called the O-type mesh. The simulations are performed with the software OpenFOAM. OpenFOAM comprises many solvers that are designed to solve specific problems in continuum mechanics. Besides the solvers, there are utilities available for pre- and post-processing of the data. The solver that is build to solve the incompressible turbulent flow by using the RANS equations is the *simpleFoam*. As stated in the user guide of (OpenFOAM Team, 2011) simpleFoam is a steady-state solver for incompressible turbulent flow.

The name of the solver simpleFoam is derived from the algorithm that is used to solve the RANS equations. The algorithm that is used is called the semi-implicit method for pressure-linked equations (SIMPLE), this method has been developed by (Patankar &

Spalding, 1972) especially to solve the steady-state problems. The main idea is to apply a pressure correction formula $p = p^* + p'$ where p^* is the first guess value, hereafter p' is determined which is called the pressure correction term. Next, p is updated and p^* gets the value of p for the next iteration. The SIMPLE algorithm is explained in detail by (Anderson, 1995). The underrelaxation technique is used to improve the stability of the simulation. Further second-order schemes are used for the pressure and the velocity and first-order schemes are used for the k and the ϵ.

Specification of the boundary conditions for k and ϵ

The boundary conditions for the k and the ϵ are based on some assumptions and relations. The flow in a wind tunnel has turbulent variations. This imperfection can be measured and it is called the turbulence intensity I. The definition of it is $\frac{u'}{U}$, herein u' is the standard deviation of the turbulent fluctuation and U is the mean velocity. The experimental data used in this thesis comes from a wind tunnel where the turbulence intensity of the wind tunnel is given as a function of the freestream velocity in (Timmer & Rooij, 2003). There is no data available about the real turbulence intensity in case of turbulent flow around an airfoil. Therefore, the turbulence intensity of the wind tunnel is used for the simulations. A formula is given in the user guide of (OpenFOAM Team, 2011) to calculate the k just in front of the airfoil

$$k_{airfoil} = 1.5(V_\infty \frac{I}{100})^2, \tag{3.1}$$

where V_∞ is the freestream velocity. The simulated turbulent flow is of a decaying type. Thus, the turbulent kinetic energy has to reach the value $k_{airfoil}$ just in front of the airfoil. The horizontal distance x from the airfoil to the framework of the mesh is used to define the k_∞ at the mesh boundary, see Figure (3.1), with the following formula (Platteeuw, 2008)

$$k_\infty = \frac{k_{airfoil}}{x^{-n}}, \tag{3.2}$$

where n is the decay exponent. The kinetic energy of the decaying turbulence is governed by the equation $V_\infty \frac{\partial k}{\partial x} = -\epsilon$. From this equation the ϵ can be obtained at the boundary of the mesh

$$\epsilon_\infty = n \cdot V_\infty \cdot k_\infty. \tag{3.3}$$

For the initial condition of the ϵ the following relation is used (OpenFOAM Team, 2011)

$$\epsilon_{airfoil} = \frac{C_\mu^{0.75} k_{airfoil}^{1.5}}{l} \tag{3.4}$$

where l is the turbulent length scale.

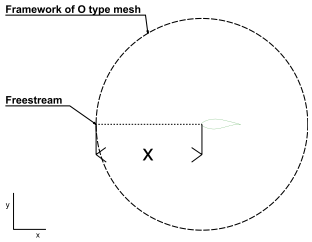

Figure 3.1: View of the numerical setup.

3.2 Mesh Convergence Study

It is important for the UQ analysis that the discretization error is small with respect to the effects of the uncertainty. Therefore, a convergence study is performed in this section. Since the partial differential equations (pde) are discretized on discrete points, increasing grid density will approximate the real solution to the pde more accurately.

The disturbances in an incompressible flow travel in all the directions. Hence, the freestream conditions should be reached at the boundary of the mesh without introducing non-physical gradients. Furthermore, the discrepancy between the obtained mesh and theoretical infinite large mesh should be not too large in the sense that the numerical errors should not play a role in the UQ analysis. The largest generated mesh, in number of cells, is assumed as the infinite large mesh. The following two steps are carried out to obtain a mesh for UQ analysis

1. The distance of the airfoil to the inflow/outflow is determined. This distance is called the farfield length.
2. The mesh density is increased in overall domain. The effect of the y^+ value is considered by the end choice of the mesh on which subsequent simulations are performed.

3.2.1 Determination of the Farfield Length

The farfield length can be seen as the distance where the inflow is started with the defined freestream properties to the airfoil. Because the framework of the mesh has almost a circular shape the farfield length can be considered as the radius of the circle.

The simulations to determine the farfield length are done at a Reynolds number of $3 \cdot 10^6$ and at an angle of attack α of $0.42°$.

The force coefficients C_l and C_d are plotted for varying farfield lengths in Figure 3.2. An asymptotical convergence can be seen in Figure 3.2 for C_l and C_d. However after about 23 metre there is a small non-convergent behaviour. This can be caused due to the different boundary conditions for k and ϵ at each mesh. Although the conditions are determined by the same formula the decay of the turbulence is not exactly the same in each mesh.

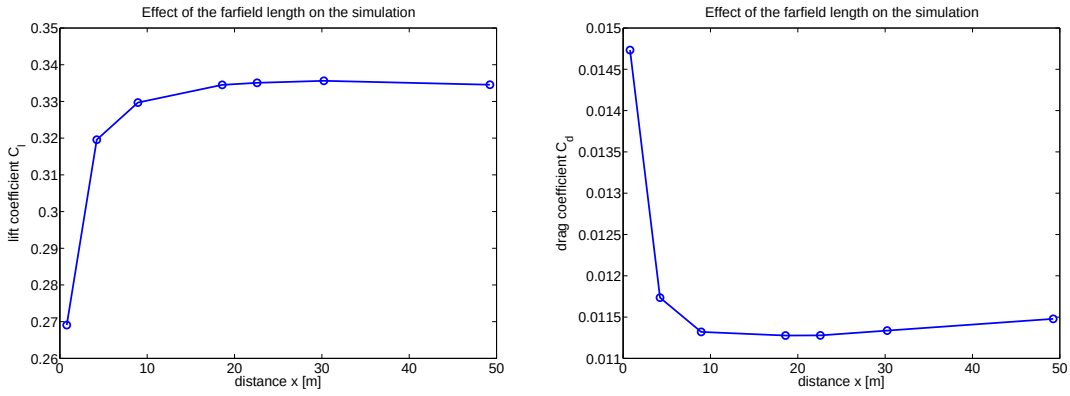

(a) C_l (b) C_d

Figure 3.2: Force coefficients as a function of farfield length.

Other reasons for the undesired behaviour are the presence of spacing constraints in the mesh, the wall function and the different length scales that are solved. Neglecting the non-convergent behaviour, the farfield length is determined as 20 metre which is $33.3c$ where c is the chord of the airfoil which is 0.6 m. From now on the farfield length of the generated meshes is larger and close to 20 metre. The exact farfield length can not be specified with Pointwise.

3.2.2 Increasing overall mesh density

The overall mesh density is increased by increasing the grid points along the airfoil and by decreasing the growth rate of the cells. In this manner the mesh density is increased in two directions. From now on the simulations are done at Reynolds number $2 \cdot 10^6$, Mach number 0.15 and angle of attack 1.45°. There is experimental data available of fully developed turbulent flow over the airfoil DU96-W-180 for these conditions. Eventually that experimental data is used for the UQ and calibration analyses of the $k-\epsilon$ model.

To see the effect of the y^+ value on the result two different kind of meshes are generated. The difference between these meshes is the distance of the first cell to the wall. One has a distance of 0.0004m and the other has a distance of 0.0005m to the first cell. The force coefficients from the simulations are plotted in Figure 3.3 as a function of number of cells in the mesh. An asymptotical convergence can be seen for both force coefficients as the total cells increases. However, it is obvious that after almost 1.5 million cells a total convergence is not reached. The main reason therefore is the different solved length scales. The result of the largest mesh is assumed to be converged for making further decisions. The error that is introduced because of this assumption is very small. The discrepancy of the simulations in absolute percents with respect to the greatest grid are plotted in Figure 3.4.

Not only the accuracy of the result is important for choosing the right mesh. The computational time is also a decisive factor. Especially in the context of uncertainty quantification the time required to simulate the problem should not be too excessive. The

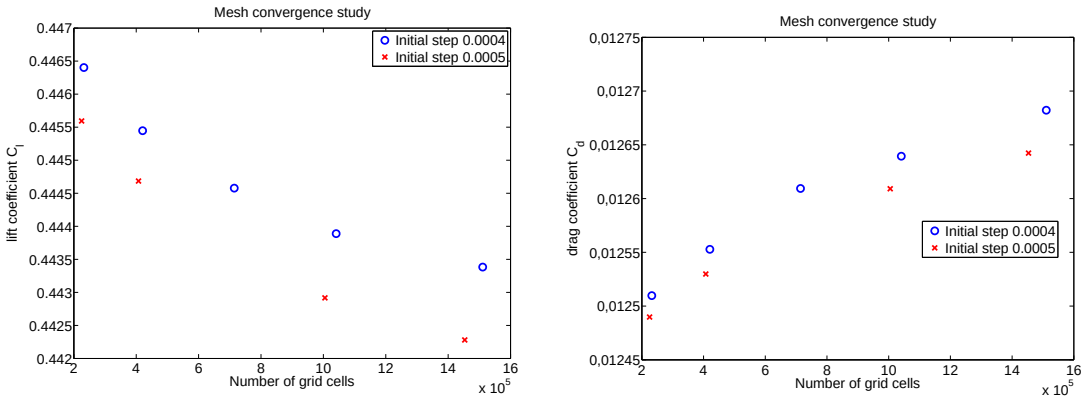

(a) C_l (b) C_d

Figure 3.3: Force coefficients as a function of total cells.

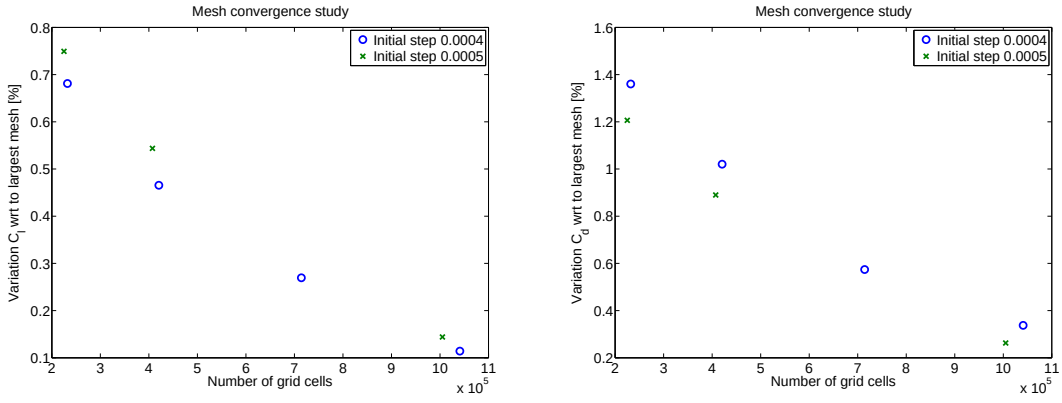

(a) C_l (b) C_d

Figure 3.4: Discrepancy of the force coefficients with respect to the results of the largest mesh.

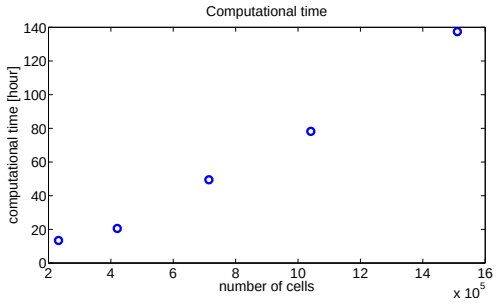

Figure 3.5: Required computational time to converge.

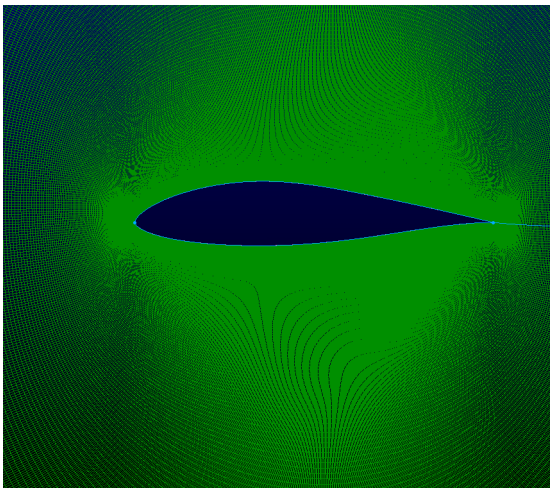

Figure 3.6: A close-up of the final mesh around the airfoil.

required computational time to have a converged simulation is depicted in Figure 3.5. As it is expected the required time for convergence increases with increasing mesh density.

The meshes with the different first cell distance show similar convergence behaviour. However, the y^+ values of the meshes with the first cell distance of 0.0005 m are more in the favourable layer. So, the first cell distance of 0.0005 is used at further simulations. Considering the discrepancy of the results with respect to the mesh with the largest number of cells and the computational time the mesh with total cells of 407320 is chosen for further simulations. Which has a discrepancy of 0.5438 % for C_l and -0.8899 % for C_d with respect to the largest mesh. A close-up of the selected mesh for UQ analysis around the airfoil is given in Figure 3.6

The order of the simulations is close to one. This is illustrated in Figure 3.7.

In the previous section it was mentioned that the kinetic energy decays. To confirm this behaviour k is plotted in Figure 3.8a from the inflow towards the airfoil. The pressure residual for the converged mesh is shown in Figure 3.8b to illustrate the convergence. The force coefficients are converged after 16000 iterations. After this iteration number the pressure residual shows no improvement which also confirms the achieved convergence.

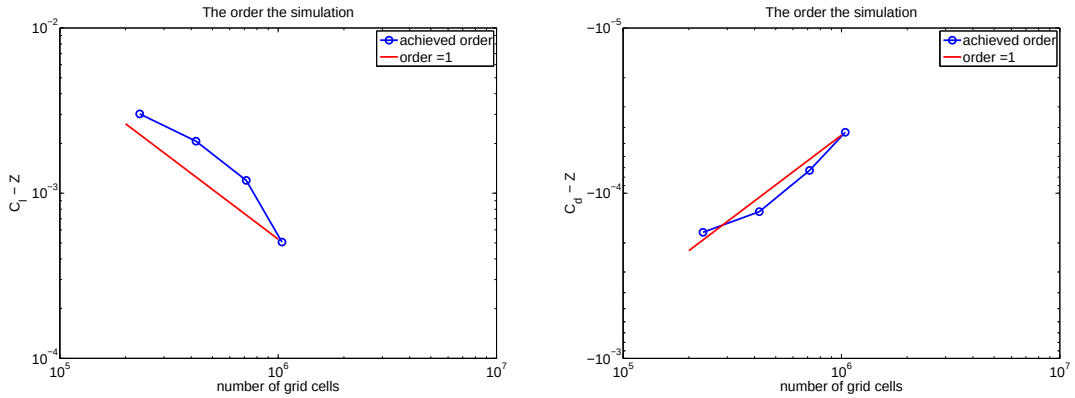

(a) C_l (b) C_d

Figure 3.7: Order of the simulation with respect to the results of the largest mesh which is denoted as Z in the figure. Exact order one is also illustrated.

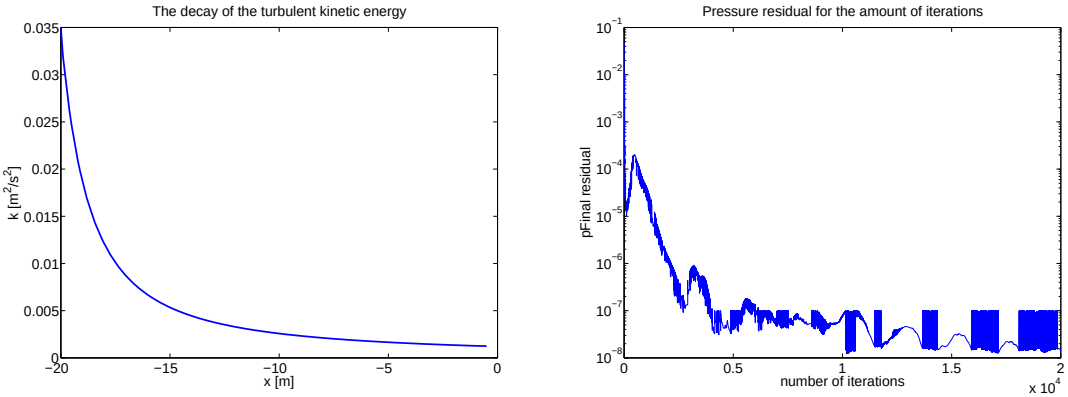

(a) The decay of the k in the simulation. (b) Pressure residual.

Figure 3.8: The decay of k in (a) and the pressure residual in (b).

3.3 Results from the simulation

The variables that are solved by using the RANS and the standard $k-\epsilon$ model are p, $\mathbf{u}$, k, ϵ and ν_t. The solution of those variables are presented in this section for the simulation with the selected mesh in Section 3.2 at $R = 2 \cdot 10^6$, $M = 0.15$ and $\alpha = 1.45°$. The presented figures give an idea about the correctness of the simulations and familiarize the reader to the solved problem. The solution of the five state variables are illustrated in Figure 3.9.

The value of the pressure field is relative because the simulation is performed at incompressible flow conditions. The coupling between the pressure and the velocity field is obvious. Higher intensity of k is observed near the airfoil. In reference (Durbin & Pettersson Reif, 2011) it is mentioned that the $k - \epsilon$ model predicts larger k around the stagnation point, the production term of k (2.9) rises too much near the stagnation point and the leading edge curvature. The ϵ has very high values just near the airfoil surface.

Outside this small layer its value decreases towards the normal value of the flow. The maximum eddy viscosity is present just at the trailing edge and at the flow behind the airfoil. Behind the airfoil the eddy viscosity dies down slowly.

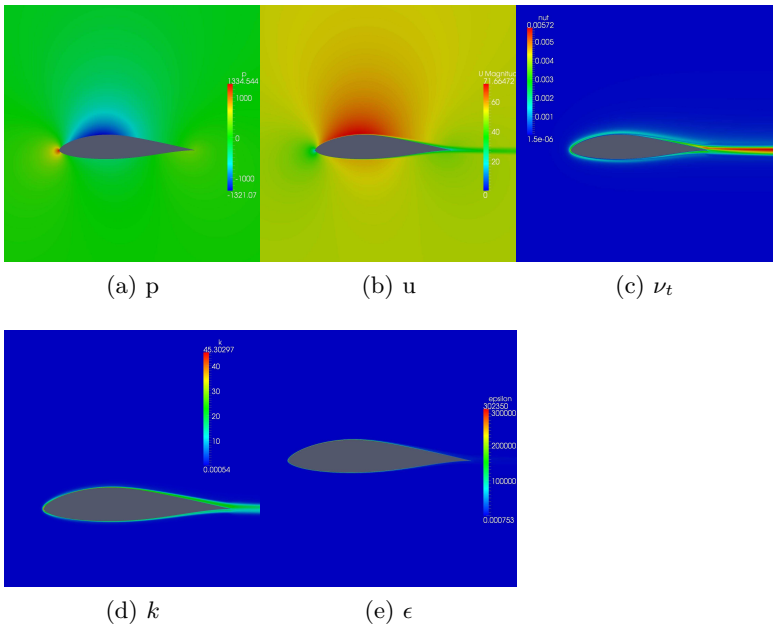

(a) p (b) u (c) ν_t

(d) k (e) ϵ

Figure 3.9: The numerical solution of the state variables (a) p, (b) u, (c) ν_t, (d) k and (e) ϵ around the airfoil DU96-W-180.

The pressure coefficient C_p and the skin friction c_f on the upper and the lower surface are shown in Figure 3.10. The wiggles on the C_p and c_f are mainly caused because of the piecewise linearly constructed airfoil shape with only 200 points. This is discovered after the analyses were performed with the current mesh. However, the error in the force coefficients due to the introduced uncertainty in the airfoil geometry is smaller than 0.05 %. A calculation based on the performed simulation showed that 90 % of the drag is caused by the pressure.

3.4 Comparison of numerical simulations and experimental results

The experimental data of the airfoil DU96-W-180 consists of measurements for 24 different angles of attack α (also denoted as AoA) in the range -4.71 to 14.64 degrees. The measurements were carried out on fully developed turbulent flow conditions at $R = 2 \cdot 10^6$ and $M = 0.15$. To compare the experimental data with the deterministic results of the standard $k - \epsilon$ model the turbulent flow over the airfoil is simulated for fifteen different angles of attack. The experimental data and the results of the numerical simulations for C_l and C_d and the discrepancy between the experimental and numerical data are plotted

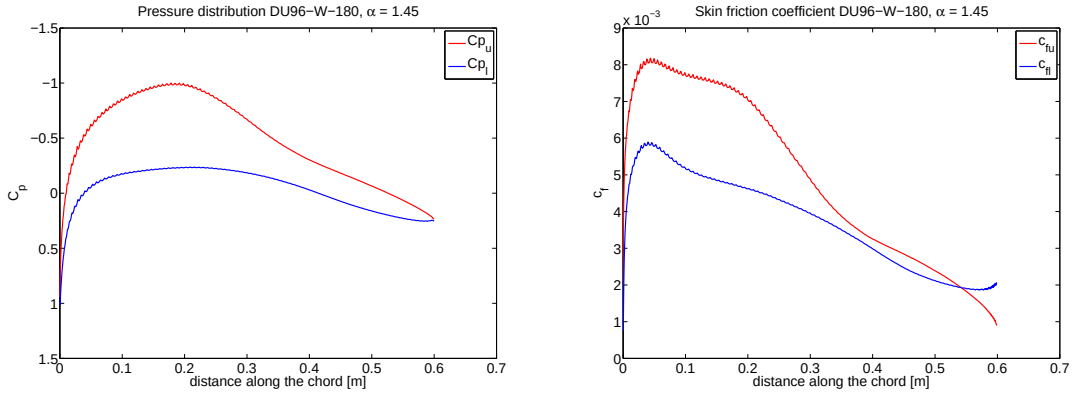

(a) C_p (b) c_f

Figure 3.10: The C_p and c_f around the airfoil DU96-W-180.

in Figure 3.11.

First, the experimental results are discussed:

- The lift coefficient varies almost linearly with angle of attack for low-to-moderate angles of attack. It increases up to 10.15 degrees, from that point the lift coefficient starts to decrease. Which shows that the airfoil is stalled after an angle of attack of 10.15 degrees. Stalled airfoil occurs due to the flow separation which occurs generally at relatively high angles of attack. Stalled airfoil leads to precipitous decrease in lift and increase in drag.

Secondly, the experimental data is compared with the numerical results:

- The prediction of C_l by the $k-\epsilon$ model agrees quite well up to the stalled airfoil. After the stalled airfoil the lift coefficient continues to increase in the numerical results. The $k-\epsilon$ model has more difficulty with the prediction of the drag coefficient. Approximately between 5 and 9 degrees it is overpredicting the drag and after the stalled airfoil the drag does not increase enough to catch up the experimental results. From the stalled airfoil the discrepancy between the experimental and numerical data grows. Besides, the $k-\epsilon$ model has not the ability to account for the effects of the separation. Neither has the employed wall function the capability to simulate the separation correctly. Therefore, for the calibration process the stalled airfoil data is not used.

3.5 Uncertainty in experimental data

The experimental data contains uncertainties which can be caused by many factors like the small differences in the inlet conditions, measurement errors by the apparatus. For

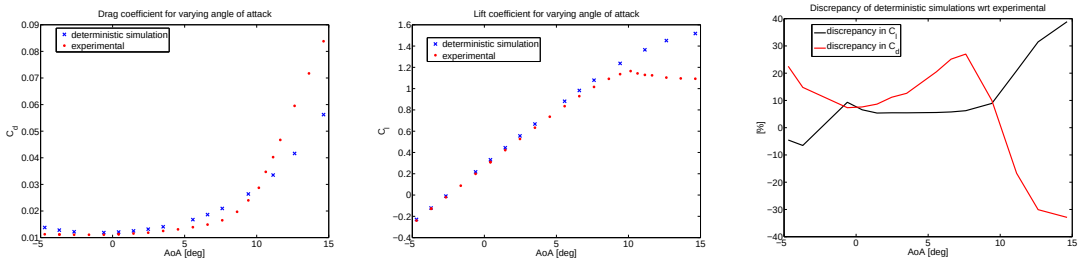

(a) C_d (b) C_l (c)

Figure 3.11: The experimental and numerical results for C_d and C_l. The discrepancy of the numerical simulations with respect to the experimental data [%] is shown in (c).

instance, the experiments with the airfoil DU96-W-180 are carried out two times almost at the same angle of attack, namely at α 0.42° and 0.421°. Nevertheless, the results have still different force coefficients which indicate definitely the presence of uncertainties. These measurements and the polynomial regression analysis are used to make a guess of the experimental error. Because of the large influence of separation on the results the regression analysis are carried out for a limited angles of attack of $[-4.71°, 7.61°]$ for which C_l is expected to be linear. The polynomial regression analysis of linear polynomial has the following form

$$Y = \beta_0 + \beta_1 x + \epsilon \tag{3.5}$$

where Y is the random variable, x is called the regressor and ϵ is the random error and β_0 and β_1 are the regression coefficients. It is assumed that the error term is normal distributed with mean zero and variance σ^2. The method of least squares is used to estimate the regression coefficients of the polynomial. In matrix form the method of least squares is

$$(\mathbf{X}^T\mathbf{X})\boldsymbol{\beta} = \mathbf{X}^T\mathbf{y}. \tag{3.6}$$

$\boldsymbol{\beta}$ is the matrix with the regression coefficients, $\boldsymbol{X}$ is the regressor and $\boldsymbol{y}$ is the response variable. $\mathbf{X}$ and $\mathbf{y}$ are defined in the following form

$$X = \begin{pmatrix} 1 & x_1 & x_1^2 & \dots & x_1^m \\ 1 & x_2 & x_2^2 & \dots & x_2^m \\ 1 & \dots & \dots & \dots & \dots \\ 1 & x_n & x_n^2 & \dots & x_n^m \end{pmatrix}$$

$$\boldsymbol{y} = \begin{bmatrix} y_1 & \dots & y_n \end{bmatrix}^T,$$

where n is the number of data points and m is the order of the polynomial. The polynomial fitting is performed for orders one to four for the experimental data of C_l and C_d see

	C_l	C_d
σ	0.0035	0.0000777

Table 3.1: The standard deviations of the experimental uncertainty.

Figures 3.12a and 3.12b. After the regression coefficients are determined the variance of the random error can be determined with the equation

$$\sigma^2 = \frac{SS_E}{n-p} \tag{3.7}$$

where p is the dimension of the $\boldsymbol{\beta}$ matrix $(p \times 1)$. SS_E is defined as

$$\sum_{i=1}^{n} (y_i - \hat{y}_i)^2 \tag{3.8}$$

where $\hat{y}$ represents the result of the fitted polynomial and y is the experimental data.

At two different AoA there are two sets of measurements available. These data is used to calculate the average variation in the experimental data. In that way obtained experimental variation and the determined standard deviation from the regression analysis for one to four orders are shown in Figures 3.12c and 3.12d. The standard deviation of C_d agrees well with the experimental variation for cubic polynomial. The standard deviation of C_l is converged for cubic polynomial which has lower value than the experimental variation. To certainly capture the value of the experimental variation its value is defined as the standard deviation of the experimental error of C_l. The standard deviation of the measurements error of C_d is taken as the standard deviation of cubic regression analysis. The standard deviations of C_l and C_d of the uncertainty in the experimental data are summarized in Table 3.1. These standard deviations are used in the calibration process.

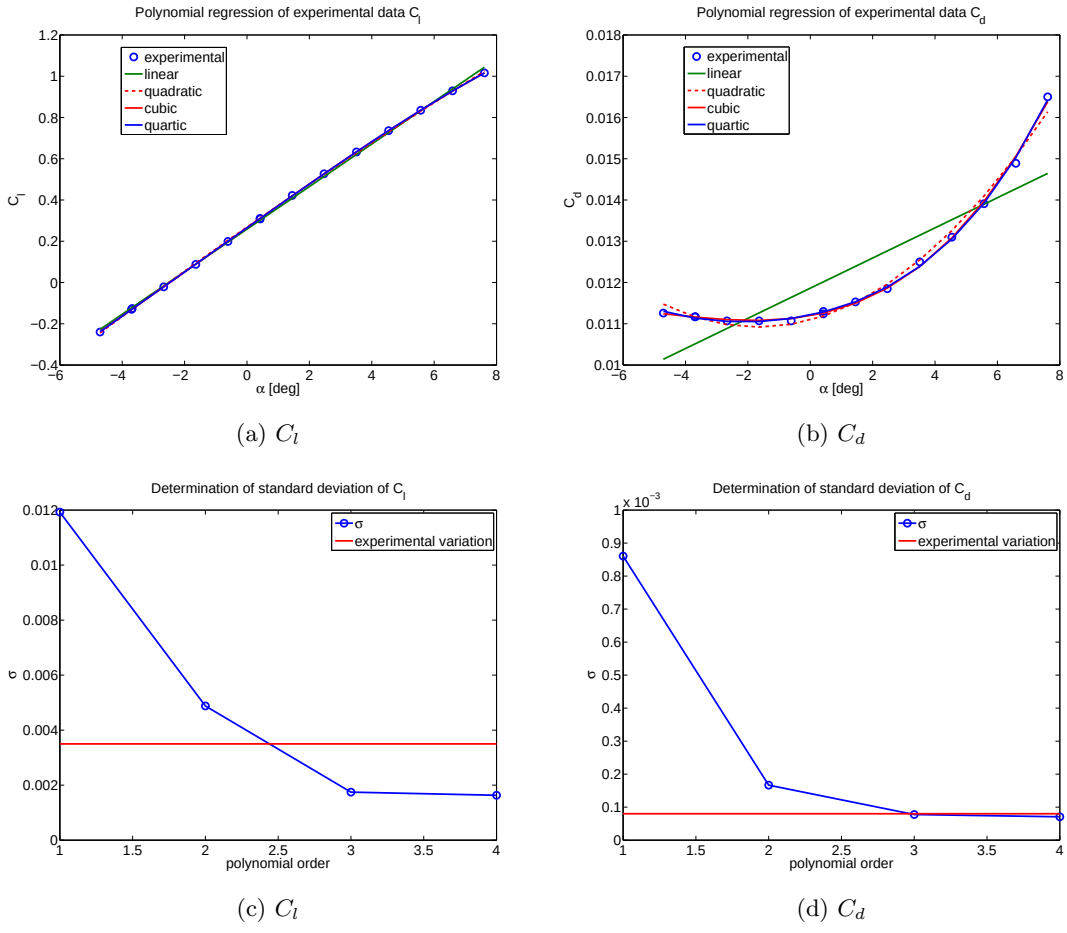

(a) C_l (b) C_d

(c) C_l (d) C_d

Figure 3.12: Polynomial regression analysis to find the standard deviation of C_l and C_d from the experimental data.

Chapter 4

Propagating Uncertainty with Probabilistic Collocation

The next step in the uncertainty quantification (UQ) process is the propagation of the uncertainties in the model parameters through the $k-\epsilon$ model to quantify the effects of the uncertainties on the force coefficients. For that purpose the Probabilistic Collocation (PC) method is very appropriate. The derivation of PC method is illustrated in Section 4.1. Subsequently, UQ analysis is performed for one, three and five dimensions (1-D, 3-D and 5-D) respectively in Sections 4.2, 4.3 and 4.4 at $\alpha = 1.45°$. 5-D UQ analysis is performed at the angles of attack of 1.45°, 4.54° and 7.61°. As a result of the analysis the response surfaces and the probability density functions of C_l and C_d are presented. For the 5-D analysis the seven uncertain parameters are reduced to five by discarding the less influential parameters. There are arisen convergence problems for some of the required simulations. One example of such a case is illustrated in Section 4.5.

4.1 Probabilistic Collocation method

The uncertainty can be propagated efficiently, especially for not too many uncertain parameters, with the Probabilistic Collocation method. The PC method is developed by (Babuska et al., 2007) and (G. J. A. Loeven et al., 2007) independently of each other. The derivation of the PC method and its properties are stated in this section.

Normally, fixed input values are used to obtain the output of a model. However, by assuming at least one parameter of a model as random the problem becomes stochastic. Mathematically, the solution of a stochastic problem is given in this way $u(\mathbf{x}, t, \omega)$ where $\mathbf{x}$ denotes position, t is time and ω denotes the stochasticity of the solution. The solution is represented by a polynomial chaos framework which divides the problem in a deterministic

and a stochastic part. The solution by PC method is represented as

$$u(\boldsymbol{x}, t, \omega) \approx \sum_{i}^{N_p} u_i(\boldsymbol{x}, t) L_i(\boldsymbol{\xi}(\omega)) \tag{4.1}$$

where N_p is the number of collocation points for a polynomial of order p, $\boldsymbol{\xi}$ is the random basis for number of uncertain parameters and L_i represents the Lagrange basis polynomials which are defined as

$$L_i(\boldsymbol{\xi}(\omega)) = \prod_{j=1, j\neq i}^{N_p} \frac{\boldsymbol{\xi}(\omega) - \boldsymbol{\xi}(\omega_j)}{\boldsymbol{\xi}(\omega_i - \boldsymbol{\xi}(\omega_j)}. \tag{4.2}$$

Very nice property of the Lagrange basis polynomials is that they possess the property of the Kronecker delta $L_i(\boldsymbol{\xi}(\omega_j)) = \delta_{ij}$.

The principles of the PC method is demonstrated by using the following general stochastic differential equation

$$D\left(\mathbf{x}, t, \omega; u(\mathbf{x}, t, \omega)\right) = S\left(\mathbf{x}, t, \omega\right) \tag{4.3}$$

in this equation D is a differential operator, the solution depends on $\mathbf{x}$, t and ω, S represents a source term and the solution of the problem is $u(\mathbf{x}, t, \omega)$. Weighted residual method is applied to get a solution with zero residual for the expanded form of the solution. The weight function is for this case the Lagrangian polynomial chaos multiplied with a desired output $f(\xi)$. The source term S is assumed to be not present. The weighted residual method makes use of the property of the variational principle to define the following equation

$$\int_{-\infty}^{\infty} D\left(\mathbf{x}, t, w; \sum_{i}^{N_p} u_i(\mathbf{x}, t) L_i(\boldsymbol{\xi}(w))\right) L_k(\boldsymbol{\xi}) f(\boldsymbol{\xi}) d\boldsymbol{\xi} = 0 \quad \forall\ k. \tag{4.4}$$

The power of the PC method lies in the fact that it uses Gauss quadrature to evaluate the last given integration. Gauss quadrature is a numerical integration technique which can integrate polynomials exactly up to $2n-1$ order where n is the number of points and it is defined as

$$\int_{a}^{b} w(x) f(x) dx \approx \sum_{i=1}^{n} w_i f(x_i), \tag{4.5}$$

where the function f is evaluated at the point x_i and the corresponding weight of x_i is w_i. Approximating the integration (4.4) with the Gauss quadrature yields the following summation

$$\sum_{l=1}^{N} w_l D\left(\boldsymbol{x}, t, \omega_l; \sum_{i}^{N_p} u_i(\boldsymbol{x}, t) L_i(\boldsymbol{\xi}_l)\right) L_k(\boldsymbol{\xi}_l) f(\boldsymbol{\xi}_l) = 0. \tag{4.6}$$

Incorporating the Kronecker delta property of the Lagrange basis polynomials yields

$$\sum_{l=1}^{N} w_l D\left(\boldsymbol{x}, t, \omega_l; \sum_{i}^{N_p} u_i(\boldsymbol{x}, t)\delta_{il}\right) \delta_{kl} f(\boldsymbol{\xi}_l) = 0. \tag{4.7}$$

Again making use of the Kronecker delta property results in

$$\sum_{l=1}^{N} w_l D\left(\boldsymbol{x}, t, \omega_l; u_l(\boldsymbol{x}, t)\right) \delta_{kl} f(\boldsymbol{\xi}_l) = 0. \tag{4.8}$$

Finally, the Kronecker delta shows that the last equation should be evaluated for k

$$w_k D\left(\boldsymbol{x}, t, \omega_k; u_k(\boldsymbol{x}, t)\right) f(\boldsymbol{\xi}_k) = 0. \tag{4.9}$$

For nontrivial solution the last equation can be zero only for $u(\boldsymbol{x}, t, \omega_k) = u_k(\boldsymbol{x}, t)$. Hence, the PC method results in decoupled realizations of $u_k(\boldsymbol{x}, t)$ at the Gauss quadrature points. The considered physical phenomenon in this thesis is solved in a steady state manner, therefore, equation (4.1) reduces to

$$u(\omega) \approx \sum_{i}^{N_p} u_i L_i(\boldsymbol{\xi}(\boldsymbol{w})). \tag{4.10}$$

The PC method results in decoupled set of equations which makes the method non-intrusive. Non-intrusiveness means that it is not necessary to adapt the code of any software for uncertainty quantification purposes, which simplifies the UQ analysis enormously. The derivation of the PC method illustrates that for UQ analysis any mathematical model should be evaluated at the points specified by the Gauss quadrature rule. The points and their corresponding weights depend on the distribution of a variable. These values can be determined with the Golub-Welsch algorithm which is explained in the references (G. J. A. Loeven, 2010; Witteveen, 2009). After the evaluation of any model at the specified points the desired response surface can be constructed with equation (4.10). The required number of collocation points N_p to approximate the response surface by order p is $N_p = (p+1)^d$ where d is the number of uncertain parameters. For multidimensional UQ analysis the tensor product is applied to the Gauss quadrature points of each uncertain parameter. The amount of computational work to perform the PC method is equal to N_p deterministic simulations. At high number of uncertain parameters the curse of dimensionality arises. Especially for computationally expensive problems like in the field of fluid dynamics the high dimensionality can make the PC analysis intractable. To reduce the dimensionality of a problem sensitivity analysis can be performed to discard any uncertain parameter that has less effect on the solution.

4.2 Separately propagated uncertain parameters

In this section, the effect of the uncertain parameters on the force coefficients C_l and C_d is investigated by one dimensional UQ analysis. This means that only one parameter is uncertain at each analysis. The uncertain parameters that are considered for UQ analysis are C_μ, $C_{\epsilon 1}$, $C_{\epsilon 2}$, σ_ϵ, σ_k, E and κ, detailed information about them is given in Table 2.3. These uncertain parameters belong to the standard $k-\epsilon$ model for wall-bounded flows. The physical phenomenon that is considered is the turbulent flow over the airfoil DU96-W-180. For each uncertain parameter a pdf is defined based on algebraic analysis, experimental results and/or expert opinions in Section 2.3. The pdf of each parameter is used to perform the UQ analysis with the PC method. The PC method is performed for the orders one to six. These analysis correspond with 27 deterministic simulations for each parameter, hence, in total 189 deterministic simulations are performed for 1-D UQ analysis. The conditions of the simulations are $\alpha = 1.45°$, $R = 2 \cdot 10^6$ and $M = 0.15$. From the results of these simulations the response curves are constructed for one to six orders of C_l and C_d. The relative error is determined for the orders one to five to confirm the exponential convergence of the simulations. For the sixth order the probability density function of C_l and C_d are determined. Also their statistical mean μ and standard deviation σ are calculated at the sixth order.

The relative error of the approximation is calculated by comparing the response curve of the order p with the response curve of the order $p+1$. The expression to determine the relative error for order p (Tatang, Pan, Pring, & McRae, 1997; G. J. A. Loeven, 2010) is

$$\varepsilon_p = \frac{\sqrt{\frac{1}{N_{p+1}} \sum_{i=1}^{N_{p+1}} w_i \left(C_{li}^{p+1} - \hat{C}_{li} \right)^2}}{\frac{1}{N_{p+1}} \sum_{i=1}^{N_{p+1}} \hat{C}_{li}} \tag{4.11}$$

where N_{p+1} is the number of collocation points for the order $p+1$, w_i are the Gauss quadrature weights, C_{li} represents the lift coefficient C_l and $\hat{C}_{li}$ denotes the values of C_l approximated by the response curve of order p at the collocation points of $p+1$ order. The relative error for C_d can be determined in the same way as for C_l by using the values of C_d in equation (4.11).

The response curves, the relative error and the pdf of C_l and C_d are presented in Figures 4.1 to 4.7 for the seven uncertain parameters.

Readily the statistical quantities mean μ and variance σ^2 can be obtained with the PC method by using the following formula

$$\mu = \sum_{i=1}^{N_p} u_i w_i, \tag{4.12}$$

$$\sigma^2 = \sum_{i=1}^{N_p} \left[(u_i - \mu)^2 \right] w_i. \tag{4.13}$$

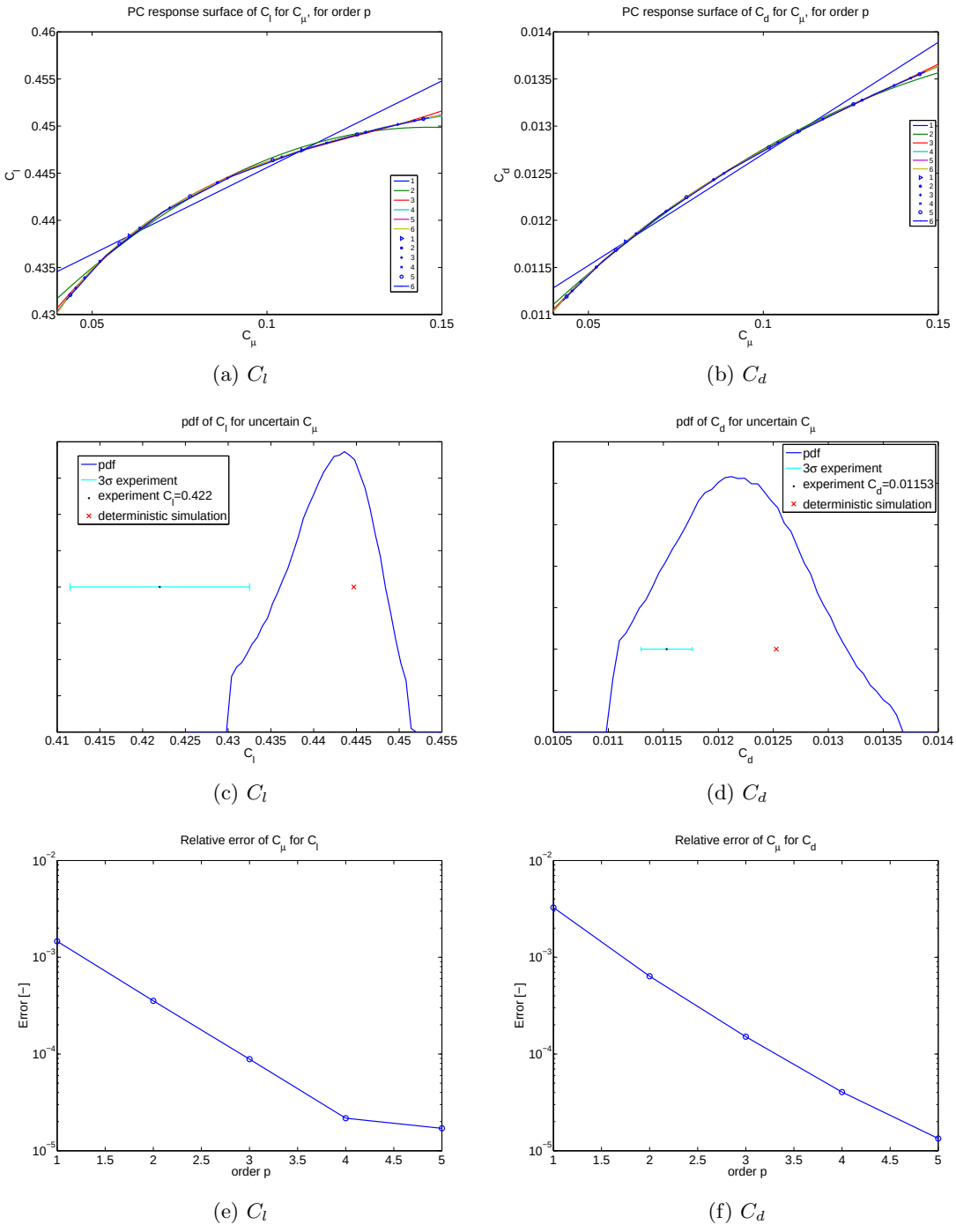

(a) C_l (b) C_d

(c) C_l (d) C_d

(e) C_l (f) C_d

Figure 4.1: UQ analysis with PC method for uncertain C_μ. The response curves, relative error, pdf, experimental data with its uncertainty and deterministic simulation of C_l and C_d are presented.

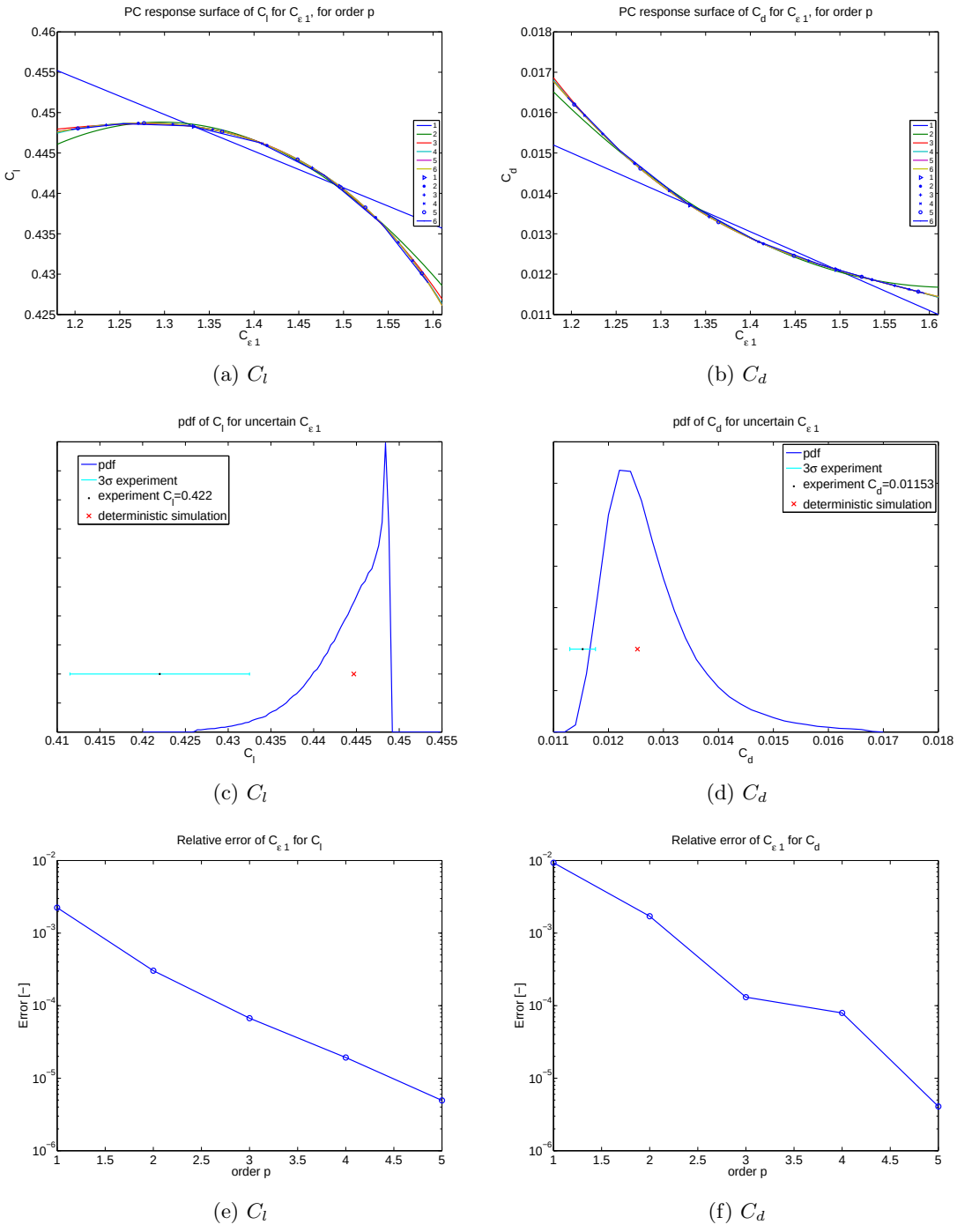

(a) C_l (b) C_d

(c) C_l (d) C_d

(e) C_l (f) C_d

Figure 4.2: UQ analysis with PC method for uncertain $C_{\epsilon 1}$. The response curves, relative error, pdf, experimental data with its uncertainty and deterministic simulation of C_l and C_d are presented.

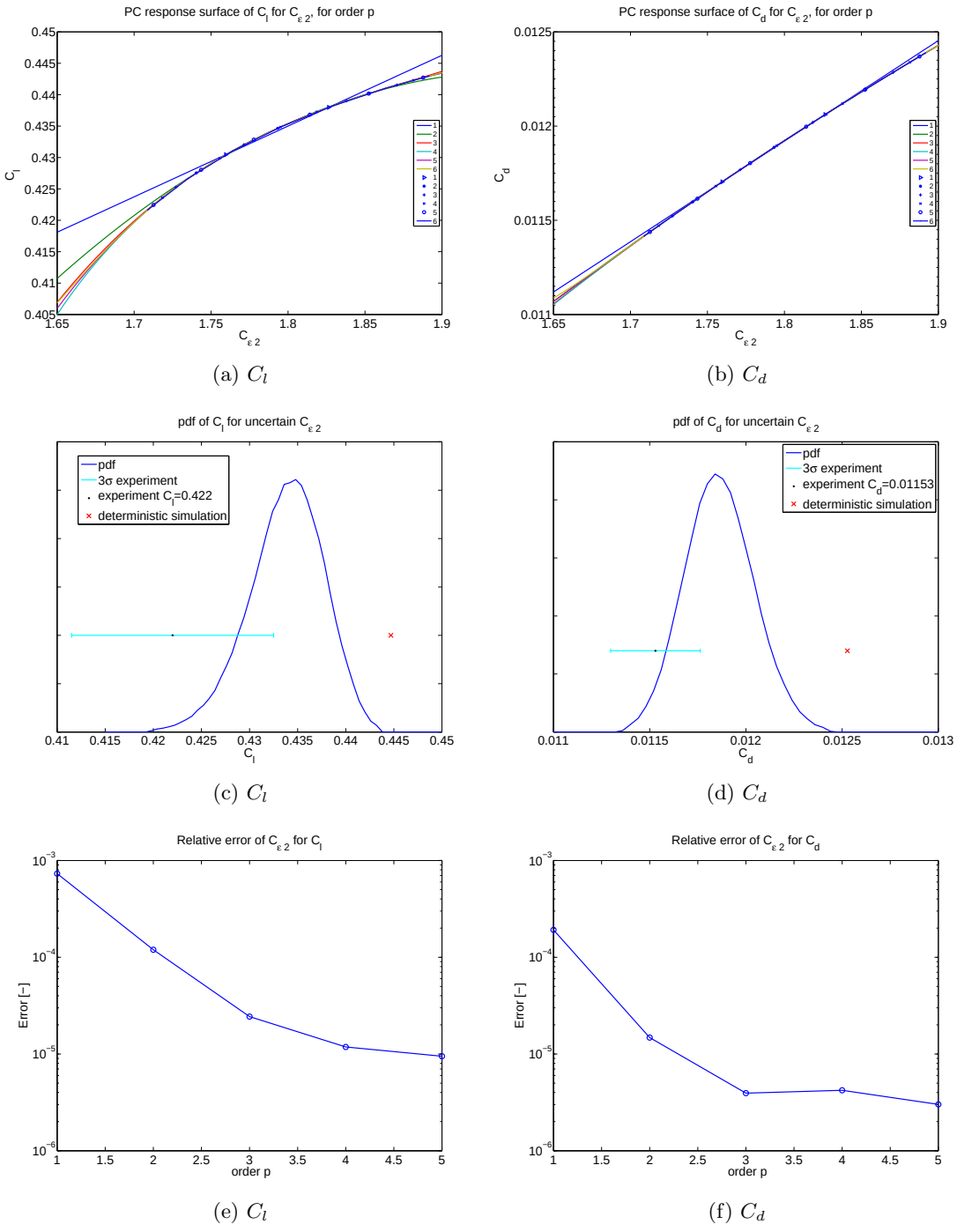

(a) C_l (b) C_d

(c) C_l (d) C_d

(e) C_l (f) C_d

Figure 4.3: UQ analysis with PC method for uncertain $C_{\epsilon 2}$. The response curves, relative error, pdf, experimental data with its uncertainty and deterministic simulation of C_l and C_d are presented.

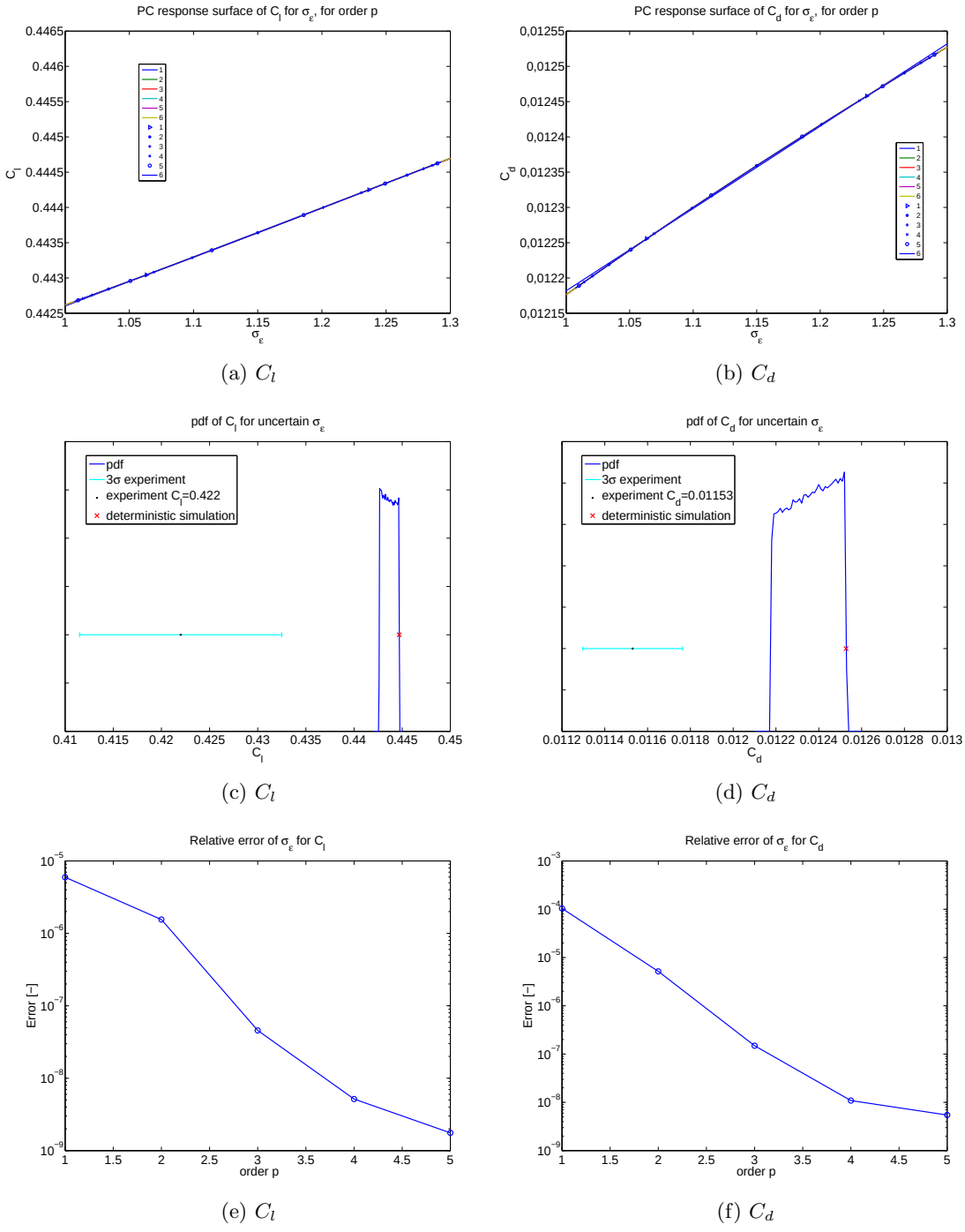

(a) C_l (b) C_d

(c) C_l (d) C_d

(e) C_l (f) C_d

Figure 4.4: UQ analysis with PC method for uncertain σ_ϵ. The response curves, relative error, pdf, experimental data with its uncertainty and deterministic simulation of C_l and C_d are presented.

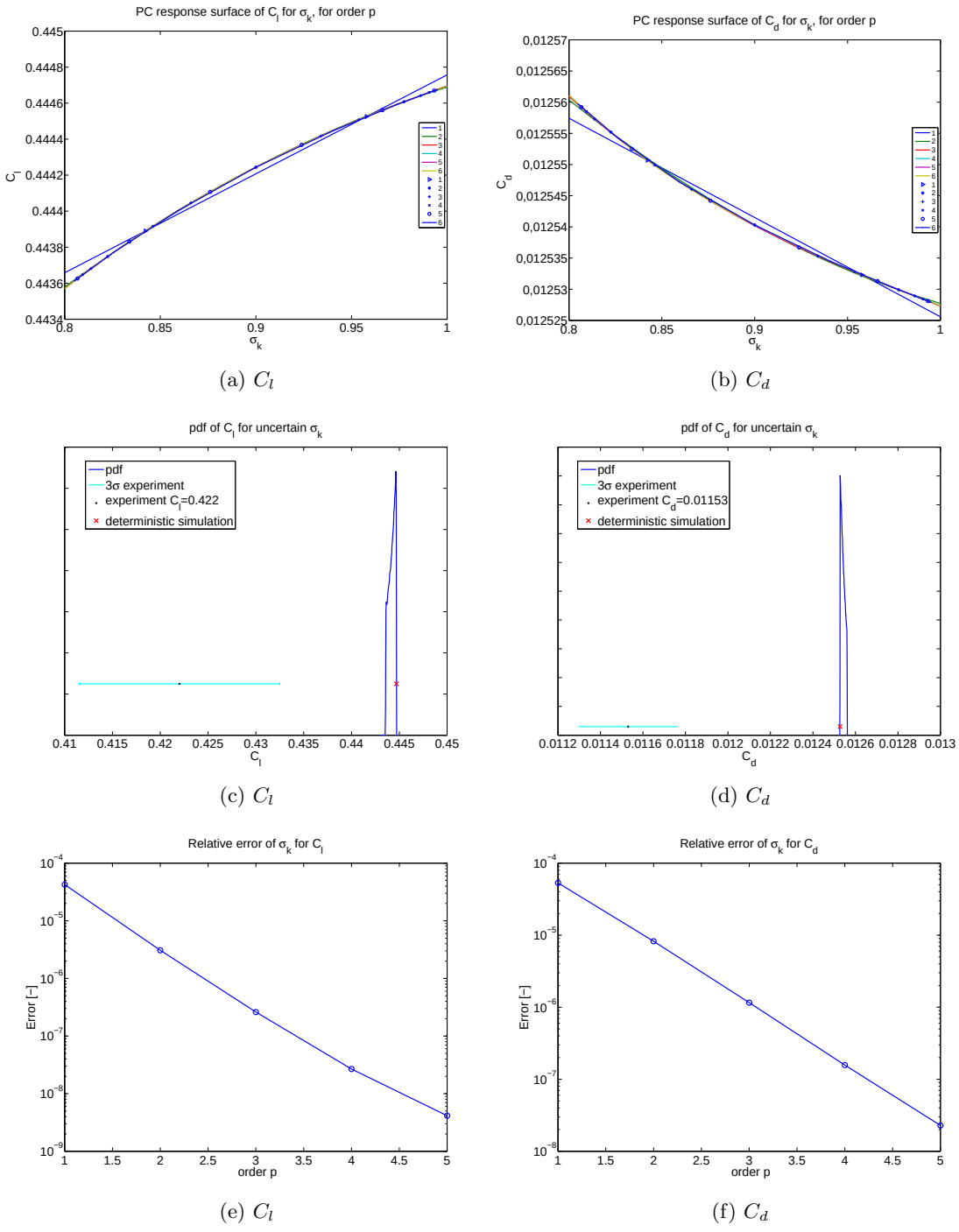

(a) C_l (b) C_d

(c) C_l (d) C_d

(e) C_l (f) C_d

Figure 4.5: UQ analysis with PC method for uncertain σ_k. The response curves, relative error, pdf, experimental data with its uncertainty and deterministic simulation of C_l and C_d are presented.

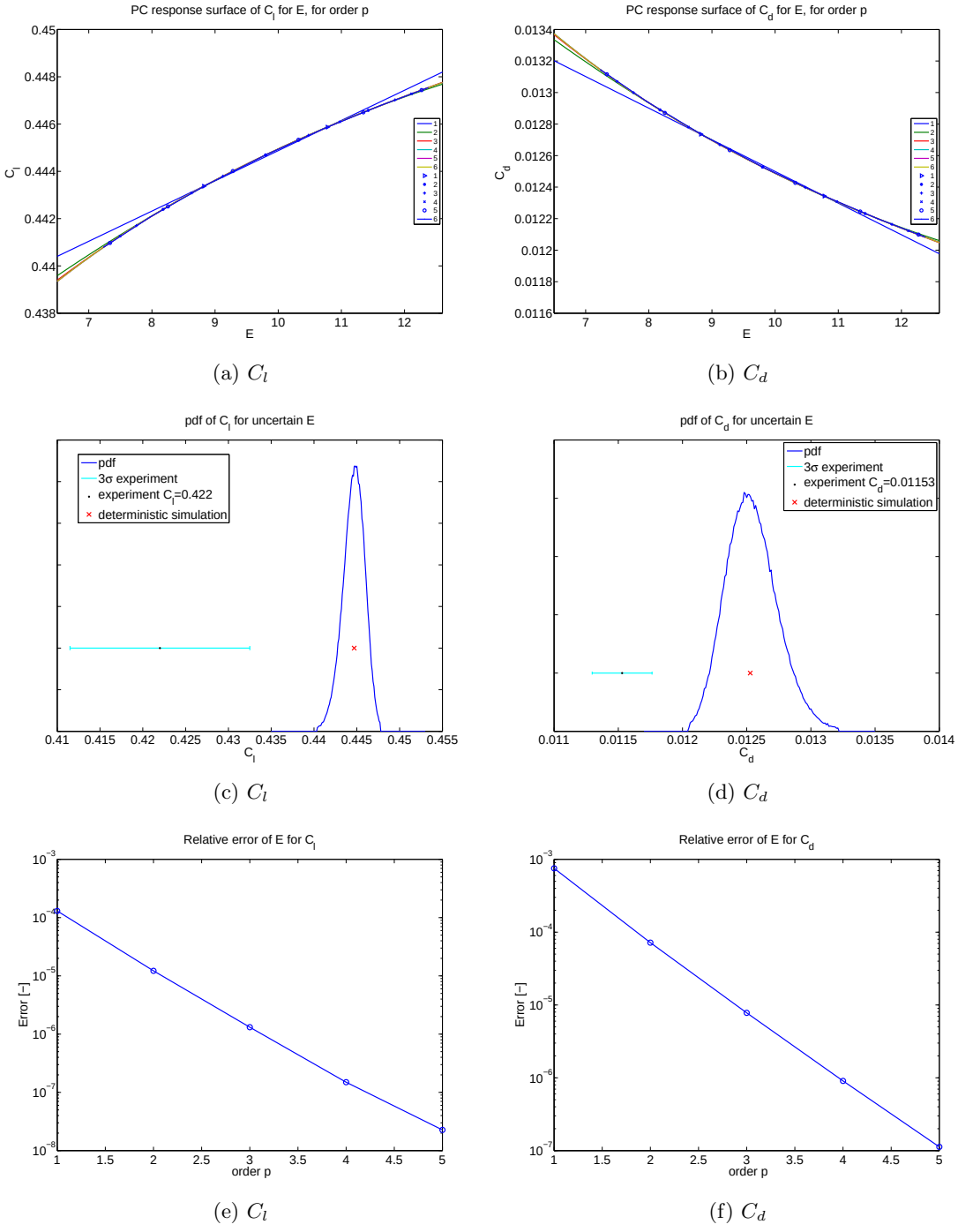

(a) C_l (b) C_d

(c) C_l (d) C_d

(e) C_l (f) C_d

Figure 4.6: UQ analysis with PC method for uncertain E. The response curves, relative error, pdf, experimental data with its uncertainty and deterministic simulation of C_l and C_d are presented.

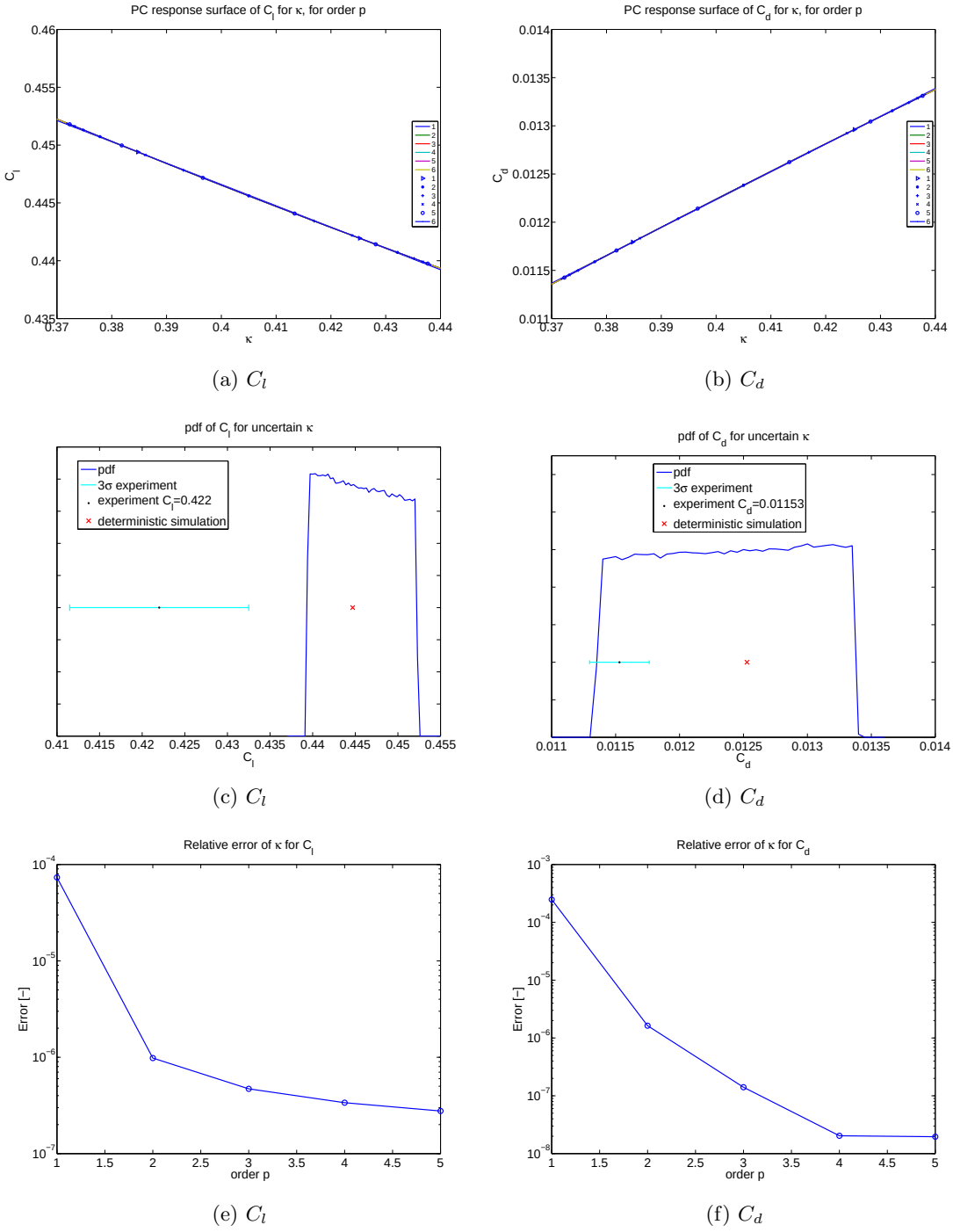

(a) C_l (b) C_d

(c) C_l (d) C_d

(e) C_l (f) C_d

Figure 4.7: UQ analysis with PC method for uncertain κ. The response curves, relative error, pdf, experimental data with its uncertainty and deterministic simulation of C_l and C_d are presented.

The standard deviation σ is the square root of the variance. The mean and the standard deviation of the pdf's for the uncertain parameters are determined at the sixth order approximation and tabulated in Table 4.1. The coefficient of variation CV

$$CV = \frac{\sigma}{\mu} \tag{4.14}$$

for each parameter is calculated to have a dimensionless quantity about the dispersion of the C_l and C_d, see Table 4.2.

Observations from the results

The relative errors are decreasing for increasing order for all the response curves of the uncertain parameters. Only for the response curve of C_d for uncertain $C_\epsilon 2$ a small increase is observed in the relative error for the fourth order. The main observation is that the drag coefficient is more sensitive to the applied uncertainty than the lift coefficient. For C_d the most influential parameters are C_μ, $C_{\epsilon 1}$ and κ. The parameter C_μ is proportional to the eddy viscosity ν_t, $C_{\epsilon 1}$ is present in the production term of ϵ and κ is present in the wall function. The most influential parameters for C_l are C_μ, $C_{\epsilon 1}$, $C_{\epsilon 2}$ and κ. The parameter σ_k has almost negligible effect on the force coefficients. The discretization error, which is 0.5438 % for C_l and -0.8899 % for C_d can be compared with $6 \cdot CV$ to notice the importance of UQ analysis, note that $6 \cdot CV$ captures 99.7 % of the distribution. The discretization error is 8.3 % and 1.74 % respectively for C_l and C_d of the range of the pdf's of C_μ C_l and $C_{\epsilon 1}$ C_d.

Parameter	C_l		C_d	
	μ	σ	μ	σ
C_μ	0.4415430570	0.0048409934	0.0121882539	0.0005827331
$C_{\epsilon 1}$	0.4439190276	0.0043111502	0.0127764787	0.0008526840
$C_{\epsilon 2}$	0.4337857816	0.0038759657	0.0118629137	0.0001776686
σ_k	0.4442072196	0.0003220107	0.0125415285	0.0000094980
σ_ϵ	0.4436463584	0.0006019471	0.0123567540	0.0001012472
κ	0.4456758321	0.0037309947	0.0123774769	0.0005839866
E	0.4446196874	0.0012640659	0.0125396060	0.0001987166

Table 4.1: The mean and the standard deviation of C_l and C_d for the uncertain parameters, determined at sixth order of approximation.

4.3 Simultaneously propagated three uncertain parameters

In previous section UQ analysis is performed by propagating the uncertainty separately for the seven uncertain parameters. In this section based on the results of 1-D UQ analysis three uncertain parameters are selected from the core $k - \epsilon$ model parameters to perform simultaneously UQ analysis. Therefore, the most influential parameters on the force coefficients C_μ, $C_{\epsilon 1}$ and $C_{\epsilon 2}$ are chosen from the five core $k - \epsilon$ model parameters.

Parameter	CV [%]	
	C_l	C_d
C_μ	1.0963808146	4.7811044567
$C_{\epsilon 1}$	0.9711568748	6.6738577615
$C_{\epsilon 2}$	0.8935206872	1.4976812885
σ_k	0.0724910975	0.0757321116
σ_ϵ	0.1356817346	0.8193673895
κ	0.8371543721	4.7181390824
E	0.2843027326	1.5847118057

Table 4.2: Coefficient of variation of the distributions of C_l and C_d for the seven uncertain parameters.

The discarded parameters σ_ϵ and σ_k have the least influence on the force coefficients from the seven uncertain parameters. In this way the combined effect on the solution is investigated. The three-dimensional (3-D) UQ analysis is performed for the orders one to four. This requires respectively $8 + 27 + 64 + 125 = 224$ deterministic simulations. There is one simulation not converged among the third order simulations and there are three simulations not converged among the fourth order simulations. Especially that is the case for low value of C_μ combined with a low difference between $C_{\epsilon 2}$ and $C_{\epsilon 1}$. Still to have reasonable outputs for the not converged simulations they are predicted with the kriging method. Kriging uses the available data to predict the value at the unobserved location. Therefore is the Matlab toolbox DACE (IMM-TR-2002-12, 2002) used.

The relative error and the standard deviation for orders one to three are depicted in Figure 4.8. The decrease of the relative error for increasing order for C_l is lower than the decrease in relative errors for C_μ, $C_{\epsilon 1}$ and $C_{\epsilon 2}$ for 1-D UQ. It is important that the relative error is negligible compared to the standard deviation of the distribution to have negligible effects of the approximation error on the solution. A factor of ten between the standard deviation and the relative error is acceptable. If only the standard deviation is considered to decide which order is acceptable for further analyses then for C_l the second order and for C_d the third order are acceptable.

The probability density function of C_l and C_d are determined at the fourth order approximation. The pdf of the force coefficients, the experimental value with its uncertainty and the outcome of the deterministic simulation are illustrated in Figure 4.9. The uncertainty in the experimental value is shown with the three-sigma rule which incorporates 99.7 % of the possible experimental measurement. Note that the deterministic simulation indicates the numerical simulation with the standard values of the model parameters. The pdf of C_l has a very long left tail, however, the probability that $C_l < 0.3$ is very small. The distribution of the experimental data is inside the stochastic response. The standard deviation of the experimental data is 18.5 % and 8.3 % respectively of the standard deviations of C_l and C_d. The coefficients of variation are calculated from the fourth polynomial order. These are for C_l 4.43 % and for C_d 8.01 %. The combined effect of the three uncertain parameters on the C_l as well as on the C_d is much larger than the CV for separately propagated uncertainties. The statistics of the pdf for the force coefficients as a result of three-dimensional UQ analysis are summarized in Table 4.3 for the fourth order of

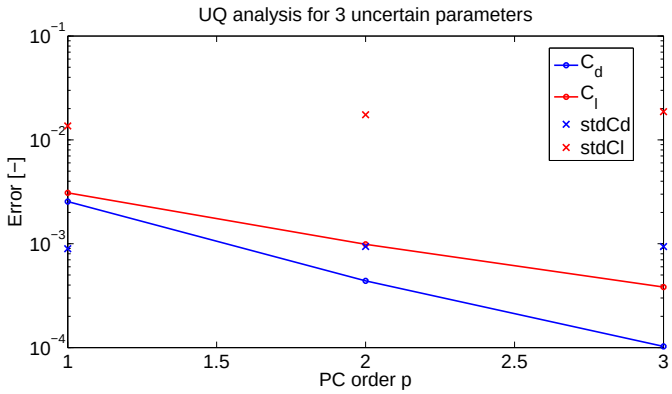

Figure 4.8: The relative errors and standard deviations for one to three orders of C_l and C_d.

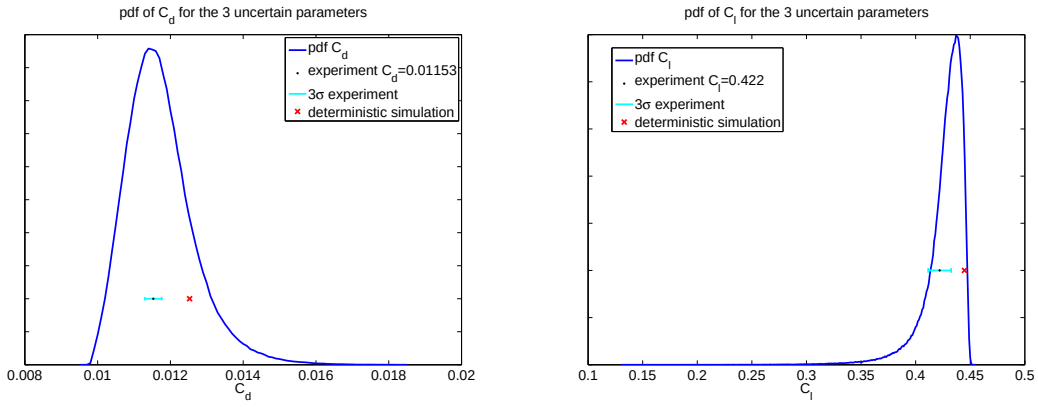

(a) C_d (b) C_l

Figure 4.9: The pdf of (a) C_d and (b) C_l as a result of 3-D UQ analysis with the uncertain parameters $C_{\epsilon 1}$, $C_{\epsilon 2}$ and C_μ, obtained at the fourth order. The experimental data with the three-sigma rule and the outcome from the deterministic simulation are shown as well.

approximation.

The response surfaces from the fourth order approximation are plotted in Figure 4.10 for C_d and C_l by reducing the variables to two by keeping C_μ constant at each figure. There are five collocation points for the fourth polynomial order that is the reason of the five subfigures. The large variation in C_l is located in a small area in the $C_{\epsilon 1}$ and $C_{\epsilon 2}$ plane.

4.4 Simultaneously propagated five uncertain parameters

Because of the curse of dimensionality the final UQ analysis is performed by propagating the uncertainty simultaneously only in five parameters. Therefore, two uncertain parameters which have small effect on the solution are discarded from the UQ analysis. The most influential five parameters are determined based on the coefficient of variation from the 1-D UQ analysis, see Table 4.2. Hence, the most influential five uncertain parameters

	μ	σ	CV [%]
C_d	0.011723791	0.000938852	8.008
C_l	0.426325374	0.018868536	4.426

Table 4.3: Statistics of the pdf from 3-D UQ analysis for the fourth polynomial order.

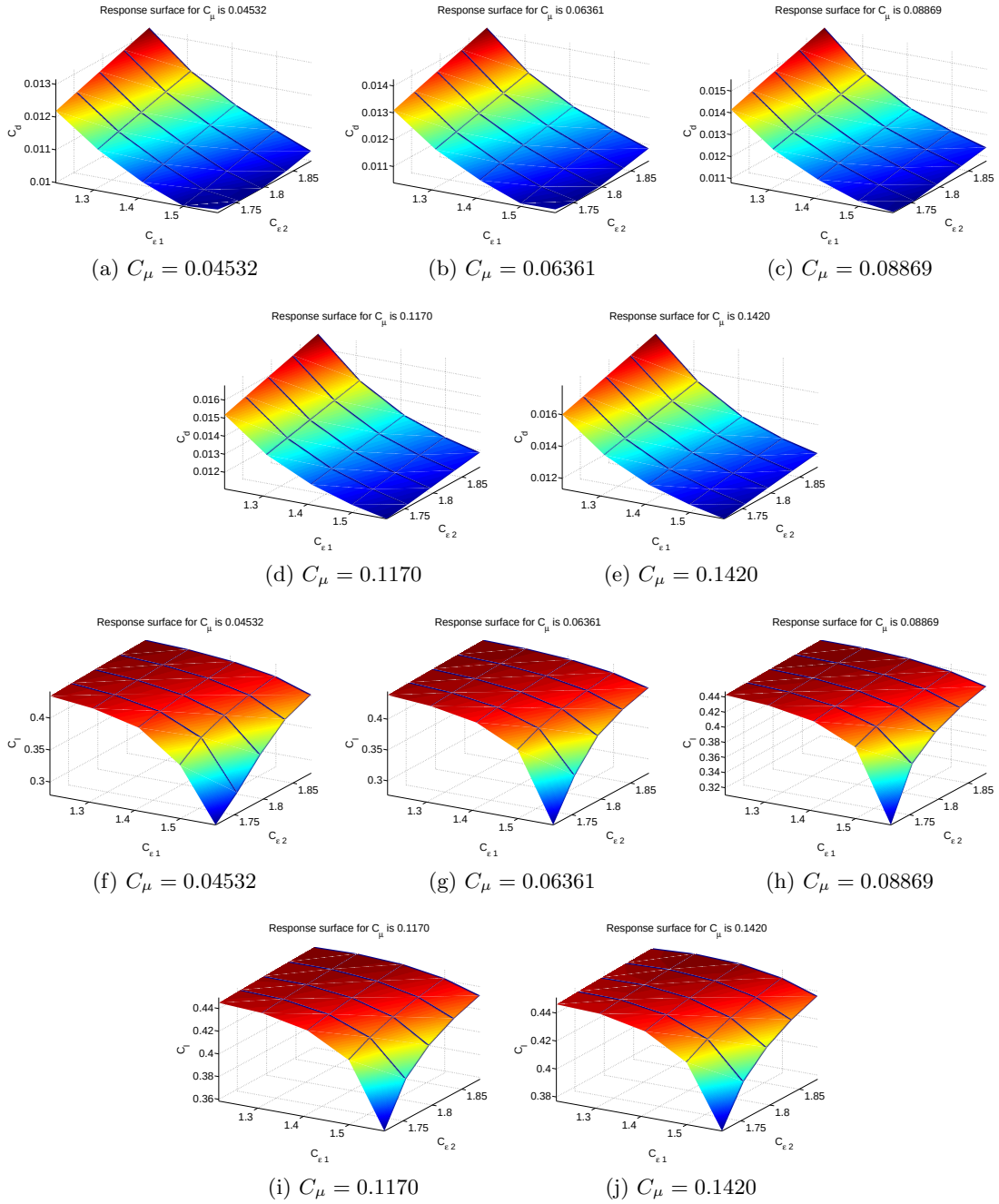

(a) $C_\mu = 0.04532$ (b) $C_\mu = 0.06361$ (c) $C_\mu = 0.08869$

(d) $C_\mu = 0.1170$ (e) $C_\mu = 0.1420$

(f) $C_\mu = 0.04532$ (g) $C_\mu = 0.06361$ (h) $C_\mu = 0.08869$

(i) $C_\mu = 0.1170$ (j) $C_\mu = 0.1420$

Figure 4.10: The response surfaces of C_d and C_l from 3-D PC analysis obtained at the fourth order, in each subfigure C_μ is constant.

	μ	σ	CV [%]
	$\alpha = 1.45°$		
C_d	0.011600718	0.001079582	9.306
C_l	0.427247309	0.020524388	4.804
	$\alpha = 4.54°$		
C_d	0.014354805	0.001464606	10.20
C_l	0.744055135	0.043421038	5.84
	$\alpha = 7.61°$		
C_d	0.020304288	0.002629112	12.95
C_l	1.005712914	0.100426089	9.99

Table 4.4: The statistics of the pdf's from 5-D UQ analysis for AoA of $1.45°$, $4.54°$ and $7.61°$.

on the force coefficients are C_μ, $C_{\epsilon 1}$, $C_{\epsilon 2}$, E and κ. The order of the approximation of the response surfaces are based on the previous results of UQ analysis and the available computational resource. The curse of the dimensionality plays a huge role at this stage, therefore, low orders of approximation are preferred.

Third order approximation is chosen for the two most influential parameters on the force coefficients C_μ and $C_{\epsilon 1}$. For the other three parameters $C_{\epsilon 2}$, E and κ second order approximation is employed. For these order of approximations the total number of deterministic simulations required to propagate the uncertainty simultaneously with the PC method is 432. The five dimensional UQ analysis is performed for three different angles of attack namely 1.45°, 4.54° and 7.61°. The range with separation is avoided. As a result of this analysis the pdf of C_l and C_d are presented for the AoA 1.45°, 4.54° and 7.61° in Figure 4.11. The mean, standard deviation and the coefficient of variation of these pdf's are given in Table 4.4.

There are 5, 18 and 51 simulations not converged from the numerical simulations respectively at AoA of 1.45°, 4.54° and 7.61°. The outputs of these simulations are predicted with the kriging method. This introduces uncertainty in the response surfaces, however, the introduced uncertainty is mainly located in the tails of the pdf's. The discretization error is 11.8 % and 10.7 % of the standard deviation of the pdf for $\alpha = 1.45°$ respectively for C_l and C_d. This illustrates the negligible effect of the discretization error compared to the effects of the uncertainty. The CV of the pdf's for 5-D UQ are larger than for 3-D UQ analysis at $\alpha = 1.45°$. For increasing AoA an increase in the CV is observed for both the force coefficients.

4.5 Convergence problems

Some of the simulations for the UQ analysis did not converge. The reason therefore is that the changed model parameters are not able to simulate the flow accurately. Especially, the simulations do not converge for low value of C_μ combined with a low difference between $C_{\epsilon 2}$ and $C_{\epsilon 1}$. Actually, from the results appeared that the model creates separation at

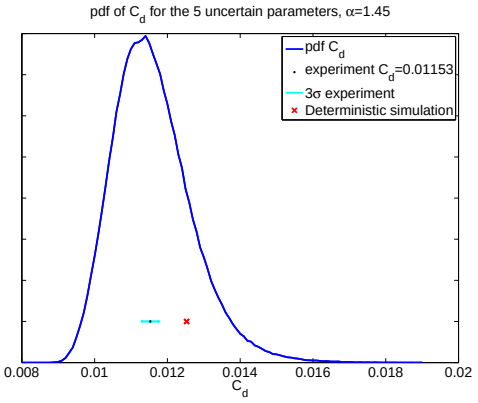

(a) C_d

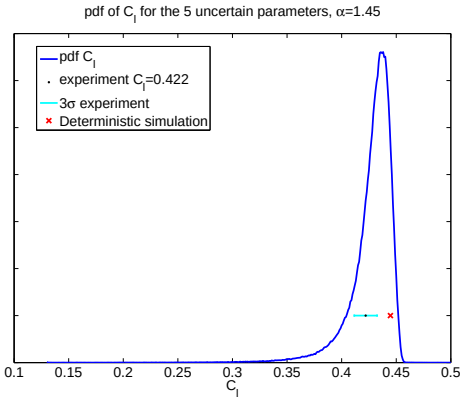

(b) C_l

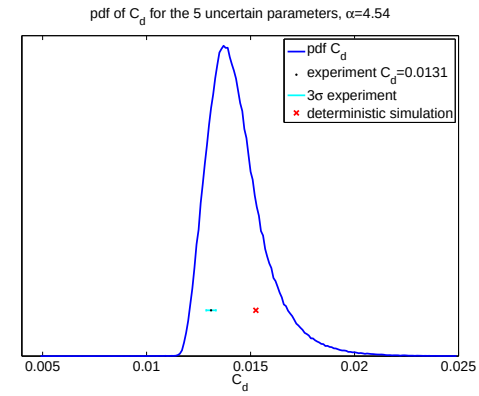

(c) C_d

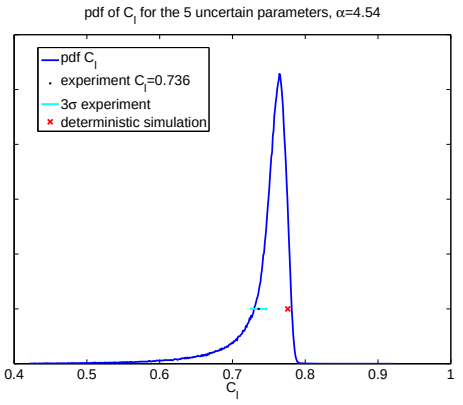

(d) C_l

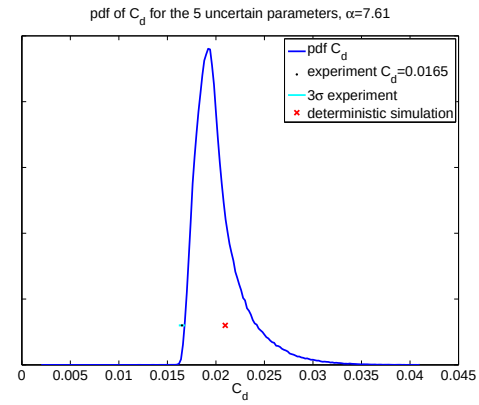

(e) C_d

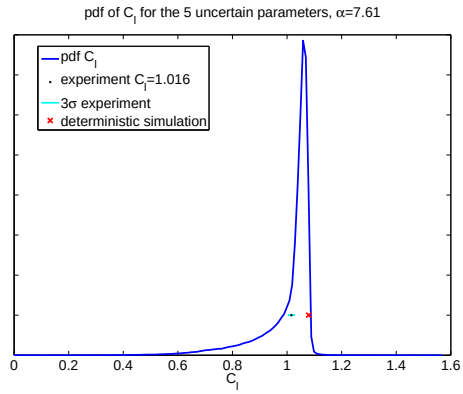

(f) C_l

Figure 4.11: The pdf of the response surface of C_d and C_l as a result of 5-D UQ analysis with the uncertain parameters $C_{\epsilon 1}$, $C_{\epsilon 2}$, C_μ, κ and E for the AoA of 1.45°, 4.54° and 7.61°. The experimental data and its 3σ and deterministic simulation result are depicted as well.

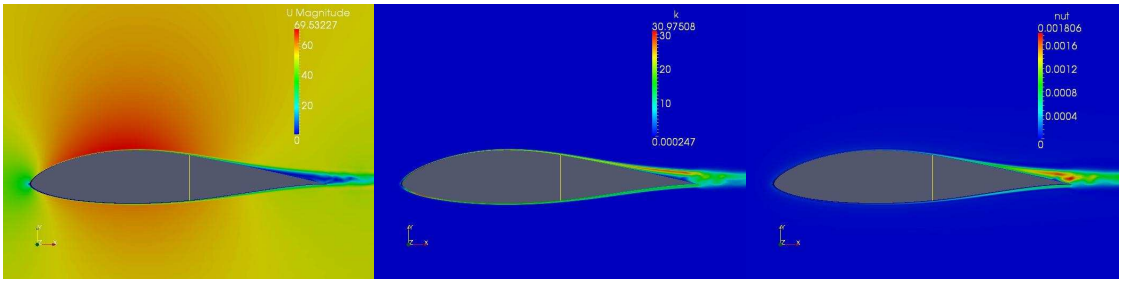

(a) u (b) k (c) ν_t

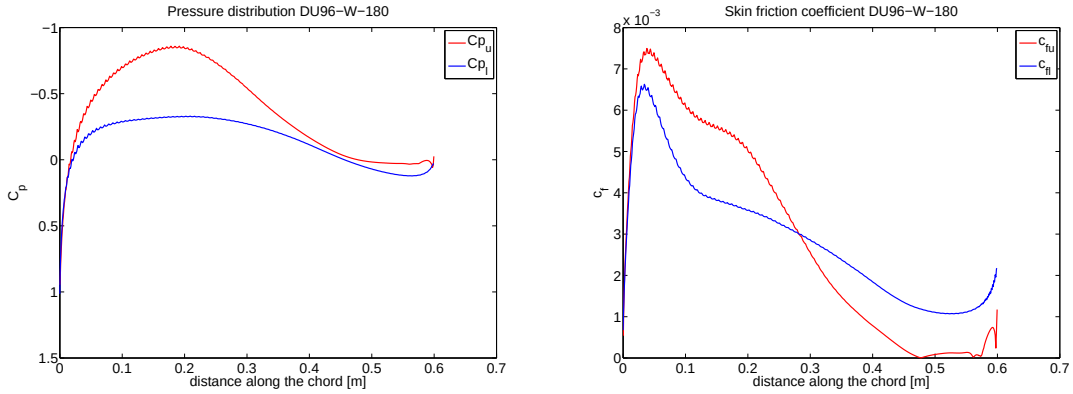

(d) C_p (e) c_f

Figure 4.12: One example of not converged simulation with (a) u, (b) k, (c) ν_t, (d) C_p and (e) c_f.

the trailing edge on the upper surface. To show this behaviour results from one of the not converged simulations are illustrated in Figure 4.12.

Chapter 5

Bayesian Calibration

The second main objective of this thesis is to calibrate the standard $k-\epsilon$ model parameters to the experimental data of the turbulent flow over the airfoil DU96-W-180. The calibration is performed for the parameters C_μ, $C_{\epsilon 1}$, $C_{\epsilon 2}$, κ and E. The parameters σ_ϵ and σ_k were discarded because of their negligible influence on the force coefficients. The calibration is performed with the Bayesian Inference/Calibration method in combination with the Markov Chain Monte Carlo (MCMC) method. These are explained respectively in Sections 5.1 and 5.2. The standard $k-\epsilon$ model is evaluated with the surrogate models that are built in Section 4.4 for AoA 1.45°, 4.54° and 7.61°. In Section 5.3 the Bayesian inference is applied for the AoA 1.45°, 4.54° and 7.61° by using two experimental data of the corresponding α. Hereafter, the model parameters are calibrated by using the maximum available data which is six. However, because the model could not be calibrated accurately for this case two other calibrations are performed by employing four and five experimental data. These calibrations can be found in Section 5.4. Subsequently, the calibrated sets presented in Section 5.4 are used to simulate the considered phenomenon. The results of these simulations are presented and discussed in Section 5.5.

5.1 Bayesian Inference

The civilisation of today is based on learning new facts which eventually helps each person in making wise decisions. The way each person acts is in this way influenced positively by gathering new information. Besides that, one's decision is constantly influenced by new learned information. For instance, going on holiday may depend on the new gathered information about the weather conditions. Frequently, new information is in this way used to update an old decision. A similar thought can also be conducted in mathematics. Usually, a mathematical model of a physical system is developed to predict the desired outputs, also called the quantities of interest like the force coefficients. Running the model for the same inputs will produce the same values as output. The method of prediction of the desired outputs in this way is called the forward modelling. If the model does not meet the expectations the model can be partially changed by adding/removing extra terms or

completely changed by developing a new mathematical model. A third way between these options is to adapt the model parameters by using the measurements of the observable parameters. Making use of the measurements of the observable parameters to improve the existing model of a physical system is called the inverse modelling.

The framework used for calibration in this chapter is called the Bayesian inference which is based on the Bayes' rule ((Montgomery & Runger, 1994)), named after the English mathematician Thomas Bayes. The Bayes' rule is derived from the conditional probability. The conditional probability of the events A and B is

$$P(A|B) = \frac{P(A \cap B)}{P(B)}, \tag{5.1}$$

where $P(B)$ is the probability of the event B. The probability $P(A|B)$ indicates the conditional probability of the event A given that the event B has occurred. $P(A \cap B)$ represents the intersection probability of the events A and B. In the same manner the probability $P(B|A)$ can be calculated

$$P(B|A) = \frac{P(A \cap B)}{P(A)}, \tag{5.2}$$

where $P(A)$ is the probability of the event A. Because the probability of the intersection of two events is the same irrespective of the order the following relation is obtained

$$P(A|B)P(B) = P(B|A)P(A). \tag{5.3}$$

The probability $P(A|B)$ can then be calculated as

$$P(A|B) = \frac{P(B|A)P(A)}{P(B)}, \tag{5.4}$$

which is called the Bayes' rule/theorem. Bayes' theorem can be used to calibrate a model to experimental data. This methodology is called the Bayesian calibration/inference. In the calibration process the probability $P(B)$ is often to difficult to calculate and because it acts only as a normalizing term independent of A it is left out from the relation. Introducing the model parameter vector $\boldsymbol{\theta}$ and the vector containing the observable parameters data $\mathbf{d}$ Bayesian inference becomes

$$P(\boldsymbol{\theta}|\mathbf{d}) \propto P(\mathbf{d}|\theta)P(\boldsymbol{\theta}). \tag{5.5}$$

$P(\mathbf{d}|\boldsymbol{\theta})$ is denoted as the *likelihood* which is the probability that the model will predict the data $\boldsymbol{d}$ given the parameters $\boldsymbol{\theta}$. In this context $P(\boldsymbol{\theta})$ is called the *prior*. The prior is the uncertainty in the model parameters before the observations. For instance, in a mass force relation model the distribution of the measurements of mass can be used as the prior. $P(\boldsymbol{\theta}|\mathbf{d})$ denotes the posterior probability of $\boldsymbol{\theta}$ given the data $\mathbf{d}$.

5.1.1 Bayesian calibration of the $k-\epsilon$ model parameters

In this thesis the inverse modelling is applied to fit the experimental data of force coefficients to the force coefficients as outputs of the simulated turbulent flow over the airfoil DU96-W-180. The mathematical model consists of the RANS equations with the standard $k-\epsilon$ model.

The statistical model that is considered for the Bayesian calibration is

$$\mathbf{d} = m(\boldsymbol{\theta}) + e, \tag{5.6}$$

where $m(\boldsymbol{\theta})$ denotes the model to calculate the quantities of interest with the model parameters $\boldsymbol{\theta}$, e is the observational uncertainty of the observable parameters and $\boldsymbol{d}$ denotes the observable parameters. The observable parameters and the quantities of interest of the model $m(\boldsymbol{\theta})$ are the force coefficients C_l and C_d in this thesis. The measurement error is assumed to be normal distributed with mean zero and the standard deviation is determined from the measurements of C_l and C_d in Section 3.5. The employed model (5.6) indicates that an observable parameter can be obtained from the mathematical model plus the experimental uncertainty. So, the model is assumed to have no model inadequacy.

The quantities of interest from the standard $k-\epsilon$ model are obtained by using surrogate models. The surrogate models of C_l and C_d are built in Section 4.4 for the angles of attack 1.45°, 4.54° and 7.61° for the five most influential uncertain parameters on the force coefficients. These are C_μ, $C_{\epsilon 1}$, $C_{\epsilon 2}$, E and κ. For the mentioned AoA there are in total six experimental data and six surrogate models available. The priors of the parameters are determined in Section 2.3.

The likelihood term in formula (5.5) is not explicitly defined. The statistical model (5.6) is used to define the likelihood in the following manner with p denoting the probability density function

$$p(\mathbf{d}|\boldsymbol{\theta}) = p(e) = p(\boldsymbol{d} - m(\boldsymbol{\theta})) \propto \exp\left\{-\frac{(\mathbf{d} - m(\boldsymbol{\theta}))^2}{2\sigma^2}\right\}, \tag{5.7}$$

where the σ denotes the standard deviation of the experimental error, note that the experimental uncertainty in equation (5.5) is known. For multiple data n the likelihood term takes the following form

$$\prod_{i=1}^{n} \exp\left\{-\frac{(d_i - m_i(\boldsymbol{\theta}))^2}{2\sigma_i^2}\right\}. \tag{5.8}$$

The data used for the calibration consist of the force coefficients C_l and C_d. The Bayesian calibration in terms of the force coefficients can be formulated as

$$p\left(\boldsymbol{\theta}|d_{C_{l,i}}, d_{C_{d,j}}\right) \propto L_i\left(d_{C_{l,i}}|\boldsymbol{\theta}\right) L_j\left(d_{C_{d,j}}|\boldsymbol{\theta}\right) p\left(\boldsymbol{\theta}\right) \tag{5.9}$$

where L is the likelihood term, i and j denote the number of data used in the calibration process. First, the model parameters are calibrated for the three mentioned AoA separately, by using the force coefficients at that α. Hereafter, the model parameters are calibrated by using more than two experimental data by combining the data at the three AoA. The set of parameters that maximizes the $p(\mathbf{d}|\boldsymbol{\theta})$ is determined for each calibration.

The posterior distribution of the parameters can be obtained by applying the Bayesian inference (5.5) in combination with Markov Chain Monte Carlo method which is the subject of the next section.

5.2 Markov Chain Monte Carlo

The calibrated posterior distributions of the model parameters can be numerically obtained with Markov Chain Monte Carlo method (MCMC). MCMC is a Monte Carlo based method with a special sampling technique that has the Markov property. Essentially, Markov property means that the next generated number for a variable is only dependent on the current value of that variable. The next value of a parameter is generated from a distribution called the proposal distribution. In that way generated sequence of numbers is called Markov Chain. The generated sequence of numbers for sampling from the posterior distribution in this thesis is based on the Metropolis Sampler (N. Metropolis, Rosenbluth, Rosenbluth, Teller, & Teller, 1953). The procedure of the Metropolis Sampler, which consists of five steps, is explained for one variable as follow:

1. Initialize a value X_t for the variable and start with t = 1.
2. Based on the previous value of the variable generate a candidate point C from a proposal distribution.
3. Evaluate the current value and the candidate point C of the variable with the Bayesian inference formula 5.5. Subsequently calculate a measure for the correctness of the value C with respect to the current value with $\alpha(X_t, C) = min\left\{1, \frac{\pi(C)}{\pi(X_t)}\right\}$, where π represents the evaluation of the Bayesian inference.
4. Generate a value U from a uniform distribution $U(0, 1)$. Compare α and U: if $U \leq \alpha$ accept the candidate point C and set $X_{t+1} = C$ else reject the candidate point and set $X_{t+1} = X_t$.
5. Set t = t + 1 to go to the next step in the Markov chain and repeat steps 2 to 5 until a sufficient t steps have been done.

Metropolis sampler examines the proposal and makes sure that it can be part of the posterior distribution only if it meets the Bayesian inference check. The proposal function to generate a candidate C is assumed to be normal distributed with the mean X_t and an appropriate standard deviation. Because there are more than one model parameters present the same procedure is applied in the same loop to each model parameter θ and each parameter has its own proposal function. The first steps in the chain are discarded

for obtaining the posterior distributions. Because in begin the method is searching the right path. The discarded amount of steps is called the burn-in period, which is specific to each problem. The used burn-in period in this thesis has at least four digits. More information about the MCMC method and the sampling technique can be found in the lecture notes of (Walsh, 2004).

5.3 Calibration by using two experimental at a specific AoA

The calibrations are performed separately for the AoA 1.45°, 4.54° and 7.61° by using one experimental data of C_d and one experimental data of C_l. The posterior and the prior pdf's of the force coefficients for the mentioned AoA are presented in Figure 5.1. The standard $k-\epsilon$ model is correctly calibrated to the employed experimental data. The posterior distributions of each uncertain parameter and the two dimensional marginal distributions are shown in Figures 5.2, 5.3 and 5.4 respectively for AoA 1.45°, 4.54° and 7.61°. At α is 1.45° and 4.54° the posteriors of the uncertain parameters are not well informed by the calibration. They have generally normal distributions with large standard deviations. At $\alpha = 7.61°$ especially κ and C_μ are well informed by the calibration. The dependency between the marginal distributions of some of the parameters can be observed, for instance C_μ and $C_{\epsilon 1}$ are dependant on each other. The set of the model parameters that maximizes the $p(\mathbf{d}|\boldsymbol{\theta})$ for three AoA are given in Table 5.1.

	$\alpha = 1.45°$	$\alpha = 4.54°$	$\alpha = 7.61°$
C_μ	0.064838581232235	0.062843326004833	0.045569293680172
$C_{\epsilon 1}$	1.446778176122390	1.474144640778667	1.450359562897191
$C_{\epsilon 2}$	1.784840284059740	1.780602820025083	1.789552703990991
E	9.707624032319995	9.719702135853517	10.250712875283829
κ	0.423731263070804	0.397253048073403	0.370117542537733
C_l	0.422391308595715	0.736106520933257	1.015428752370740
C_d	0.011545899252120	0.013089049538845	0.016503410620547

Table 5.1: The set of parameters that maximizes the $p(\mathbf{d}|\boldsymbol{\theta})$ and the corresponding C_l and C_d for three AoA.

5.4 Combined calibrations at AoA 1.45°, 4.54° and 7.61°

The previous calibrations illustrated that the calibration process works well for one angle of attack with the experimental data of C_l and C_d. However, the main objective is to obtain one set of parameters that can predict the experimental data at different AoA. Therefore, the available six surrogate models and six experimental data for the AoA 1.45°, 4.54° and 7.61° are employed to calibrate the model parameters. Hereafter, the calibration is performed by employing four and five experimental data. The reason therefore will be clear at the discussion of the results. The pdf's of the prior and the posterior distributions for the calibration with six, four and five experimental data are respectively illustrated in Figures 5.5, 5.6 and 5.7.

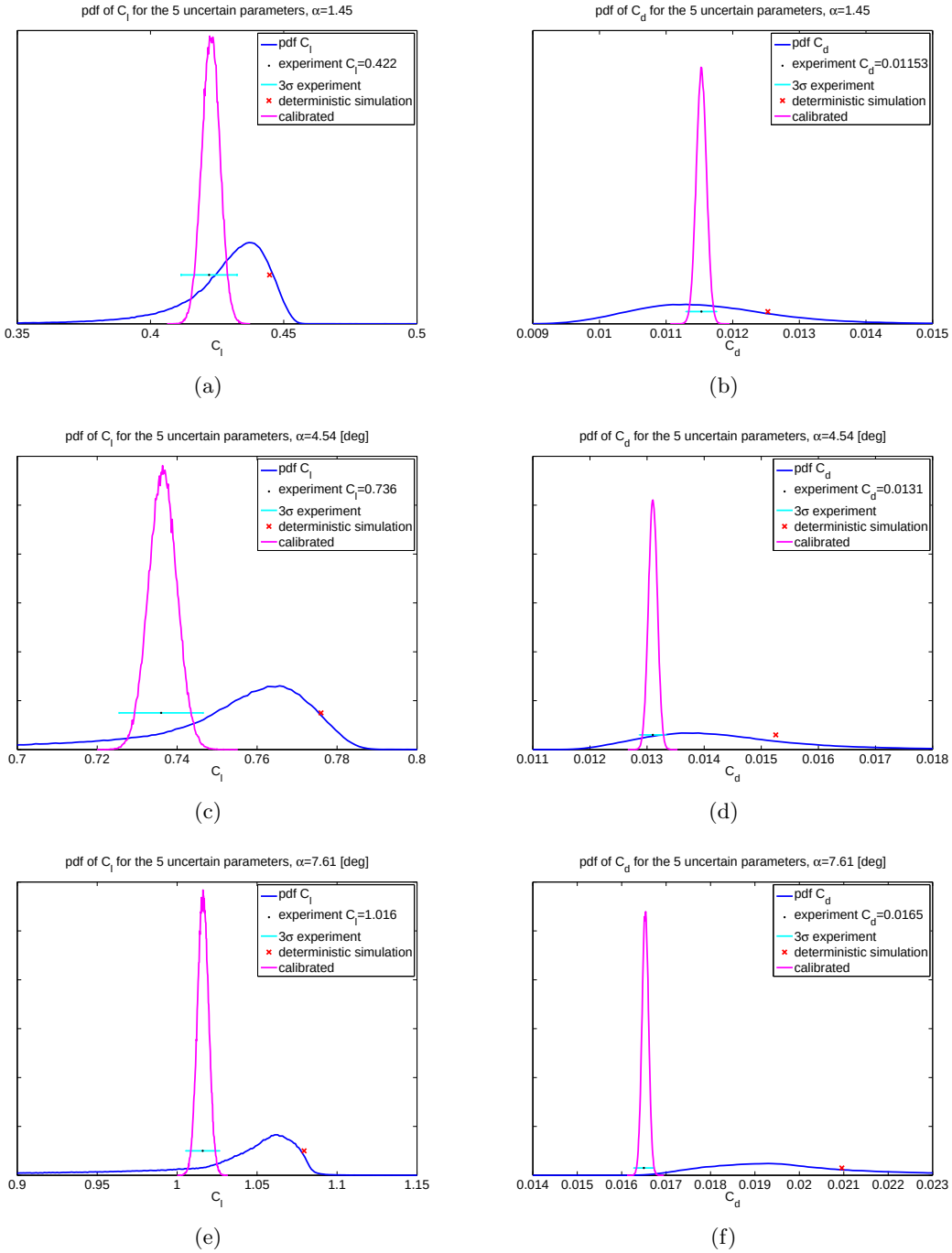

Figure 5.1: Posterior and prior pdf's of C_l and C_d at three different AoA.

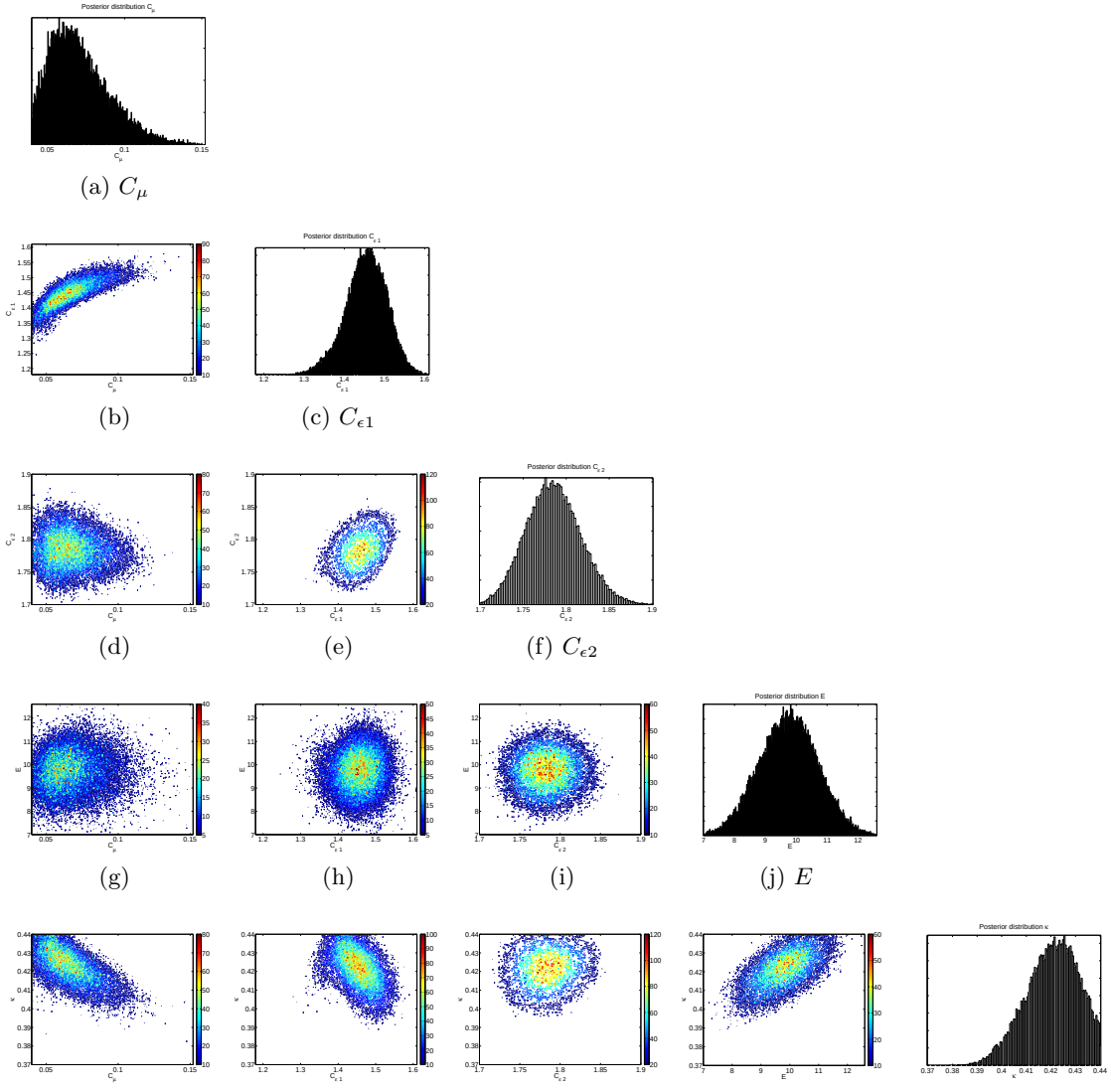

(a) C_μ (b) (c) $C_{\epsilon 1}$ (d) (e) (f) $C_{\epsilon 2}$ (g) (h) (i) (j) E (k) (l) (m) (n) (o) κ

Figure 5.2: Posterior distributions of the uncertain parameters and the 2-D marginal distributions are presented respectively at the diagonals and off-diagonals for $\alpha = 1.45°$.

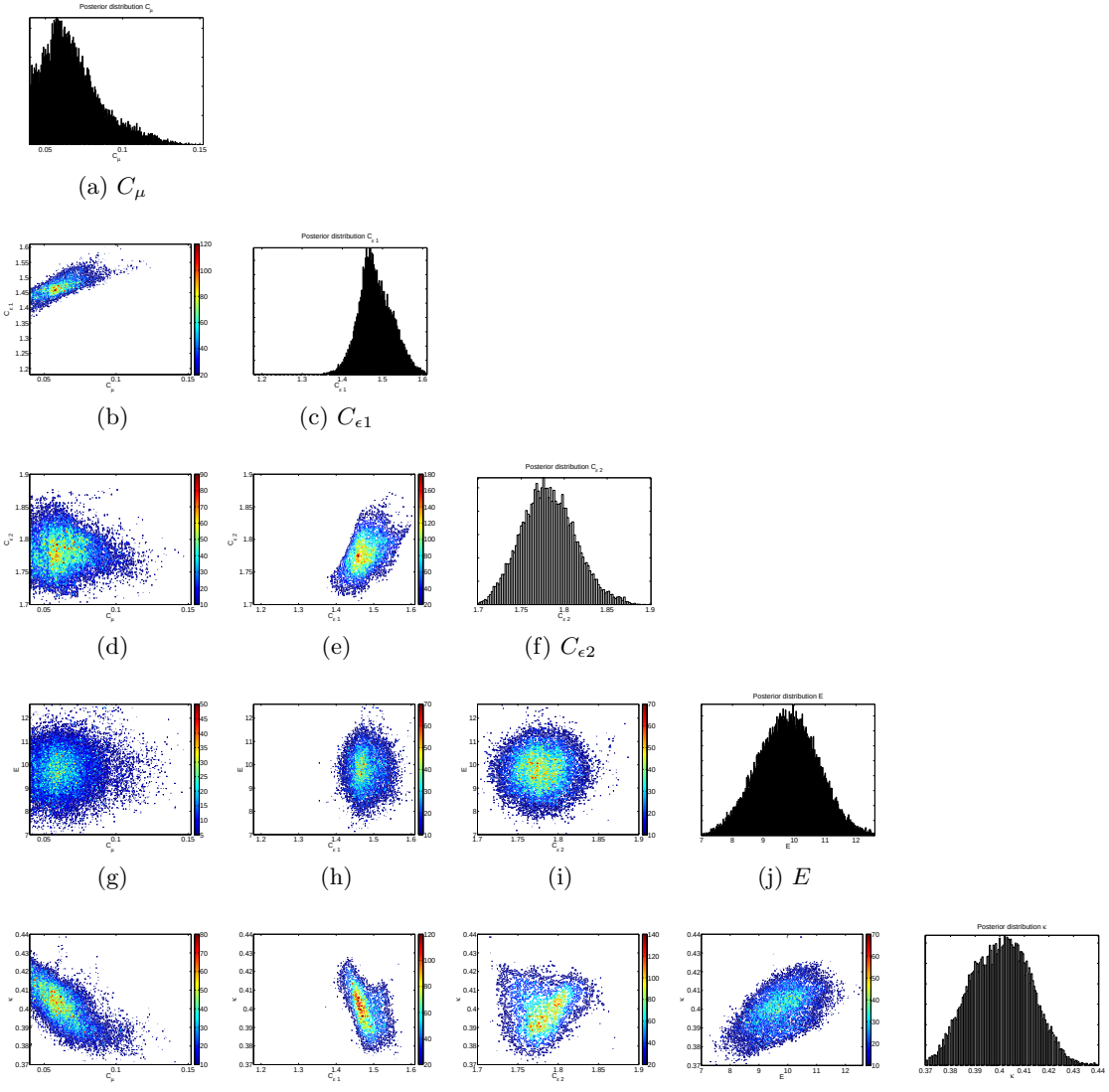

(a) C_μ (b) (c) $C_{\epsilon 1}$

(d) (e) (f) $C_{\epsilon 2}$

(g) (h) (i) (j) E

(k) (l) (m) (n) (o) κ

Figure 5.3: Posterior distributions of the uncertain parameters and the 2-D marginal distributions are presented respectively at the diagonals and off-diagonals for $\alpha = 4.54°$.

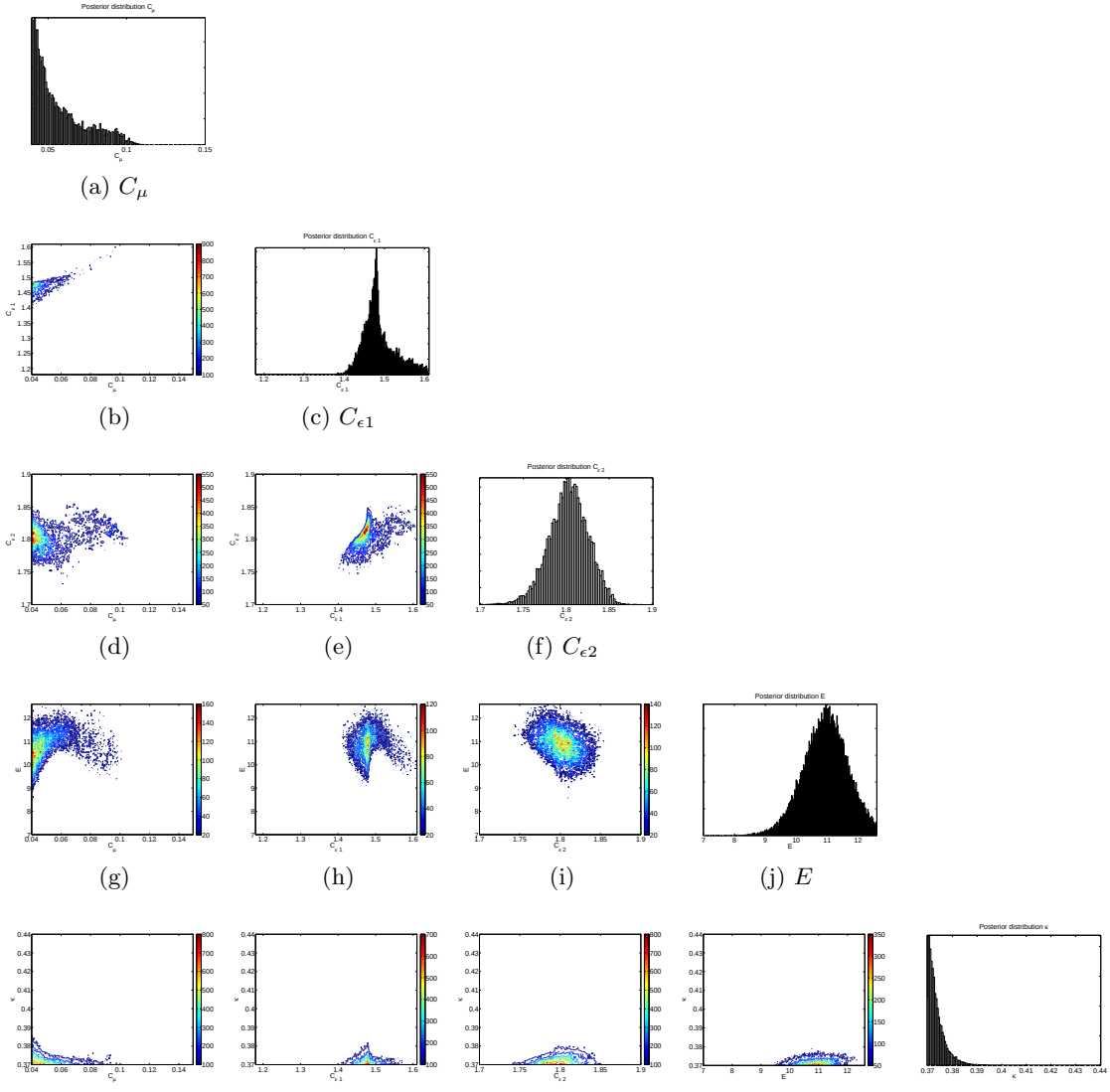

(a) C_μ (b) (c) $C_{\epsilon 1}$ (d) (e) (f) $C_{\epsilon 2}$ (g) (h) (i) (j) E (k) (l) (m) (n) (o) κ

Figure 5.4: Posterior distributions of the uncertain parameters and the 2-D marginal distributions are presented respectively at the diagonals and off-diagonals for $\alpha = 7.61°$.

The fit to the experimental data by the calibration with the six experimental data is not accurate. Only for the distributions at $\alpha = 4.54$ it is accurate. The main reason for the incapability of the model parameters to predict the experimental data at those AoA is the experimental data of C_d at $\alpha = 7.61°$. This experimental data lies just on the left tail of the prior distribution of the C_d. Therefore, the calibration is performed again but now by discarding the experimental data at $\alpha = 7.61°$ from the calibration process. Hence, the calibration is performed with four experimental data at the AoA 1.45° and 4.54°. The distributions at $\alpha = 7.61°$ are predicted with the calibrated parameters. The results of the calibration with four experimental data are accurate for AoA 1.45° and 4.54°. However, the predicted results of $\alpha = 7.61°$ are not accurate. As last the calibration is performed by only discarding the experimental data of C_d at $\alpha = 7.61°$ which proves that the main source of the error is this data. This data is the error in the sense that the $k-\epsilon$ model has difficulty with predicting this quantity. For the last performed calibration the posteriors of the force coefficients for the calibrated data are good. The predicted distribution of C_d at $\alpha = 7.61°$ is not accurate.

The posterior and 2-D marginal distributions of the uncertain parameters are presented in Figures 5.8, 5.9 and 5.10 respectively for the performed calibration with six, four and five experimental data. For the calibrations with six and five experimental data the parameters C_μ, $C_{\epsilon 1}$ and $C_{\epsilon 2}$ are well informed by the calibrations. The calibration with six experimental data yields peculiar distributions for κ and E. And κ and E are less informed by all the calibrations presented in this section.

Remarkably, the starting points for the calibration with the MCMC algorithm have influence, especially, on the posterior distributions of the model parameters. This is illustrated in Figure 5.11. Therefore, the calibrations with the six experimental data are carried out again with 25 different starting points to obtain the comprehensive posterior distribution of the model parameters. In this way obtained comprehensive posterior distributions of the force coefficients and the model parameters from the calibration with six experimental data are respectively illustrated in Figures 5.12 and 5.13. The posterior distributions of the model parameters illustrate that there are more distinct sets of parameters to calibrate the model to the experimental data. The posterior distributions of the force coefficients indicate that there are differences between the used set of parameters in predicting the force coefficients, however, these differences do not result in more accurate predictions of the experimental data.

The set of the model parameters that maximizes the $p(\mathbf{d}|\boldsymbol{\theta})$ for the combined calibrations are given in Table 5.2.

5.5 Simulations with the calibrated parameters

The calibrated uncertain parameters in the previous sections are used to simulate the turbulent flow over the airfoil DU96-W-180 for varying angles of attack. The results of the simulations with the calibrated parameters in Section 5.4 are compared with the experimental data, deterministic simulations, with each other and at three angles of attack with

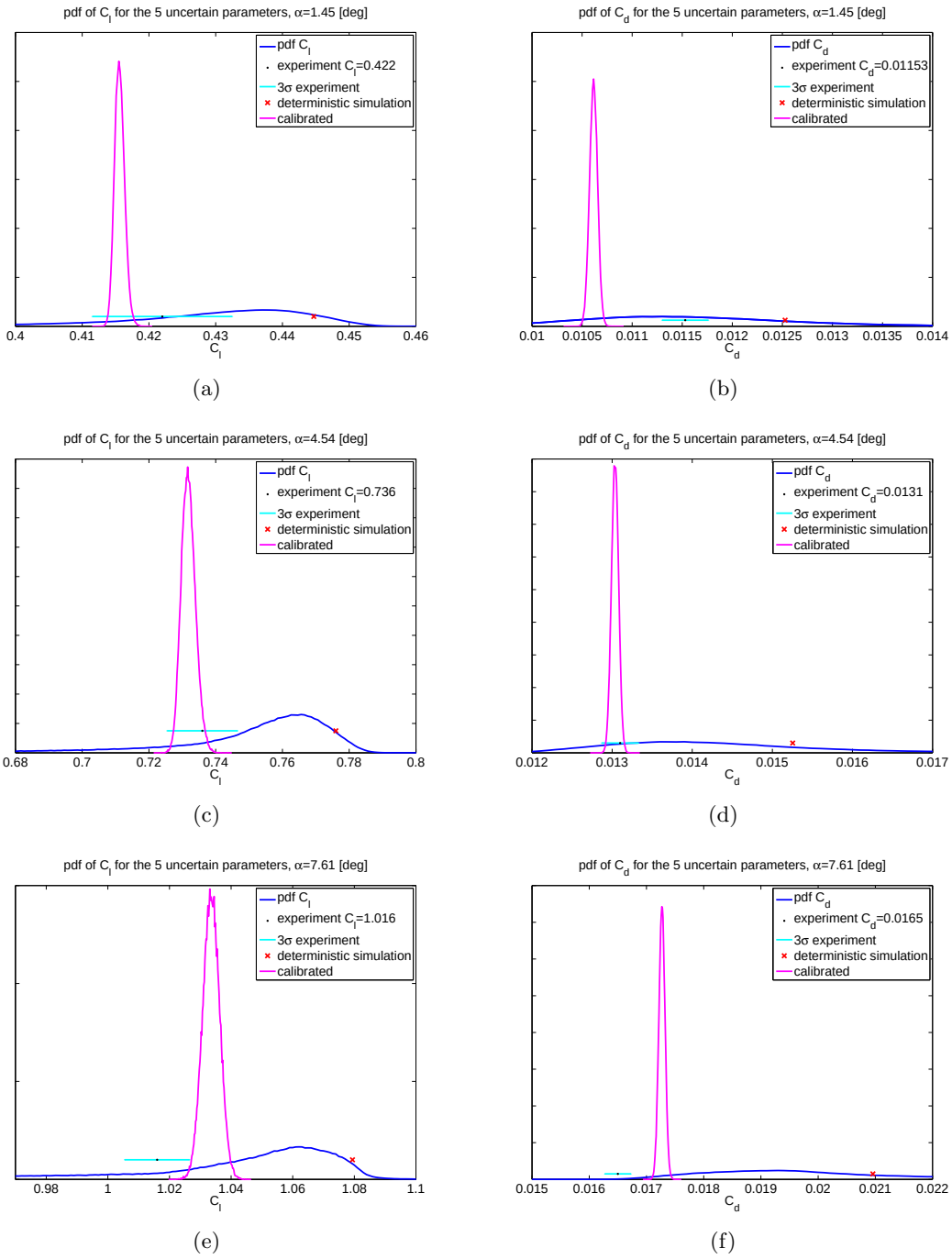

Figure 5.5: Posterior and prior pdf's of C_l and C_d of the calibration with six experimental data at $\alpha = 1.45°$, $\alpha = 4.54°$ and $\alpha = 7.61°$.

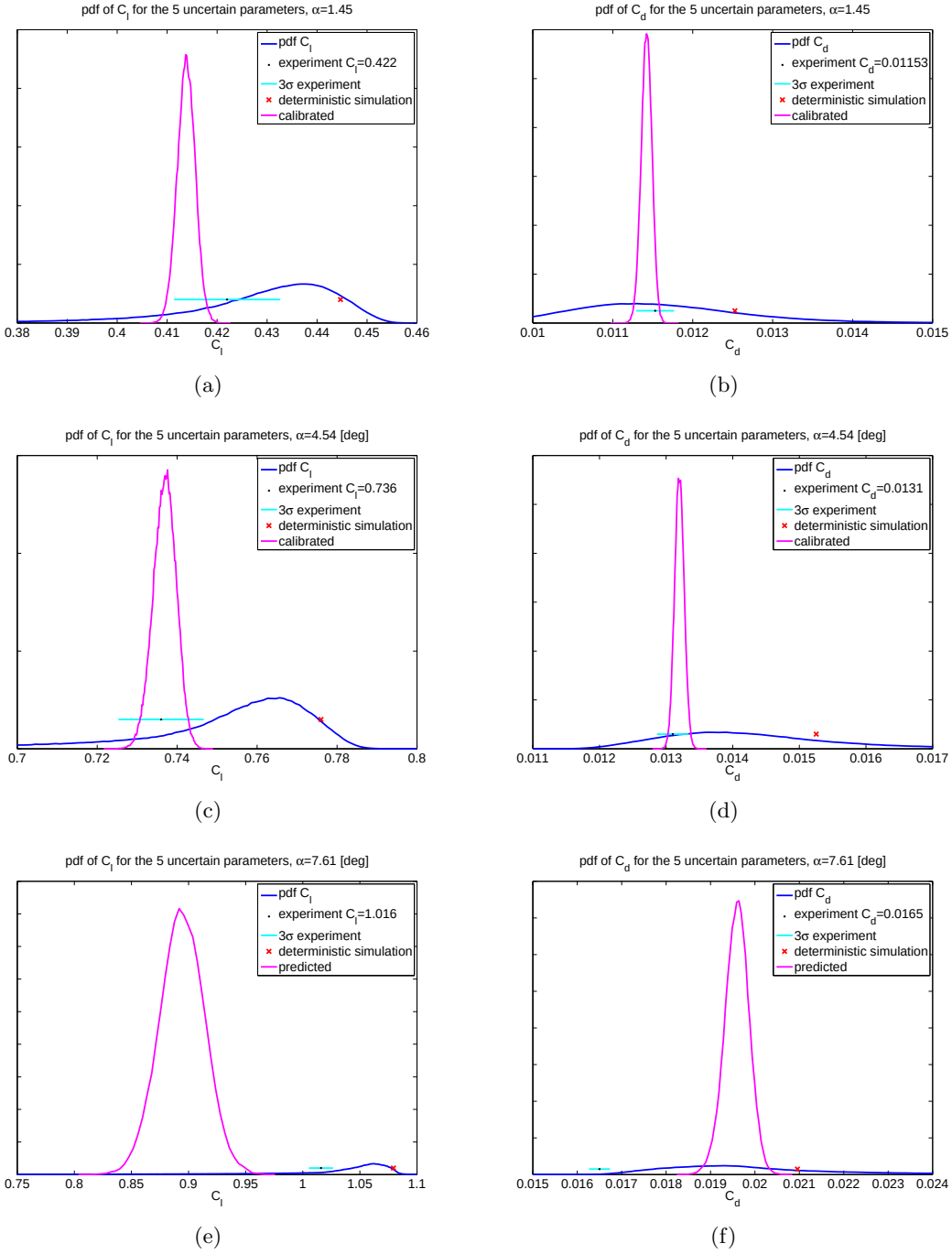

Figure 5.6: Posterior and prior pdf's of C_l and C_d of the calibration with four experimental data at $\alpha = 1.45°$ and $\alpha = 4.54°$. The posterior distributions at $\alpha = 7.61°$ are predicted with the calibrated parameters.

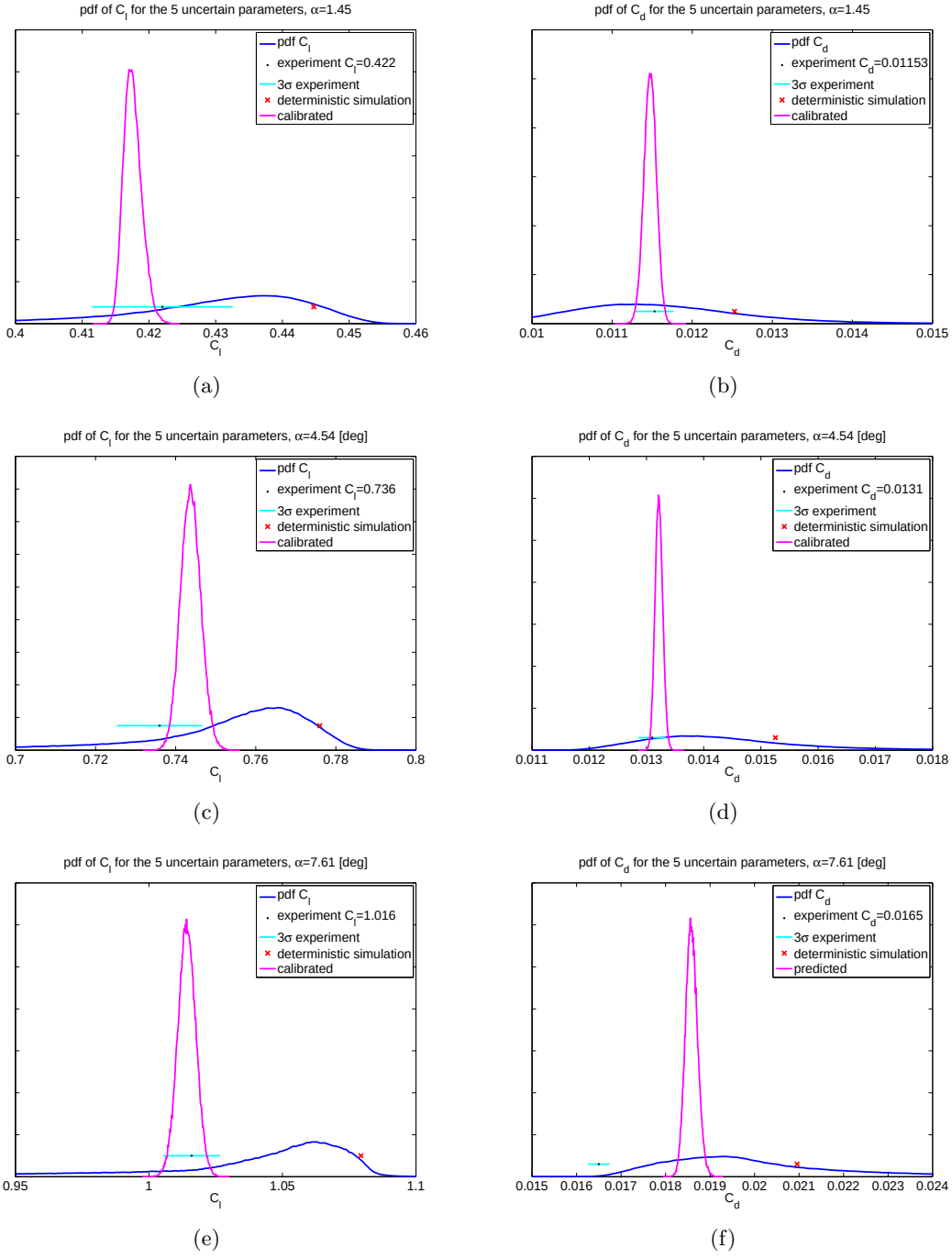

Figure 5.7: Posterior and prior pdf's of C_l and C_d of the calibration with five experimental data at $\alpha = 1.45°$, $\alpha = 4.54°$ and $\alpha = 7.61°$. The posterior distribution of C_d at $\alpha = 7.61°$ is predicted with the calibrated parameters, because it was not taken into account at the calibration.

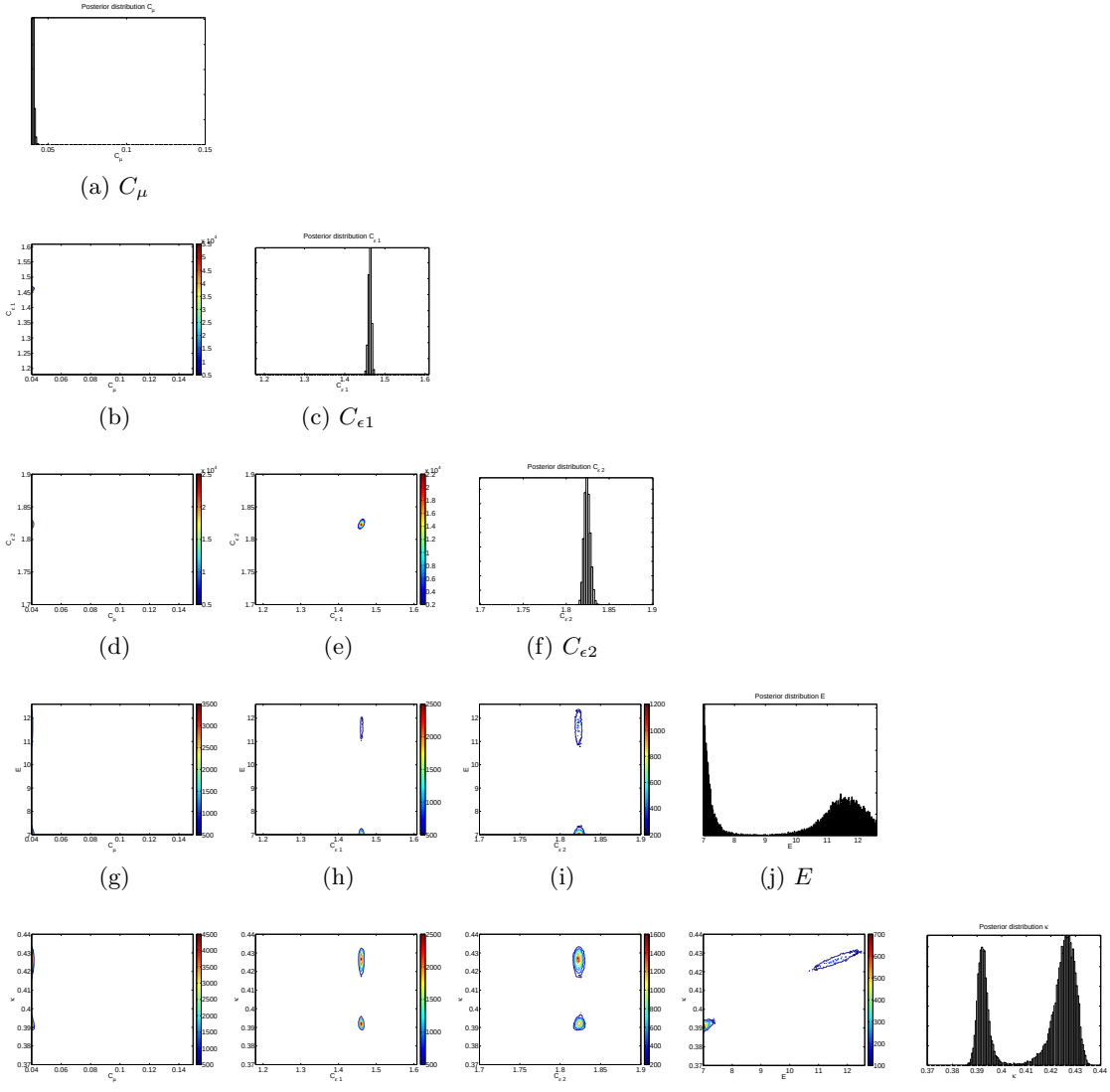

(a) C_μ (b) (c) $C_{\epsilon 1}$

(d) (e) (f) $C_{\epsilon 2}$

(g) (h) (i) (j) E

(k) (l) (m) (n) (o) κ

Figure 5.8: Posterior distributions of the uncertain parameters and the 2-D marginal distributions are presented respectively at the diagonals and off-diagonals, as a result of calibration with six experimental data.

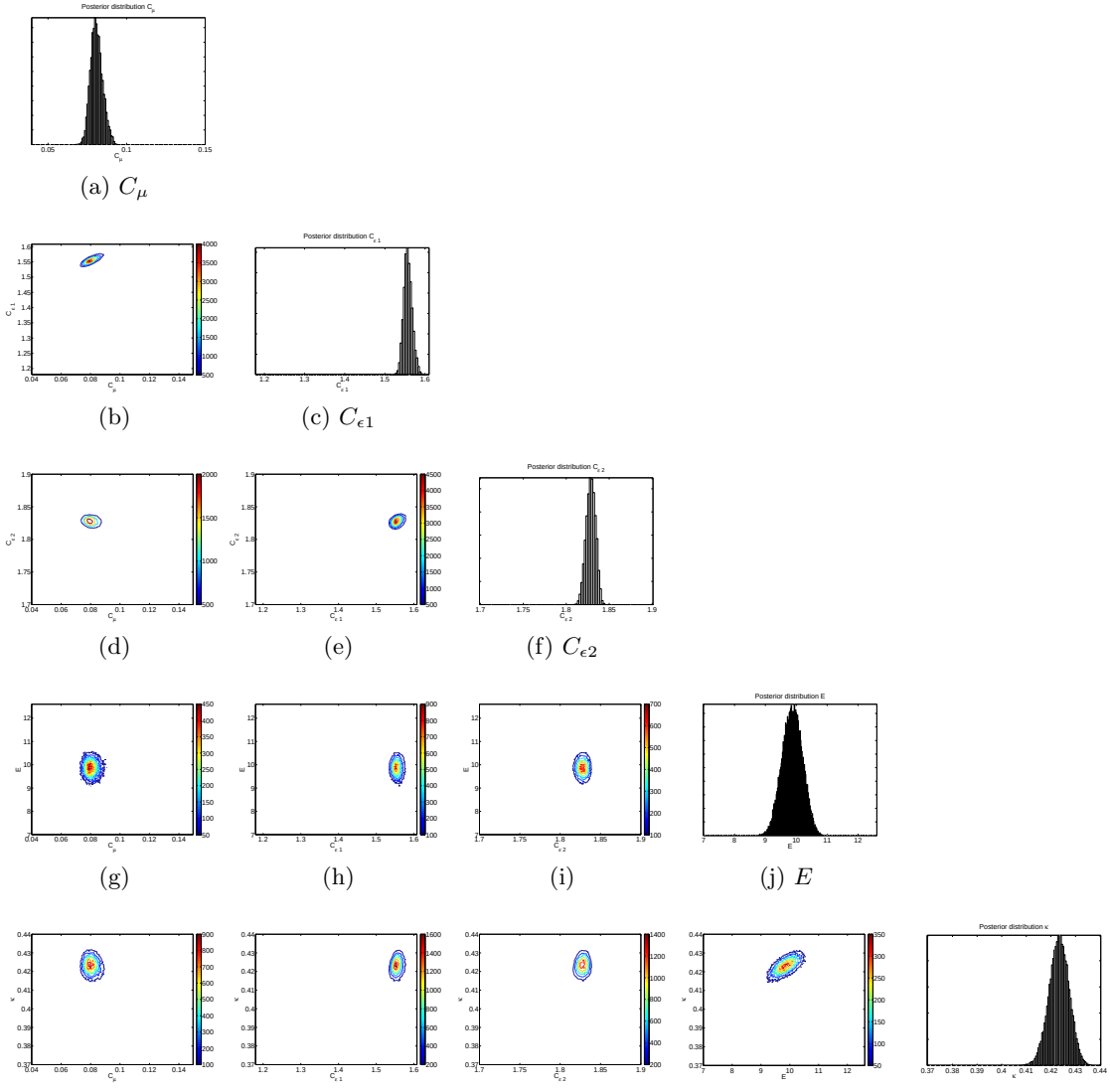

(a) C_μ (b) (c) $C_{\epsilon 1}$ (d) (e) (f) $C_{\epsilon 2}$ (g) (h) (i) (j) E (k) (l) (m) (n) (o) κ

Figure 5.9: Posterior distributions of the uncertain parameters and the 2-D marginal distributions are presented respectively at the diagonals and off-diagonals, as a result of calibration with four experimental data.

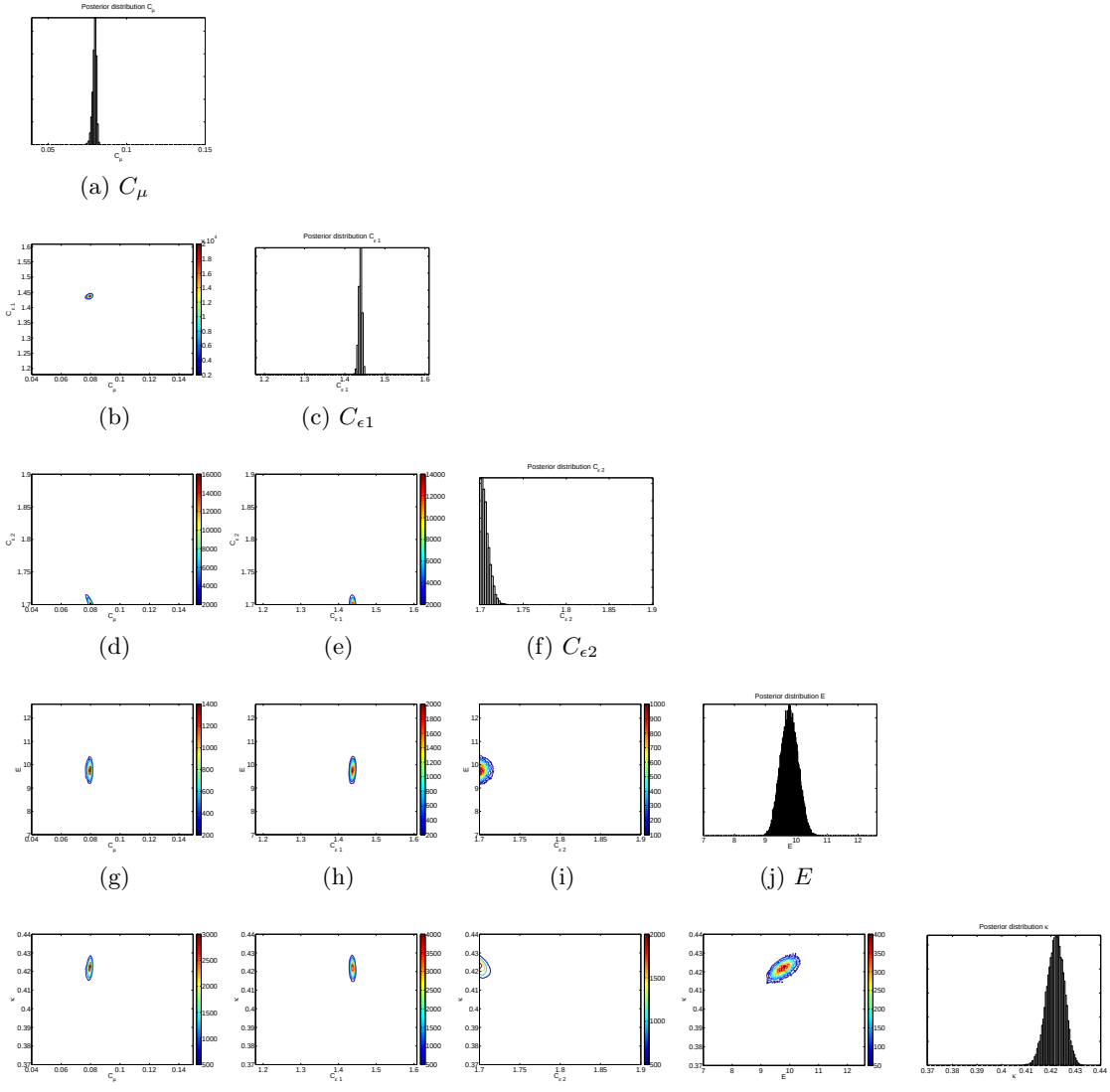

(a) C_μ (b) (c) $C_{\epsilon 1}$

(d) (e) (f) $C_{\epsilon 2}$

(g) (h) (i) (j) E

(k) (l) (m) (n) (o) κ

Figure 5.10: Posterior distributions of the uncertain parameters and the 2-D marginal distributions are presented respectively at the diagonals and off-diagonals, as a result of calibration with five experimental data.

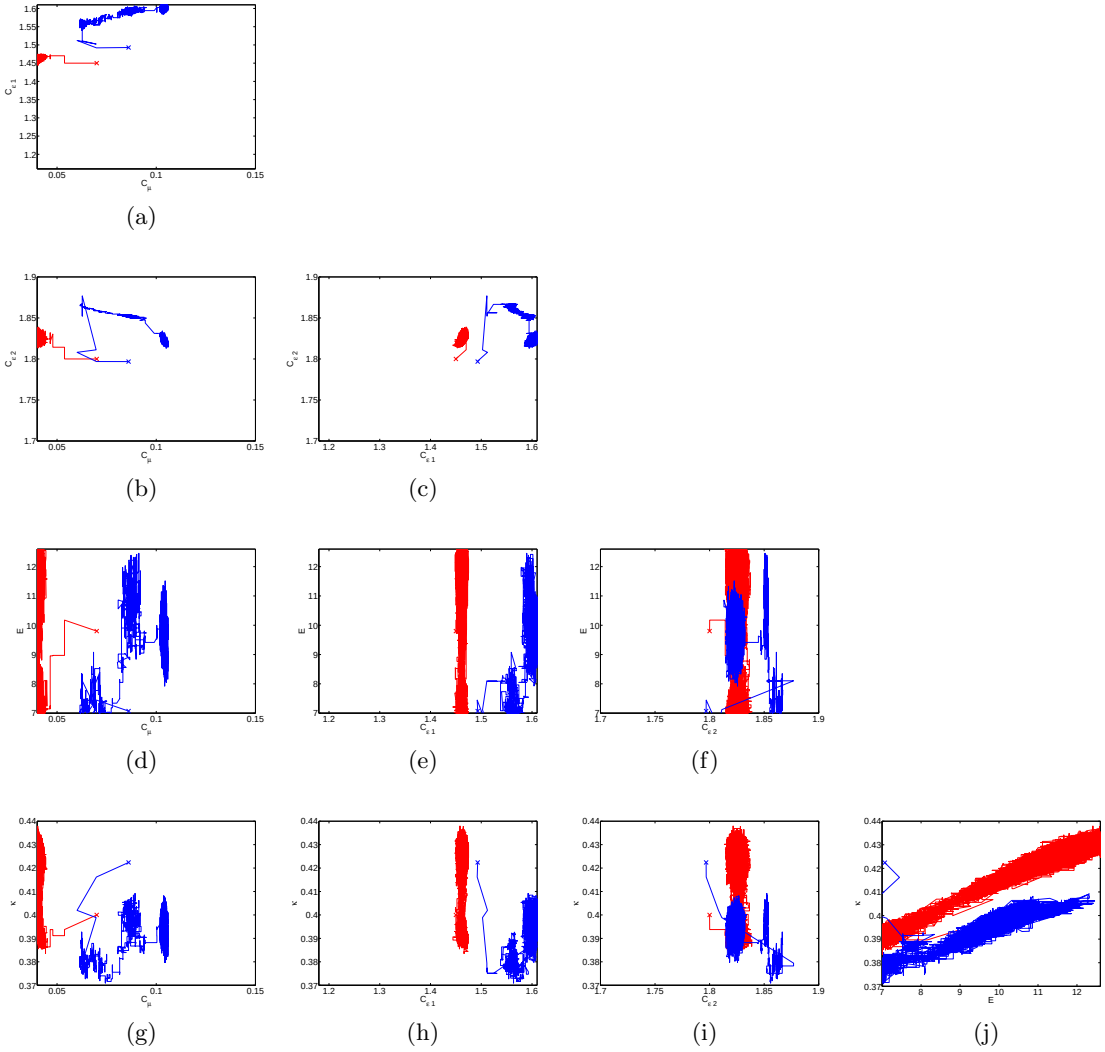

Figure 5.11: Depending on the first guess of the uncertain parameter the calibrated parameters can be different which is illustrated with two different starting points. Figure 5.8 is obtained with the start points of red color.

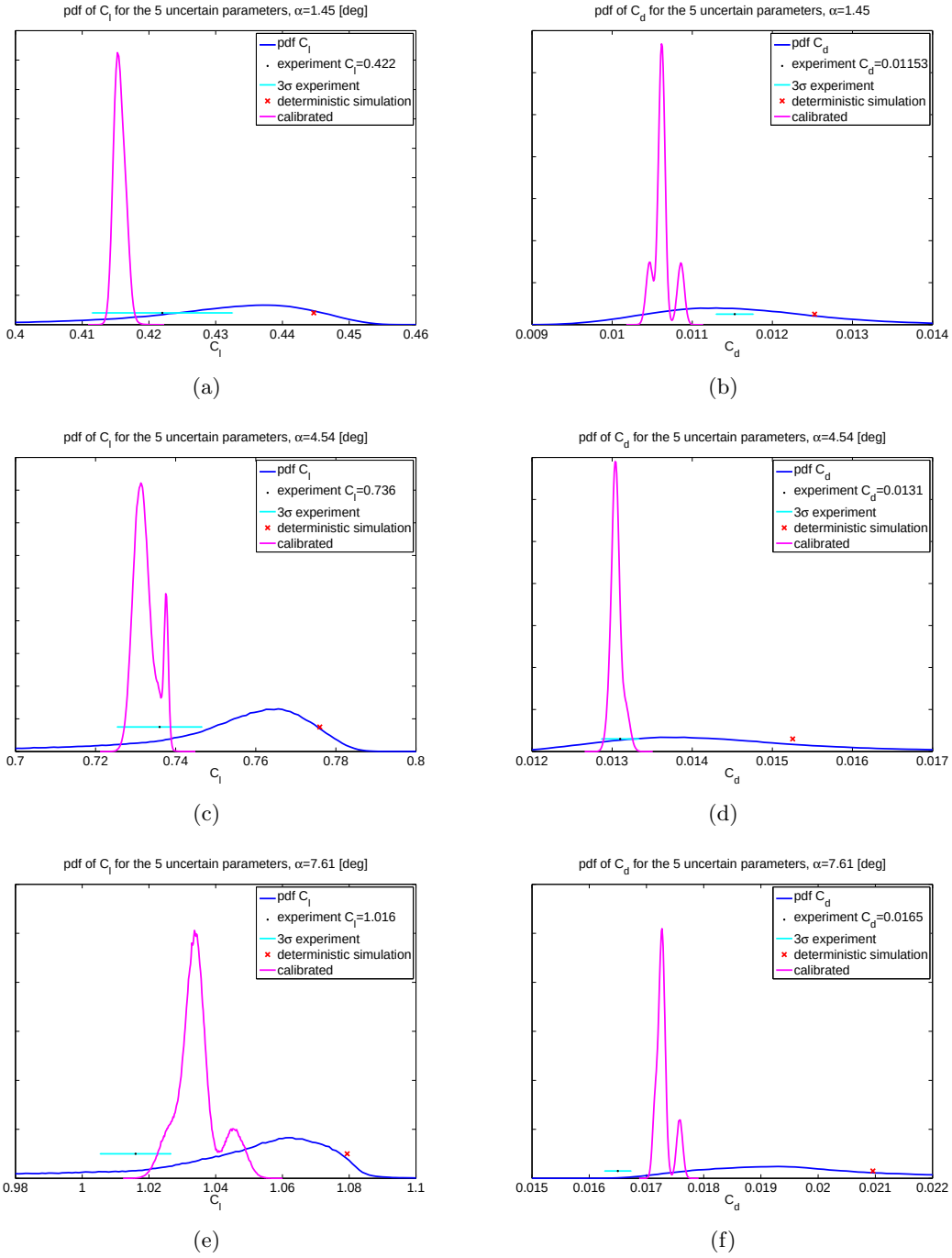

Figure 5.12: Posterior and prior pdf's of calibration with 25 different start points and with six experimental data at $\alpha = 1.45°$, $\alpha = 4.54°$ and $\alpha = 7.61°$.

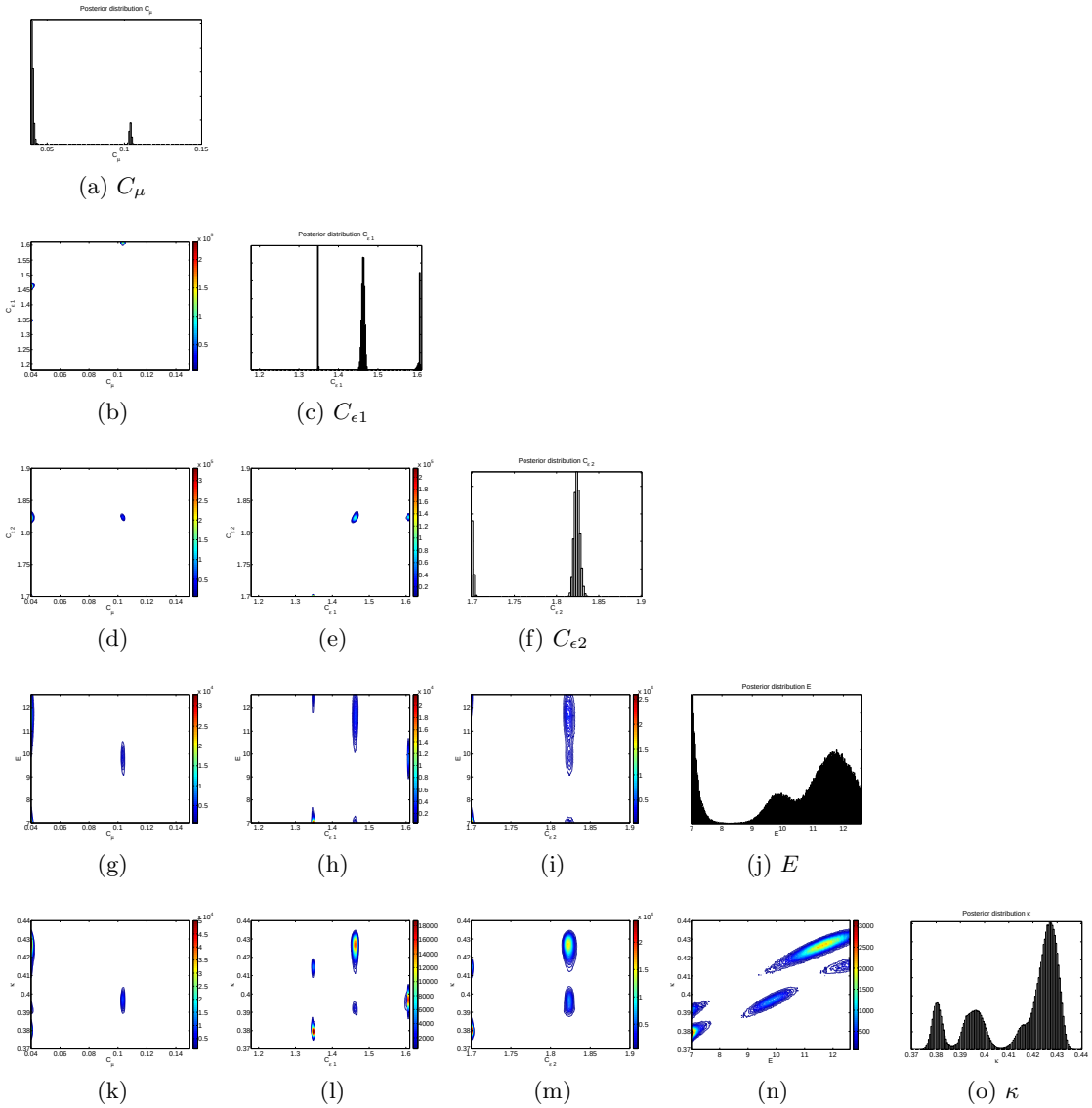

(a) C_μ (b) (c) $C_{\epsilon 1}$ (d) (e) (f) $C_{\epsilon 2}$ (g) (h) (i) (j) E (k) (l) (m) (n) (o) κ

Figure 5.13: Posterior distributions of the uncertain parameters and the 2-D marginal distributions are presented respectively at the diagonals and off-diagonals, as a result of calibration with six experimental data. 25 different start points are used to obtain these results.

	6 data	**4 data**	**5 data**
C_μ	0.103756725470	0.079599012885	0.080946311920
$C_{\epsilon 1}$	1.606746810726	1.554258910368	1.440408062517
$C_{\epsilon 2}$	1.825437489682	1.829759937789	1.700294406334
E	9.860082597488	9.892992729003	9.718884014073
κ	0.397352652958	0.424436897217	0.422958687887
C_l $\alpha = 1.45°$	0.415366404929	0.414243778403	0.416187919734
C_d $\alpha = 1.45°$	0.010865914980	0.011442509924	0.011494560596
C_l $\alpha = 4.54°$	0.732142549175	0.737075284310	0.742111666179
C_d $\alpha = 4.54°$	0.013165248206	0.013174244709	0.013171550904
C_l $\alpha = 7.61°$	1.026592646798	0.893664888587	1.015300258003
C_d $\alpha = 7.61°$	0.017150183340	0.019660632958	0.018499655145

Table 5.2: The set of calibrated model parameters that maximizes $p(\mathbf{d}|\boldsymbol{\theta})$ and the prediction of the force coefficients with the calibrated set at three different AoA. Note that respectively for *4 data* and *5 data* the experimental data of $\alpha = 7.61°$ and the experimental data C_d at $\alpha = 7.61°$ is not used in the calibration process, they are only predicted.

the surrogate models. These results of the numerical simulations and their discrepancy with respect to the experimental data are depicted in Figure 5.14 for the force coefficients. At large AoA the simulations with the calibrated parameters did not converge, so, their results are not given in the figure.

The discrepancy of the numerical simulations with the calibrated parameters in Section 5.3 with respect to the experimental data are illustrated in Figure 5.15.

The discussion of the results is presented in the following list respectively for C_l and C_d:

- C_l: Remarkably, the calibrations that are performed with two data for one α result in better simulations than the simulations for combined α. Especially the calibrated set at $\alpha = 1.45°$ is very good. Up to $\alpha = 5°$ the combined calibrations result also in good predictions of C_l.

  Note that there are large differences in the predictions of the surrogate models and the numerical simulations with the calibrated set for four, five and six data with a maximum of 8.9903 % at $\alpha = 7.61°$, see Table 5.3.

- C_d: The discrepancies of the simulations with respect to the experimental data have a similar oscillating curve with a different position on the ordinate. Which calibrated set of parameters is more accurate depends on the AoA because of the peculiar path of C_d for the calibrated range. However, the calibrations with four and five data give quite good results for α up to five degrees. The discrepancy of the surrogate models with the numerical simulations increases up to 6.25% for C_d.

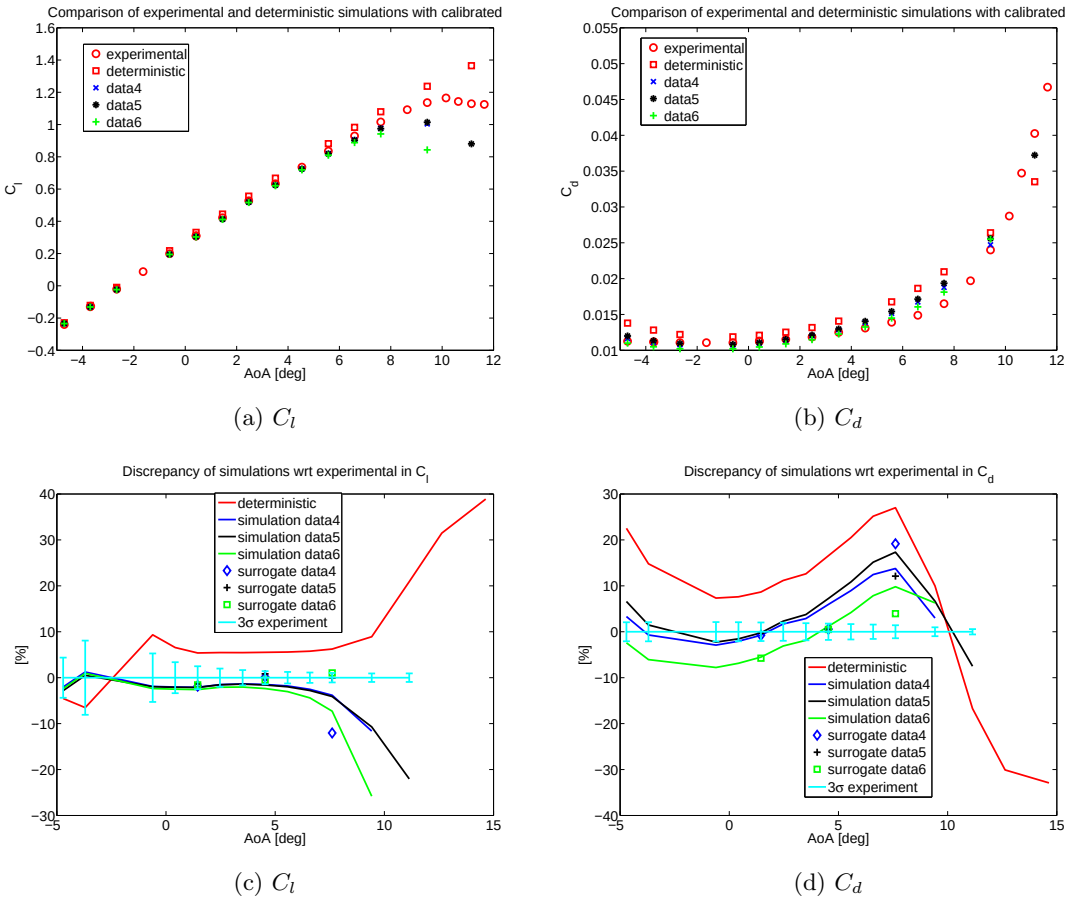

(a) C_l (b) C_d

(c) C_l (d) C_d

Figure 5.14: Numerical simulations with calibrated parameters are compared with the deterministic simulations and experimental data in (a) and (b). The difference of the simulations with the calibrated parameters and the surrogate model with respect to the experimental data [%] are illustrated in (c) and (d). The number behind the data refers to the amount of experimental data used to calibrate the model.

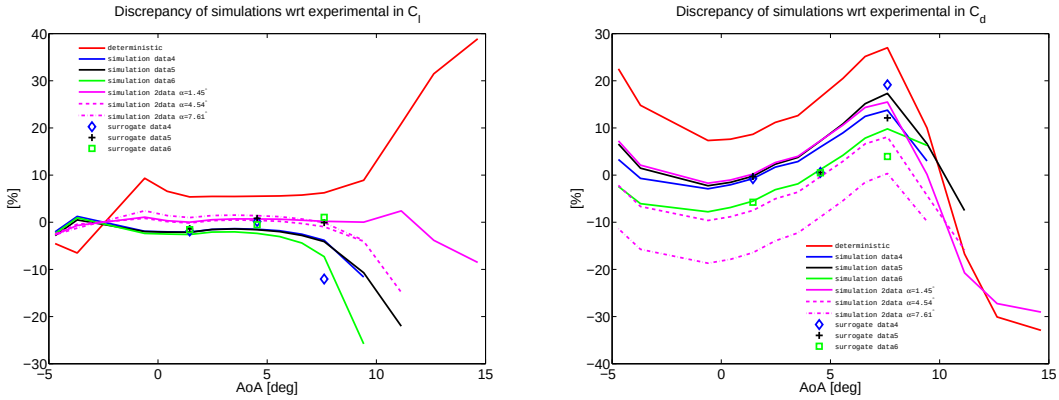

(a) C_l (b) C_d

Figure 5.15: The discrepancy with respect to the experimental data of all the numerical simulations that are performed with the calibrated set of parameters.

	$\alpha = 1.45°$	$\alpha = 4.54°$	$\alpha = 7.61°$
Data 6 C_l	1.0519	1.8835	8.9903
Data 6 C_d	-0.2567	-0.6741	-5.3406
Data 5 C_l	0.7730	2.4534	4.2004
Data 5 C_d	-0.0780	-6.2446	-4.4420
Data 4 C_l	0.2665	1.6506	-8.5418
Data 4 C_d	-0.0090	-5.0831	4.7292

Table 5.3: The discrepancy of the surrogate model in [%] with respect to the calibrated simulations.

Chapter 6

Conclusions & Recommendations

In this final chapter of the thesis the conclusions and recommendations are stated. Before that the main objectives of the thesis are summarized:

- Quantify the uncertainty in the model parameters of the $k-\epsilon$ model.
- Propagate the uncertainty in the parameters through the $k-\epsilon$ model to investigate the effect of them on the force coefficients C_l and C_d.
- To improve the prediction capability of the $k-\epsilon$ model perform calibration with the Bayesian inference method.

6.1 Conclusions

To quantify the uncertainty in the model parameters a literature research is performed. By using simplified relations, experimental data and expert opinions the distributions of the uncertain parameters are determined. However, the determined distributions are not unique. Moreover, using different relations to define the distributions in the used methodology leads to convergence problems. Therefore, defining the distributions became an iterative procedure.

From the UQ analysis with separately propagated parameters (1-D) appeared that for the lift coefficient C_l the most influential uncertain parameter is C_μ with coefficient of variation (CV) of 1.096 % and for the drag coefficient C_d it is $C_{\epsilon 1}$ with CV of 6.674 %. The discretization error is 8.3 % and 1.74 % of the range of C_μ C_l and $C_{\epsilon 1}$ C_d. Hence, the discretization error can be considered as small compared to the uncertainty in the model parameters.

From the results of 1-D UQ analysis the most influential five parameters on the force coefficients are determined. These are C_μ, $C_{\epsilon 1}$, $C_{\epsilon 2}$, κ and E. Subsequently the probability density functions (pdf) of the force coefficients are determined with the simultaneously propagated uncertainty for those five parameters for three different angles of attack $\alpha = 1.45°$, $\alpha = 4.54°$ and $\alpha = 7.61°$. The range of the experimental data and the force coefficients is finite. For $\alpha = 1.45°$ the discretization error is 11.8 % and 10.7 % respectively of the standard deviations of C_l and C_d. Which illustrates the importance of the uncertainty quantification. Furthermore, the CV of the force coefficients increase for increasing α. Respectively for $\alpha = 1.45°$ and $\alpha = 7.61°$ the CV of C_l is 4.804 and 9.99 % and the CV of C_d is 9.306 and 12.95 %.

Subsequently, the five most influential parameters are calibrated by using surrogate models of the standard $k - \epsilon$ model.

The parameters are readily calibrated to the experimental data at one α.

The calibrations by combining experimental data at the three α of 1.45°, 4.54° and 7.61° did not result in accurate fits to the experimental data. Main reason therefore is the model inadequacy to predict the drag coefficient accurately at high α. When the experimental data at $\alpha = 7.61°$ is discarded from the calibration, thus the process is carried out with data at α is 1.45° and 4.54°, the predictions of the force coefficients become more accurate up to $\alpha = 5°$. Neglecting only the C_d at $\alpha = 7.61°$ results in similar accuracy with respect to neglecting the complete data at $\alpha = 7.61°$ up to $\alpha = 5°$.

Discrepancy is observed between the surrogate models and the numerical simulations, especially, at α is 4.54° and 7.61°. Which definitely deteriorates the calibration process. The absolute maximum discrepancy is 8.9903 % for C_l at $\alpha = 7.61°$ and 6.2446 % for C_d at α 4.54°.

6.2 Recommendations

- To overcome the time consuming iterative process of defining the distributions, due to convergence problems, one can be freer in defining the distributions. Still, the basis of this analysis should be the analytic relations, nevertheless, it is not unacceptable if the defined distributions do not meet those relations. After all, the $k - \epsilon$ model is an invention with calibrated constants to predict turbulent flows, which is a very difficult subject.

- Although it is not tested fixing the difference between $C_\epsilon 2$ and $C_{\epsilon 1}$ may decrease the convergence problems.

- To improve the accuracy of the surrogate models the order of the polynomials should be increased, which is especially necessary for high α. If the required high amount of simulations exceeds the computational resources the number of uncertain parameters can be decreased further.

- To take into account the model inadequacy of the $k - \epsilon$ model a term could be introduced in the statistical model used to calibrate the model.

- More data can be used in the calibration process like the pressure or skin friction along the airfoil to take into account the local effects along the airfoil.
- Because the $k - \epsilon$ model needs a wall function to simulate a wall bounded flow it has more variables than only the $k - \epsilon$ equations. This inserts more uncertainties in the problem and makes the UQ more complex. Like the y^+ value of the first cell, which is different for every generated mesh and the solution is dependent on that value. The applied procedure in this thesis can be performed for a model which do not need wall functions like the SST $k - \omega$ model. Then, only the real model parameters have to be calibrated.

References

Anderson, J. D. (1995). *Computational fluid dynamics.* McGraw-Hill, Inc.

Babuska, I., Nobile, F., & Tempone, R. (2007). A stochastic collocation method for elliptic partial differential equations with random input data. *SIAM Journal of Numerical Analysis*, *45/3*, 1005-1034.

Bradshwa, P., Cebeci, T., & Whitelaw, J. H. (1981). *Engineering calculation methods for turbulent flow.* Academic Press.

Chen, C.-J., & Jaw, S.-Y. (1998). *Fundamentals of turbulence modelling.* Taylor & Francis.

Cheung, S. H., Oliver, T. A., Prudencio, E. E., Prudhomme, S., & Moser, R. D. (2011). Bayesian uncertainty analysis with applications to turbulence modeling. *Reliability Engineering and System Safety*, *96*, 1137-1149.

Comte-Bellot, G., & Corrsin, S. (1966). The use of a contraction to improve the isotropy of grid-generated turbulence. *Journal of Fluid Mechanics*, *25*, 657-682.

Davidson, P. A. (2004). *turbulence, an introduction for scientist and engineers.* Oxford University Press.

Durbin, P. A., & Pettersson Reif, B. A. (2011). *Statistical theory and modeling for turbulent flows* (2nd ed.). John Wiley and Sons, Ltd.

Eckhardt, B. (2009). Turbulence transition in pipe flow: 125th anniversary of the publication of reynolds' paper. *Philosophical Transactions Of The Royal Society*, *367*, 449-455.

Fluent. (n.d.). ANSYS. Available from http://www.ansys.com/

Gatski, T. M., Hussaini, M. Y., & Lumley, J. L. (1996). *Simulation and modeling of turbulent flows.* Oxford University Press.

Ghanem, R., & Spanos, P. (1991). *Stochastic finete elements: A spectral approach.* Springer Verlag.

Hanjalic, K. (2004).
In *Introduction to turbulence modeling.* von Karman Institute for Fluid Dynamics.

Harlow, F. H., & Nakayama, P. (1968). *Transport of turbulence energy decay rates* (Tech. Rep.). Los Alamos Scientific Laboratory of the University of California. (LA-3854)

Kennedy, M. C., & O'Hagan, A. (2001). Bayesian calibration of computer models. *SIAM Journal of Numerical Analysis*, *63*, 425-464.

Kim, J., Moin, P., & Moser, R. (1987). Turbulence statistics in fully developed channel flow at low reynolds number. *Journal of Fluid Mechanics*, *177*, 133-166.

Launder, B. E. (1972). *Lectures in mathematical models of turbulence.* Academic Press.

Launder, B. E., Morse, A., Rodi, W., & Spalding, D. B. (1972). *Prediction of free shear flows, a comparison of the performance of six turbulence models* (SP No. 311). N.A.S.A.

Launder, B. E., & Spalding, D. B. (1974). The numerical computation of turbulent flows. *Computer Methods in Applied Mechanics and Engineering*, *3*, 269-289.

Loeven, A., Witteveen, J., & Bijl, H. (2006). Efficient uncertainty quantification using a two-step approach with chaos collocation. In *Eccomas cfd.* European Conference on Computational Fluid Dynamics.

Loeven, G. J. A. (2010). *Efficient uncertainty quantification in computational fluid dynamics.* Unpublished doctoral dissertation, Delft University of Technology.

Loeven, G. J. A., & Bijl, H. (2008). Airfoil analysis with uncertain geometry using the

probabilistic collocation method. In *49th aiaa structures, structural dynamics, and materials conference.* American Institute of Aeronautics and Astronautics (AIAA).

Loeven, G. J. A., Witteveen, J. A. S., & Bijl, H. (2007, January). Probabilistic collocation: An efficient non-intrusive approach for arbitrarily distributed parametric uncertainties. In *45th aiaa aerospace sciences meeting and exhibit.* Reno Nevada, United States: AIAA.

Lophaven, S. N., Nielsen, H. B., & Sondergaard, J. (2002, August). *Dace, a matlab kringing toolbox* (2.0). Technical University of Denmark. (Informatics and Mathematical Modelling)

Metropolis, N., Rosenbluth, A. W., Rosenbluth, M. N., Teller, A. H., & Teller, E. (1953). Equations of state calculations by fast computing machines. *Journal of Chemical Physics*, *21*, 1087-1092.

Metropolis, S., & Ulam, S. (1949). The monte carlo method. *Journal of the American Statistical Association*, *44*, 335-341.

Mohamed, M. S., & LaRue, J. C. (1990). The decay power law in grid-generated turbulence. *Fluid Mechanics, volume 219.*.

Montgomery, D. C., & Runger, G. C. (1994). *Applied statistics and probability for engineers.* John Wiley & Sons.

OpenFOAM Team the. (n.d.). The OpenFOAM Foundation. Available from http://www.openfoam.org/ (1.6)

OpenFOAM Team the. (2011). User guide (2.1.0 ed.) [Computer software manual]. Available from http://www.openfoam.org/docs/

Osborne, R. (1883a). An experimental investigation of the circumstances which determine whether the motion of water shall be direct or sinuous, and the law of resistance in parallel channels. *Proceedings of the Royal Society*, *35*, 84-99.

Osborne, R. (1883b). An experimental investigation of the circumstances which determine whether the motion of water shall be direct or sinuous, and the law of resistance in parallel channels. *Philosophical Transactions of the Royal Society*, *174*, 935-982.

Osterlund, J. M., Johansson, A. V., Nagib, H. M., & Hites, M. H. (2000). A note on the overlap region in turbulent boundary layers. *Physics of Fluids 13, 229-238*. (12, 1)

Patankar, S. V., & Spalding, D. B. (1972). A calculation procedure for heat, mass and momentum transfer in three-dimensional parabolic flows. *Int. J. Heat Mass Transfer*, *15*, 1787-1806.

Platteeuw, P. D. A. (2008). *Application of the probabilistic collocation method to uncertainty in turbulence models.* Unpublished master's thesis, Delft University of Technology.

Pope, S. B. (1998). *Turbulent flows.* Cambridge University Press.

Salim, M. S., & Cheah, S. C. (2009). Wall yplus strategy for dealing with wall-bounded turbulent flows. *Proceedings of the International MultiConference of Engineers and Computer Scientist 2009 Vol 2*.

Tatang, M. A., Pan, W., Pring, R. G., & McRae, G. J. (1997). An efficient method for parametric uncertainty analysis of numerical geophysical models. *Journal of Geophysical Research*, *102*, 21925-21932.

Timmer, W. A., & Rooij, R. P. J. O. M. van. (2003). Summary of the delft university turbine dedicated airfoils. *ASME Journal of Solar Energy Engineering*, *125*.

Townsend, A. A. (2003). *The structure of turbulent shear flow.* Cambridge University Press.

Walsh, B. (2004, April). *Markov chain monte carlo and gibbs sampling* (Lecture Notes for EEB). Massachusetts Institute of Technology.

Wikle, C. K., & Berliner, L. M. (2006). A bayesian tutorial for data assimilation. *Physica D*.

Wilcox, D. C. (1994). *Turbulence modeling for cfd*. DCW Industries.

Witteveen, J. A. S. (2009). *Efficient and robust uncertainty quantification for computational fluid dynamics and fluid-structure interaction*. Unpublished doctoral dissertation, Delft University of Technology.